CORROSION BEHAVIOR OF MICROARC OXIDATION AND POLYCAPROLACTONE COATINGS APPLIED TO AZ31 MAGNESIUM ALLOY EVALUATED IN SIMULATED BODY FLUID AND BALANCED SALT SOLUTION

By

Benjamin M. Wilke

RECOMMENDED:

Dr. Cheng-fu Chen
Advisory Committee Member

Dr. Junqing Zhang
Advisory Committee Member

Dr. Rorik Peterson
Advisory Committee Member

Dr. Lei Zhang
Advisory Committee Chair

Dr. Rorik Peterson
Chair, Department of Mechanical Engineering

APPROVED:

Dr. Douglas Goering
Dean, College of Engineering and Mines

Dr. John Eichelberger
Dean of the Graduate School

17 July 2015
Date

CORROSION BEHAVIOR OF MICROARC OXIDATION AND POLYCAPROLACTONE COATINGS APPLIED TO AZ31 MAGNESIUM ALLOY EVALUATED IN SIMULATED BODY FLUID AND BALANCED SALT SOLUTION

A

THESIS

Presented to the Faculty

of the University of Alaska Fairbanks

in Partial Fulfillment of the Requirements

for the Degree of

MASTER OF SCIENCE

By

Benjamin M. Wilke, B.S.

Fairbanks, Alaska

August 2015

Abstract

Recent research in orthopedic implant materials has focused on the use of magnesium alloys as a base material due to its mechanical properties similar to that of human bone. Rapid corrosion of magnesium materials in aqueous environments poses a significant hurdle to their application as a biomedical implant. A variety of coatings have been shown to improve the corrosion resistance of magnesium based materials in simulated body fluid environments including microarc oxidation and polymer coatings. However, formulation and corrosion rates vary significantly between solution types. Furthermore, in vivo results have shown that many common in vitro solutions over estimate corrosion rates. In addition to variations between solutions needing to be resolved, there has been little work performed to characterize large sample corrosion under stress. This is an essential step in evaluating concept performance at a macro scale, for application as a human implant.

The experiments performed and presented in this thesis primarily involve the comparison of conventional simulated body fluid (c-SBF) and Earle's balanced salt solution (EBSS). Samples evaluated in these environments are microarc oxidation (MAO) coated AZ31 magnesium alloy and polycaprolactone dip-coated AZ31. MAO coated samples were created for a range of process settings to observe the effect of processing on corrosion performance. A dependence of MAO coating thickness on process voltage was found which augmented the initial corrosion resistance values observed via electrochemical testing. Both MAO and PCL coatings were found to improve the corrosion resistance of the samples as compared to uncoated AZ31. It was found that all variations (MAO, PCL, and uncoated) showed a reduced corrosion rate in EBSS as compared to c-SBF. This corrosion reduction was apparent through potentiodynamic scanning, electrochemical impedance spectroscopy, and visual inspection. Preliminary mechanical corrosion results, in the form of constant extension testing, showed no dependence of corrosion on stress level. Future work may be aimed towards expanding modes of mechanical testing and further refining simulated body fluids to fit with in vivo test results.

Table of Contents

List of Figures

Page

List of Tables

Page

List of Equations

Definitions

Anodic Region: The oxidation reaction for a material occurs resulting in corrosion of the sample. A large spike in current density in this region often coincides with the pitting potential E_{pit}, for local corrosion.

Bode Plot: Plots output from EIS consisting of impedance magnitude vs. frequency and phase angle vs. frequency.

Cathodic Region: Relating to the reduction reaction occurring for the system, production of hydrogen from magnesium corrosion in aqueous environments occurs due to the cathodic reaction taking place.

Conversion Coating: Coating created through a reaction between base material and environment (ex. passivation, chemical bath, anodization).

Deposition Coating: Coating through addition of material to a base substrate (ex. electrodeposition, spin/spray coat, or spin coating).

E_{corr}: Corrosion potential, also known as Open Circuit Potential (OCP), this is the potential between the working electrode (sample) and reference electrode (e.g. Saturated Calomel Electrode) with no load applied. At the OCP, the rates of the anodic and cathodic reactions in the system are balanced. This value typically shifts more positively when passivation occurs on the sample surface and negative when corrosion occurs.

I_{corr}: Corrosion current density is the measure of current density at the location of the open circuit potential. Corrosion current, I_{corr}, can be extrapolated via the Tafel method and can be used with Faraday's law to estimate corrosion rate.

In-Vitro: Referring to tests carried out in a simulated body environment (ex. Benchtop equipment, simulated body fluid)

In-Vivo: Referring to testing inside the body (ex. Animal studies, actual implantation)

MAO: Microarc oxidation also known as plasma electrolytic oxidation (PEO). Oxidation coating produced at high voltages resulting in well adhered, ceramic-like coating.

PCL: Polycaprolactone, polymer developed for drug delivery and biodegradable suture applications.

Acknowledgments

I would like to thank my graduate committee of Dr. Lei Zhang, Dr. Cheng-Fu Chen, Dr. Junqing Zhang, and Dr. Rorik Peterson for their guidance and review of my thesis research. In addition, I would like to express my gratitude to the Mechanical Engineering department for providing teaching assistantship in support of my studies at the University of Alaska. Research was also supported by Professor Chengyun Ning and Weiping Li at South China University of Technology through supplying MAO test samples. Thanks to Joe Michalski in the CEM machine shop and Ken Severin in the UAF Advanced Instrumentation Lab for equipment training and support.

Chapter 1: Introduction and Literature Review

1.1 Magnesium as a Biomedical Implant

Materials currently considered for use in orthopedic repair of bone damage may include metallic alloys, ceramics, and polymers [1]. Within these major classifications of materials exists a smaller population of options which have acceptable biocompatibility, corrosion resistance, and strength properties. Recent research in metallic biomaterials is focused on improving the properties listed above to expand the possible choices available to physicians, and develop materials better suited for implant as temporary bone support.

The most common metallic based implants for orthopedics are Stainless Steels, Cobalt, and Titanium based alloys [2-4]. Application of these materials as bone plates, screws, joints, and other implantable accessories (pacemaker housings) is a generally approved practice by the FDA (Table 1.1) [4].

Table 1.1: Common metallic biomaterial use and FDA classification

Type	Primary Utilizations	Statius of Applications	Ref.
Stainless Steels	1. Temporary devices (fracture plates, screws, hip nails, etc) (Class II) 2. Total hip replacements (Class II)	Routinely applied	[5]
Co-based alloys	3. Total joint replacements (wrought alloys) (Class II) 4. Dentistry castings (Class II)	Routinely applied	[5]
Ti-based alloys	5. Stem and cup of total hip replacements with CoCrMo or ceramic femoral heads (Class II) 6. Other permanent devices (nails, pacemakers) (Class III)	Routinely applied	[5]
Miscellaneous others			
NiTi	1. Orthodontic dental archwires (Class I)	FDA approved	[6]
	2. Vascular stents (Class III)	FDA approved	
	3. Vena cava filter (Class II)	FDA approved	
	4. Intracranial aneurysm clips (Class II)	FDA approved	
	5. Contractile artificial muscles for an artificial heart (Class III)	Research	
	6. Catheter guide wires (Class II)	FDA approved	
	7. Orthopedic stables (Class I)	FDA approved	
Mg	Biodegradable orthopedic implants (Class III)	Animal trial	[2,7]
Ta	8. Wire sutures for plastic surgery and neurosurgery (Class III)	FDA approved	[8]
	9. A radiographic marker (Class II)	FDA approved	

Success of Steel, Co, and Ti alloy materials in orthopedic applications is owed to their excellent strength, biocompatibility, and corrosion resistance [3]. However, there is concern of reduction in biocompatibility in these materials brought on by wear of the implant and release of metallic ions into the blood [9, 10]. Furthermore, a stress shielding effect, leading to bone resorption, can occur with materials which are much stronger than the bone tissue they support [11]. As a result, research interest has steered toward use of alloys and materials which more closely match the mechanical properties of human bone, such as magnesium.

Table 1.2: Mechanical properties of common orthopedic materials compared to bone [2]

Properties	Natural Bone	Magnesium	Ti alloy	Co-Cr alloy	Stainless steel	Synthetic hydroxyapatite
Density (g/cm^3)	1.8-2.1	1.74-2.0	4.4-4.5	8.3-9.2	7.9-8.1	3.1
Elastic modulus (GPa)	3-20	41-45	110-117	230	189-205	73-117
Compressive yield strength (MPa)	130-180	65-100	758-1117	450-1000	170-310	600
Fracture toughness ($MPam^{1/2}$)	3-6	15-40	55-115	--	50-200	0.7

Magnesium based materials, which may be absorbed by the body as the damaged bone heals, hold added benefit as they reduce the requirement for follow-up surgical procedures. Current permanent metallic implants, such as titanium screws, may require removal after repair which increases medical cost and pain to patient [12].

Magnesium alloys provide a potential solution to the primary concerns expressed above for metallic orthopedic implants. In addition to mechanical strength and modulus closer to that of bone, magnesium degrades in the body providing a basis for a biodegradable implant material [13, 14]. Magnesium is an important element in the body with deficiency linked to muscle cramps, mental confusion, nausea, and weakness [15]. Over half of the Mg in the human body is found in bone tissues and a low magnesium diet is believed to adversely affect bone strength as has been shown in rats [15-17]. Use of magnesium as the basis for an implant material is limited by rapid corrosion within the body which produces excessive hydrogen gas which could delay healing and affect local pH [16].

1.2 Corrosion of Magnesium

In air, magnesium forms an oxide coating which can provide some protection to corrosion. When exposed to an aqueous environment, magnesium hydroxide is formed following reaction (1). This $Mg(OH)_2$ film layer can be stable and protective at a pH higher than 10 [18]. However, at a physiologic pH of 7.4 the film can be broken down per reaction (2) [19].

$$MgO + H_2O = Mg(OH)_2 \quad (1)$$

$$Mg(OH)_2 + 2H^+ = Mg^{2+} + 2H_2O \quad (2)$$

As the protective film layer breaks down, corrosion of the base Mg material proceeds through the partial reactions (3) and (4) and the overall reaction (5) [18].

$$2H^+ + 2e^- = H_2 \text{ (Cathodic)} \quad (3)$$

$$2Mg = 2Mg^+ + e^- \text{ (Anodic)} \quad (4)$$

$$2Mg + 2H^+ + 2H_2O = 2Mg^{2+} + 2OH^- + 2H_2 \quad (5)$$

In a chloride rich physiologic environment, Mg and $Mg(OH)_2$ react to form $MgCl_2$ following reactions (6) and (7) [2, 20].

$$Mg + 2Cl^- = MgCl_2 \quad (6)$$

$$Mg(OH)_2 + 2Cl^- = MgCl_2 + 2OH^- \quad (7)$$

These additional reactions aid in breaking down the protective film and base Mg material, causing an accelerated corrosion of Mg in body solution.

In experiments involving coated magnesium in simulated body solution, the corrosion products vary depending on the element ions available in the solution and from the dissolution of the coating material. Common products resulting from the corrosion of Mg-Al-Zn alloys in SBF include $Mg(OH)_2$, $Mg_3(PO_4)_2$, quintinite ($Mg_4Al_2(CO_3)(OH)_{12}\cdot 3H_2O$), and hydroxyapatite ($Ca_{10}(PO_4)_6(OH)_2$) [21, 22].

1.3 Common Magnesium Alloys

A large variety of Mg alloys have been recently developed aimed at improving the corrosion resistance in situ while also maintaining and/or improving mechanical properties of the material.

Table 1.3: Common Mg alloys in medical device research [23]

Family	Representative alloys	Alloy elements (wt.%)			Main phases
Pure Mg	Mg				Mg
Mg-Al-Zn	AZ31	3Al	1Zn		Mg; $Mg_{17}Al_{12}$
	AZ91	9Al	1Zn		
Mg-Ca	Mg-xCa (x = 1, 2, 3, 4, 5, ...)	xCa			Mg; Mg_2Ca
Mg-Zn-Ca	Mg-1Zn-1Ca	1Zn	1Ca		Mg; Mg_2Ca; $Ca_2Mg_6Zn_3$
Mg-Zn-Mn-Ca	Mg-2.0Zn-1.2Mn-1Ca	2Zn	1.2Mn	1Ca	Mg; Mg_2Ca; $Ca_2Mg_6Zn_3$; $Ca_2Mg_5Zn_{13}$
Mg-Si-Ca		1Si	1Ca		Mg; Mg_2Si; SiMgCa
Mg-Zn	Mg-xZn (x = 1, 3 10)	xZn			Mg; MgZn; Mg_2Zn_3; Mg_7Zn_3
Mg-Zn-Mn	Mg-1Mn-1Zn	1Mn	1Zn		Mg; MgZn; Mg_2Zn_3; Mg_7Zn_3
Mg-Mn	Mg-1Mn	1Mn			Mg; Mn
RE containing magnesium alloy	LAE442	4Li	4Al	2RE	Mg; $Al_{11}RE_3$;
	WE43	4Y	3RE		Mg; $Mg_{12}YNd$; $Mg_{14}YNd_2$
	ZE41	4Zn	1RE		Mg; MgZn(RE)
	AE44	4Al	4RE		Mg; $Mg_{17}Al_{12}$; $Al_{11}RE_3$; $Al_{12}RE$
	Mg-xGd (x = 5, 10, 15,...)	xGd			Mg; Mg_5Cd
	WZ21	2Y	1Zn		Mg; $MgYZn_3$; Mg_7Zn_3; Mg_3YZn_6
	Mg-8Y	8Y			Mg; $Mg_{24}Y_5Mg_2Y$

Common alloy materials are Al, Mn, Zn, Ca, and some rare earths [23]. It has been seen in Mg-Al-Zn based alloys that an increase in Al content increases the corrosion resistance of these materials [24]. However, increased Al content is also linked to toxic effects in body including Alzheimer's and dementia [25, 16]. Thus, the enhanced corrosion resistance brought on by Al alloying is limited by the concern of Al exposure. AZ31 is commercially available and popular in biomedical research due to low Al content, favorable mechanical properties, and corrosion resistance [21].

1.4 Magnesium Alloy Coating Techniques

In addition to alloying, there are a variety of coating techniques being developed to further tune the corrosion performance of Mg alloys. These coatings typically fall into the classification of conversion or deposition coatings [26]. A large number of conversion and deposition coatings for magnesium-aluminum alloys have been explored involving chemical conversion [27, 28], anodization [29], sol-gel [30, 31], electrodeposition [32], and Polymer dip [33]. Table 1.4 shows a number of these studies which employed electrochemical testing to provide insight into the corrosion resistance of each coating method.

Table 1.4: Electrochemical performance of various coating methods on Mg based substrates [26]

Conditions	Substrate	i_{corr}	E_{corr}	Coating Method	i_{corr}	E_{corr}
Hanks solution 37C	AZ31	2.51×10^{-5} A/cm^2	-1.6 V (SCE)	Hydrothermal oxide / hydroxide	4×10^{-6} A/cm^2	-1.71 V (SCE)
Hanks solution 37C	Mg	400 µA/cm^2	-1.85 V (SCE)	Chemical conversion fluoride	10 µA/cm^2	-1.58 V (SCE)
MEM, 37C	Mg	6×10^{-4} A/cm^2		Chemical conversion Ca-phosphate	2.7×10^{-6} A/cm^2	
SBF 37C	Mg	380 µA/cm^2	-1.97 V (SCE)	PEO	161 µA/cm^2	-1.97 V (SCE)
Hanks solution 37,5C	AZ91	0.028703 A/cm^2	-1.5786 V	PEO	2.0456×10^{-7} A/cm^2	-0.43019 V
0.9% NaCl	AZ91D	2.256×10^{-5} A (1cm^2)		PEO Ca-phosphate various compositions	5.478×10^{-7} and 6.339×10^{-7} A (1cm^2)	
0.1 M NaCl 20+/-2C	AM50	1.8×10^{-2} mA/cm^2	-1452 mV (Ag/AgCl)	PEO Ca-phosphate in different mass ratios	Range: $3.5\text{-}23.0 \times 10^{-5}$ mA/cm^2	About -1500mV (Ag/AgCl)
SBF, 37C	AZ91	2.97×10^{-4} A/cm^2		Electrodeposition Ca-phosphate	3.65×10^{-5} A/cm^2	Decrease
Hanks solution, 37C	AZ31	2.51×10^{-5} A (1cm^2)	-1.6 V	Electrodeposition Ca-phosphate	3.98×10^{-8} A (1cm^2)	-1.42 V
0.9% NaCl 37C	Mg6Zn	26.5×10^{-6} A/cm^2	-1.46 V	Dipcoating PLGA various concentrations	0.085×10^{-6} and 0.097×10^{-6} A/cm^2	-1.44 V and -1.36 respective
SBF + Hepes 37C	Mg	2.073×10^{-4} A (1cm^2)		Dipcoating PCL	1.293×10^{-5} A (1cm^2)	Increase ΔE = 246.4mV
SBF + Hepes 37C	Mg	2.073×10^{-4} A (1cm^2)		Dipcoating PLA	3.565×10^{-5} A (1cm^2)	Increase ΔE = 120.1mV
Hanks solution, 37C	WE42			PEO and infiltration gelatin / PLGA	Decrease	Increase
SBF, 36.5 +/- 0.5C	Mg-Zn-Ca	3.36×10^{-4} A/cm^2		PEO and infiltration prospolis	1.10×10^{-6} A/cm^2	Decrease ΔE = 240mV
Hanks solution, 37C	Mg	0.25×10^{-3} A/cm^2	-1.80 V	Infiltration stearic acid various thicknesses	0.12×10^{-6} , 0.14×10^{-6} and 11.2×10^{-9} A/cm^2	-1.49, -1.46 and -1.45 V (SCE) respective
SBF, 37 +/- 0.5C	AZ91			Spraying PCL low and high porosity membrane	Decreased	Increase ΔE = 1444mV and 1114mV
SBF, 37C	AZ31	3.893×10^{-4} A/cm^2	-1.733 V	Spraying HA-chitosan, example 10% chitosan	3.144×10^{-5} A/cm^2	-1.581 V
3.5% NaCl	AZ31	4.948×10^{-5} A/cm^2	-1.455 V	N ion implantation	2.058×10^{-5} A/cm^2	-1.450 V

1.4.1 Microarc Oxidation Coating

One type of conversion coating which is of particular interest for Mg, Al, and Ti materials is the method of Microarc Oxidation (MAO) also known as Plasma Electrolytic Oxidation (PEO). MAO can be considered a form of anodization which is performed with electric potentials above the oxide breakdown voltage. As a result, discharges on the material surface produce oxides of substrate and electrolyte material grown in both directions from the substrate surface [34]. This conversion method can provide a hard, well-adhered coating which aids in wear and corrosion resistance [35, 34]. Microscopically, the produced MAO surface consists of pores and micro-cracks created by release of gases through discharge channels and the cooling of molten oxides [16].

The MAO treatment apparatus is pictured in Figure 1.1. The system consists of an electrolyte solution, stainless steel vessel (cathode), working metallic sample (anode), water cooling line, and power supply/control.

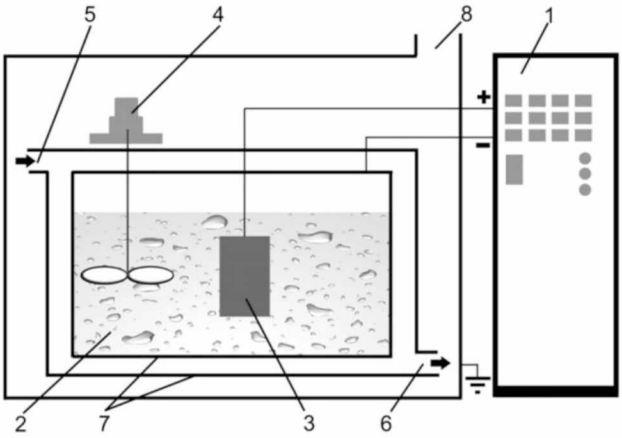

Figure 1.1: MAO Coating system. 1. Power supply unit; 2. Electrolyte; 3. Sample; 4. Stirrer; 5. Cooling water inlet; 6. Cooling water outlet; 7. Stainless-steel bath; 8. Exhaust fan [36]

Previous research has shown the dependence of corrosion performance and residual stress on process parameters such as pulse frequency, oxidation time, electrolyte concentration, and voltage [22, 36-38]. Gu demonstrated this through MAO coating formed on a substrate material of AZ31 alloy in Trisodium Phosphate (Na3PO4) electrolyte. The resulting surface was found to consist of substrate elements (Mg, Al, Zn, Mn) as well as Phosphorous and Sodium through the oxide forming interaction with the electrolyte [22, 36, 37].

1.4.2 Polymer Dip Coating

Polymer dip coatings are gaining popularity in research due to their relatively easy application methods and the ability to modify organic polymers for drug delivery or nanoparticle doping [33]. Polymer applications on an AZ31 substrate in current literature include Poly (lactic acid) (PLA) [33], Poly (lactide-co-glycolide) (PLGA) [39,40], Polycaprolactone (PCL) [39, 41], and Poly (ether imide) (PEI) [42, 43]. These biopolymers are advantageous for use in implants as they have a long history of approval and use as sutures and tissue scaffolding devices. PCL poses a slower degradation rate vs. PLGA polymers while degrading in the body through hydrolysis of ester links [44, 45]. Preliminary animal studies have been conducted in rabbits showing a promising reduction in corrosion rate for PCL coated magnesium substrates without inflammation or adverse tissue effects [46].

Surface preparation varies in literature but regularly involves polishing with SiC paper between 1200-2000 grit [40-41, 45]. The surface is then cleaned with a solvent such as ethanol or acetone to prevent foreign particles from compromising the adherence between the polymer and substrate. Common coating formulation involves mixture the raw polymer with a solvent such as Dichloromethane (DCM) in a ratio of raw polymer material weight to solution volume (%w/v). The solution is then mixed for a period of time and applied via dip, spray, spin-coat, or other application method. Process variants for application of the polymer include submersion time, rate of dip/withdrawal, and number of layers deposited.

1.5 Simulated Body Fluids for Corrosion Testing

A number of simulated body fluids have been adopted for in-vitro testing of magnesium biomaterials ranging from structural implants, to cardiovascular stents, and drug delivery mechanisms [13]. Mock body solutions provide a means of testing degradation of biomaterials prior to animal testing allowing a humane way to perform preliminary benchmarking and comparison of materials.

Body solutions which simulate the ion composition of human blood are a standard tool for the evaluation of corrosion performance of prospective orthopedic implants. Several different solutions exist which are commonly used to evaluate material corrosion which hinders the ability to easily compare results between research labs.

Table 1.5: Common Simulated Body Fluids in Literature

Concentration (mmol/L)	Na^+	K^+	Mg^{2+}	Ca^{2+}	Cl^-	HCO_3-	HPO_4^{2-}	SO_4^{2-}
Blood Plasma [47]	142	5	1.5	2.5	103	27	1	0.5
Original SBF [48]	142	5	1.5	2.5	148.8	4.2	1	0
c-SBF [48]	142	5	1.5	2.5	147.8	4.2	1	0.5
m-SBF [49]	142	5	1.5	2.5	103	10	1	0.5
Hank's Solution [50]	142	5.8	0.8	2.5	145	4.2	0.3	0.8
EBSS [51]	144	5.4	0.4	1.8	125	26	1	0.4
Minimum Essential Media (MEM) [51]	143	5.4	0.4	1.8	125	26	0.9	0.4

The largest deviation from blood plasma typically occurs with respect to chloride ions in solution. As described in Section 1.2, the breakdown of Magnesium within the body has been seen to be accelerated in a high Chloride environment making this a specific element of interest when observing corrosion in a simulated body environment. Efforts are being made to standardize solution use across research experiments, however at this time there is no established standard for body solution.

Table 1.6: Electrochemical corrosion results for AZ31 in simulated body fluids

Reference	Body Solution	Ecorr (V)	iCorr (A/cm^2)	Sample Dimensions (Exposed Area)
[24]	Hanks Solution	-1.6	2.51×10^{-5}	1cm^2
[30]	SBF 37C	-1.733	3.893×10^{-4}	
[52]	3.5% NaCl	-1.43	1.5×10^{-5}	
[53]	Various NaCl and PBS (Phosphate buffer solution)		Phosphate ions hinder attack compared to chloride ions	1cm^2
[54]	NaCl 5g/L	-1.33	3.54×10^{-6}	
	NaCl 10 g/L	-1.41	1.24×10^{-5}	
	NaCl 35g/L	-1.43	1.77×10^{-4}	
	PBS	-1.24	1.43×10^{-5}	
[24]	m-SBF	-1.273	3.274×10^{-5}	1cm^2
[55]	Hanks Solution		8.155×10^{-5}	1cm^2
	DMEM		1.514×10^{-5}	
	DMEM+FBS		0.468×10^{-5}	
[36]	SBF	-1.30	10.1×10^{-5}	4.18cm^2
[40]	DMEM + FBS	-1.54	3.10×10^{-5}	1.25 x 1.25 x 0.08 cm

Several studies have shown the solution dependency of corrosion results in simulated, 'in vitro' environments (Table 1.6). In these studies, corrosion current, an electrochemical metric related to corrosion rate, varies widely between solutions both within and across research experiments. Yang contributed a similar solution dependency in Mg-Mn-Zn alloy to ion composition differences between Hank's Solution and a Simulated Blood Plasma [56].

Table 1.7: In vivo vs. in vitro corrosion testing on magnesium alloys

Reference	Material	In vivo Model	In vitro Solution(s)	Observations
[57]	AZ91D LAE442	Guinea Pig Femur	Substitue Salt Water (ASTM-D1141-98)	In vivo corrosion rates four orders of magnitude smaller than in vitro.
[58]	AZ31B	Rabbit	Hank's Solution	Degradation rate of 0.3mm/yr in vitro. Implant appeared to degrade in rabbit without adverse tissue reactions.
[51]	AZ31 Mg-0.8Ca Mg-1Zn Mg-1Mn Mg-1.34Ca-3Zn	Lewis Rat	EBSS MEM MEMp (HEPES and NaHCO3 buffer schemes)	Weight loss is lowest with NaHCO3 buffer method. EBSS vs. in vivo corrosion rates not significantly different.
[50]	Mg WZ21	Wistar Rat	Nor Solution (CO_2-Bicarbonate Hank's Solution)	Agreement for in vivo vs. in vitro corrosion rates for Mg and WZ21. AZ91 corrosion rate significantly higher in vitro.
[59]	Mg coated with Monetite and Brushite	Lewis Rat	EBSS MEM MEMp (NaHCO3 buffer)	No significant difference between EBSS and in vivo corrosion rates.

Efforts have been made to compare in-vivo and in-vitro degradation through animal studies vs. benchtop corrosion testing (Table 1.7). Witte found lower overall corrosion of Mg alloy implants in vivo compared to immersion in a simulated body solution. Increased chloride content in the simulated environment compared to actual body fluid was cited as the reason for this discrepancy [57]. Use of a CO_2 – Bicarbonate buffer has been employed in order to match the biological buffering mechanism in the body [50, 51]. Abidin found good agreement between in vivo and in vitro corrosion rate results for CO_2 buffered Hank's Solution for Mg and WZ21 alloy. However, these results did not show good agreement for AZ91 alloy which was attributed to manufacturing techniques [50]. Walker explored in vivo vs. in vitro results through use of Lewis rats and benchtop immersion weight loss testing in SBF (MEM, MEMp, EBSS).

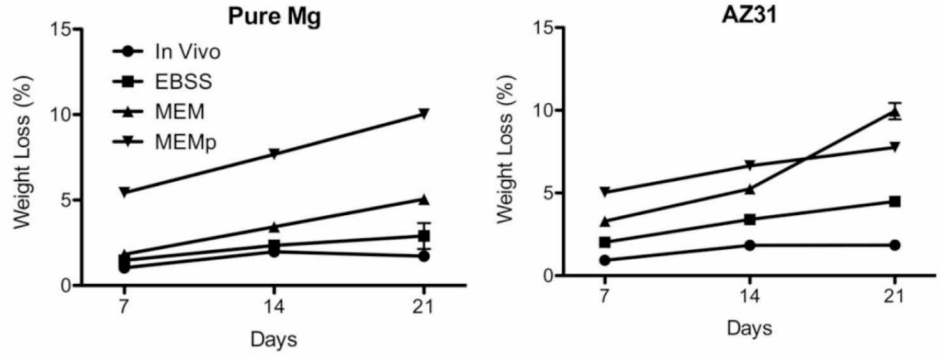

Figure 1.2: Weight loss immersion study with various simulated body fluids compared to in vivo (rat) results [51]

The results of the solution comparison testing showed no significant difference in corrosion rate between EBSS and the in vivo testing. Walker concluded that EBSS is an appropriate predictor of in vivo corrosion performance, and could be used to reduce animal testing when comparing a range of early stage implant concepts [51]. These results were also found in an additional study of coated Mg by Shadanbaz [59].

1.5.1 Kokubo Simulated Body Fluid

Kokubo's SBF (and updated versions) are often used as a tool for in vitro assessment of apatite formation, a corrosion product which may be beneficial to bone growth [60, 2]. However, traditional SBF and c-SBF has a concentration lower in HCO-3 and higher in Cl- than blood plasma. This is believed to affect the composition of apatite formation and may not be representative of bone apatite [61]. Oyane compared stability of improved c-SBF variants in an effort to produce a solution which more closely matches the ion concentration in blood plasma [49]. A round robin series of testing was reported by Takadama that

looked at an improved ion concentration SBF vs. c-SBF for purposes of apatite formation and found that the improved solution and traditional c-SBF produce similar results [62]. This result ultimately led to an improved preparation process for c-SBF but no further update to the reagent amounts used in the solution [48]. The c-SBF is prepared by combining reagents, shown in Table 1.8, into deionized H_2O around 37°C. The buffering mechanism for this solution is the combination of Tris $(CH_2OH)_3CNH_2$ and HCl.

Table 1.8: Composition of reagents of SBF solutions c-SBF and EBSS based on 1000ml produced volume

Reagent	c-SBF [48]	EBSS [63]
NaCl	8.035g	6.80g
$NaHCO_3$	0.355g	2.20g
KCl	0.225g	0.40g
K_2HPO_4-$3H_2O$	0.231g	--
$MgCl_2$-$6H_2O$	0.311g	--
1 kmol/m^3 HCl	39ml	--
$CaCl_2$	0.292g	0.20g
Na_2SO_4	0.072g	--
$(CH_2OH)_3CNH_2$	6.118g	--
1 kmol/m^3 HCl	0-5 ml	--
$MgSO_4$	--	0.10g
NaH_2PO_4-H_2O	--	0.125g
Glucose	--	1.00g

1.5.2 Earle's Balanced Salt Solution

Earle's Balanced Salt Solution has been used as a component of cell culture media for many years, originally used in fibroblast culture studies in mice [64]. Recently, use of this salt solution has been applied to in vivo vs. in vitro corrosion studies due to the close ion composition similarity to blood plasma and biological buffering mechanisms, Table 1.5. Yamamoto compared corrosion rates of pure magnesium in six body solution variants and concluded that the EBSS solution variants were most fitting for in vitro evaluation of magnesium degradation [65]. These results are supported by in vivo vs. in vitro tests performed by Walker and Shadanbaz [51, 59]. EBSS can be purchased commercially or produced by combining the reagents listed in Table 1.8 and buffering through CO_2 bubbling. For the experiments outlined in Chapters two and three, the Kokubo (c-SBF) and Bryant (EBSS) formulations were chosen. The estimated ion concentrations of these solutions are shown in Table 1.9.

Table 1.9: Estimated ion concentrations of SBF solutions c-SBF and EBSS

Ion	Ion concentration (mmol/L) Blood Plasma [47]	c-SBF [48]	EBSS [Calculated]
Na^+	142.0	142.0	143.6
K^+	5.0	5.0	5.4
Mg^{2+}	1.5	1.5	0.8
Ca^{2+}	2.5	2.5	1.8
Cl^-	103.0	147.8	125.3
HCO_3^-	27.0	4.2	26.2
HPO_4^{2-}	1	1	1
SO_4^{2-}	0.5	0.5	0.8
pH	7.2-7.4	7.2-7.4	7.2-7.4

1.6 Immersion Corrosion Testing

Multiple time-point immersion testing is a common method for evaluating the change in morphology and corrosion rate of a material in solution. Methods for evaluating corrosion rate through immersion of magnesium alloys have included weight loss studies [56, 46, 66] and hydrogen evolution rate [67, 68]. Morphological changes are typically assessed through microscopy and SEM/SEM imaging. Criticisms of weight loss and hydrogen evolution testing include the need to account for variation between sample, difficulty in obtaining an accurate measurement, and lack of information on the corrosion mechanisms at work [69]. To better analyze long term corrosion samples, immersion testing is often paired with electrochemical testing after an immersion endpoint has been reached. This provides an opportunity to measure both morphological changes as well as electrochemical properties of corroding samples.

1.7 Electrochemical Testing

Measures of the electrochemical interaction between a working electrode (corroding specimen) and the surrounding electrolyte can provide insight into corrosion rate and resistance of protection layers. Electrochemical testing for evaluation of Mg corrosion in SBF is typically performed using a three-electrode corrosion cell as shown below:

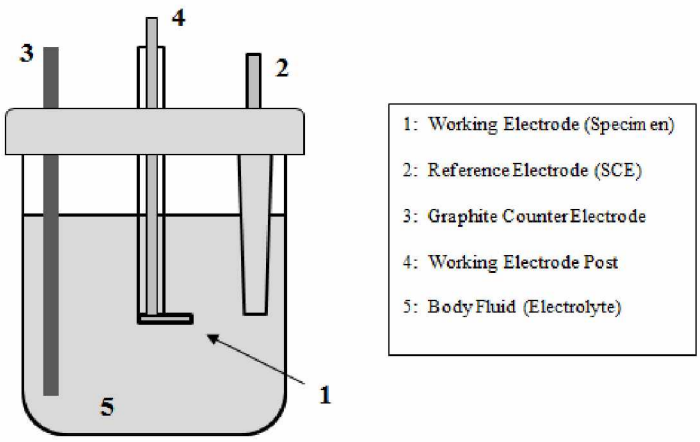

Figure 1.3: Basic schematic of three electrode corrosion cell

Electrode terminals (2, 3, 4) are connected to potentiostat equipment to control the applied voltage and current as well as monitor the output signal from the cell.

1.7.1 Electrochemical Impedance Spectroscopy (EIS)

EIS is an electrochemical test method in which a small sinusoidal potential (e.g. 10mV) is applied to the sample (working electrode) with a resulting current measured via reference electrode (Saturated Calomel Electrode). The ratio of the time dependent input, *V(t)*, and output *i(t)* provide the basis of the circuit impedance. The sinusoidal potential is determined through dependency on frequency in the relationship $\omega = 2\pi f$, where f is the frequency and ω is radial frequency. For an EIS corrosion experiment, this relationship is typically observed from a frequency (f) as high as 100kHz to as low as 1mHz [70]. System input and response is represented by the equations below:

$$Input\ Voltage: \quad V(t) = V_0 \cdot sin(\omega t) \tag{8}$$

$$System\ Response: \quad i(t) = i_0 \cdot sin(\omega t + \phi) \tag{9}$$

$$Impedance: \quad Z(\omega) = \frac{V(t)}{i(t)} = \frac{V_0 \cdot sin(\omega t)}{i_0 \cdot sin(\omega t + \phi)} = Z_0 \left(\frac{sin(\omega t)}{sin(\omega t + \phi)}\right) \tag{10}$$

Where ϕ is the phase shift between the input voltage and the delayed system response. An alternate form of this relationship involves use of real $Z'(\omega)$ and imaginary $Z''(\omega)$ components of impedance:

$$Z(\omega) = Z'(\omega) + jZ''(\omega) \tag{11}$$

From these results a series of plots can be created to observe the impedance of a sample, most commonly Nyquist and Bode plots [71, 72]. Performance of an electrochemical system on Nyquist and Bode plots can be imitated by a combination of resistors and capacitors in a circuit referred to as an 'Equivalent Circuit'. A simple demonstration of this fitting method is called the Randles Cell shown below:

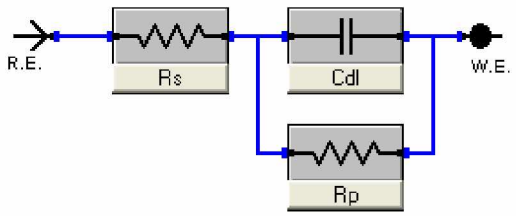

Figure 1.4: The Randles cell is a common starting point for EIS equivalent circuit analysis

Where, R_s, is the resistance of the electrolyte surrounding the electrode (corroding metal), R_p is the polarization resistance of the corroding metal, and C_{dl} is the double layer capacitance of the electrode. At a low frequency, the capacitor impedance is very high resulting in the simplified circuit of $R_s + R_p$. Conversely, at a high frequency the impedance of the capacitor component becomes very small resulting in an overall impedance of just R_s [72]. This relationship allows the separation of R_p to be used as a metric for comparing corrosion resistance between coatings. In this way, knowledge of coating resistance components through EIS may be used as a quality control method [70]. In contrast to the simple example above, finding an appropriate equivalent circuit may require additional resistance and capacitance elements to represent all layers of a corroding surface.

Use of a constant phase element (CPE) has been found to improve the fit of EIS results to equivalent circuits as defined by the equation [73, 74]:

$$Z_{CPE} = \frac{1}{Y_0(jw)^{\alpha}} \tag{12}$$

Where Y_o is constant, $j = \sqrt{-1}$, $\omega = 2\pi f$, and $\alpha = 0$ or 1. For the case of capacitance, $Y_o = C$ and $\alpha = 1$. This use of the CPE is referred to as an 'imperfect capacitor' and simulates a double layer capacitor [74].

1.7.1.1 Coated Substrate Equivalent Circuit

A number of studies have presented equivalent circuits for MAO [36, 73, 75] and polymer [76, 77] coated surfaces. These circuits generally consist of 3 or more resistors with 2 or more CPEs to best fit the bode impedance plots. The basic circuit shown below was used to fit the EIS data presented in the experiments

outlined in Chapters 2 and 3. The circuit is shown between the reference electrode (R.E.) and working electrode (W.E.).

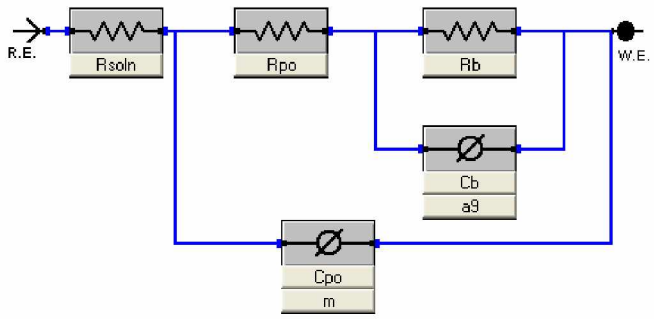

Figure 1.5: Equivalent circuit for coated material corrosion in SBF

The resistance components are the solution resistance, R_s, porous outer layer resistance, R_{po}, and polarization resistance of the substrate-solution interface, R_b, also called the 'barrier' layer of the coating [36]. C_b and C_{po} are the corresponding CPEs for the barrier and porous layers.

1.7.2 Potentiodynamic Polarization

Potentiodynamic polarization scans are conducted by varying electric potential over a range below (cathodic) and above (anodic) the corrosion potential E_{corr}. The potential is regulated via the current flowing through the electrolyte environment between a counter electrode (e.g. Graphite rod) and the working electrode (specimen). The sweep rate is measured in mV/s and usually falls around 1 mV/s for corrosion studies involving magnesium alloys in simulated body fluid [69]. The test returns values of current density (A/cm^2) at each of the swept potentials. Analysis of the polarization curve can provide insight into E_{corr}, I_{corr}, cathodic, and anodic kinetics.

When cathodic and anodic regions of the polarization curve are linear, a Tafel extrapolation can be performed to determine the corrosion current density (I_{corr}) and tafel constants (βa, βc). The polarization resistance, R_p, is related to I_{corr} through the Stern-Geary equation:

$$R_p = \frac{\beta_a \beta_c}{2.3 \cdot I_{corr} \cdot (\beta_a + \beta_c)} \tag{13}$$

The corrosion density and polarization resistance can then be compared directly between samples or converted to a corrosion rate, CR, using Equation 14 below:

$$CR = \frac{3.27x10^{-3} \cdot i_{Corr} \cdot (EW)}{\rho} \quad (14)$$

Where I_{corr} is expressed in units of $\mu A/cm^2$, EW is equivalent weight of sample, and density is in g/cm3. When units of K (3.27x10-3) are mm · g/μA·cm·yr, EW is unitless and CR is output in mm/yr [78, 70]. As EW and density can be considered approximately constant across samples, comparison of I_{corr} simply reflects the corrosion rate of the sample. Furthermore, since Mg typically does not corrode uniformly, it is common practice to compare I_{corr}, as an indication of corrosion severity [69]. As the Potentiodynamic curve shifts to higher current density it can be expected that the corrosion rate is increasing for the sample. Also, for higher open circuit potentials the sample can be considered more passive. These relationships, defined above, in addition to pitting potential observations in the anodic region allow qualitative interpretations of polarization curves when data may not allow for mathematical modeling.

1.8 Mechanical Corrosion Tests

The in-service performance of an implantable medical device is of primary importance when evaluating the viability of a new concept. Specifically, orthopedic implants are subjected to continuous and cyclic loading due to their use as a bone tissue support material. In this respect, a biodegradable implant material, such as magnesium, will be subjected to a combined degrading effect of corrosion and mechanical loading. This configuration has led to the exploration of a specific failure type called Stress Corrosion Cracking (SCC). SCC is the failure of a part/material when subjected to combined corrosion and mechanical loading through propagation of a crack induced by the corrosion environment.

Stresses required for SCC to occur are typically below the yield stress and applied in tension [70]. Many alloys, including existing orthopedic implants have been shown to be susceptible to SCC with influencing factors (environment compositions) varying between materials [70, 79]. Mg alloys have been demonstrated to be susceptible to SCC in chloride environments [18]. Also, alloys which have increasingly high Al content have been shown to have increasing susceptibility to SCC failure [80]. A variety of mechanism models have been proposed to explain SCC propagation, with the most accepted being a combination of anodic dissolution of material and hydrogen embrittlement at the crack tip.

Experimental observation of SCC behavior is typically performed using static loading (constant deflection) or slow strain rate testing ('quasi static') while the material is subjected to a corrosive environment. Results of these tests are reported in time to failure or ratio of performance in corrosive environment vs. performance in air (% Elongation, UTS, YS, etc).

Table 1.10: Stress Corrosion Studies on Mg-Zn alloys

Reference	Material	Corrosive Environment	Test Types	Results
[81]	AZ31	NaCl (0.5%, 3%, 8%)	***Constant Tensile Load*** - Pre-notched Specimen - Load increased every 24h - Crack growth monitored	Crack growth accelerated with increased NaCl concentration
[82]	Mg-Zn-Ca Alloy w/Ca-P Electrodeposition	SBF	***SSRT*** -Cylindrical specimens (10mm x 4mm Dia) - Strain rate: 2.16 x 10^{-5} mm/s	UTS: 152 MPa (SBF); 175 MPa (Air) Mg-Zn-Ca is not highly susceptible to SCC
[83]	Al-Zn-Mg-Cu-Zr Alloy	3.5 wt% NaCl	***SSRT (ASTM G129)*** -Flat Dog-bone specimen - Strain rate: $10^{-6}s^{-1}$ ***Constant Extension (ASTM G30)*** - U-Bend Specimen - 134 x 9 mm Rectangle - Held in solution until failure or cracks visible under microscope	SSRT: - UTS: 515 MPa (3.5% NaCl); 561 MPa (Air) Constant Extension: - U-bend sample failed in 17-20h
[84]	AZ91	m-SBF	***SSRT*** - Cylindrical specimens (10mm x 4mm Dia) - Strain rate: 1.2 x $10^{-7}s^{-1}$	UTS: 100 MPa (m-SBF); 120 MPa (Air) Elongation (Fracture): 3.7% (m-SBF); 4.7% (Air) SCC susceptibility in sand-cast AZ91 is not substantial
[85]	AZ91D	m-SBF	***SSRT*** - Cylindrical specimens (20mm x 3mm Dia) - Strain rate range: 1.2 x 10^{-7} to 4.3 x $10^{-7}s^{-1}$	Strain Rate: I_{SCC} (UTS) - 1.2 x 10^{-7}: 0.48 - 2.2 x 10^{-7}: 0.52 - 4.3 x 10^{-7}: 0.76 AZ91D is susceptible to SCC in m-sbf at low strains
[86]	AZ31 AZ91 AM30	Double distilled H_2O	***Constant Extention Rate Test (CERT) and Linear Increasing Stress Test (LIST)*** - Cylindrical specimens (5mm Dia waist) - Strain rate (Air): $10^{-4}s^{-1}$ - Strain rate range (H_2O): 3 x $10^{-8}s^{-1}$ to 50 x $10^{-8}s^{-1}$	Material : I_{SCC} Range (UTS) AZ31: 0.42-0.68 AZ91: 0.33-0.45 AM30: 0.57-0.61 All alloys investigated were susceptible to SCC in distilled water SCC increased with decreasing strain rate for all alloys
[87]	AZ31 various grain sizes (UFG, FG, BM)	3.5 wt% NaCl	***SSRT*** - Flat Dog-bone specimen - Strain rate: $10^{-6}s^{-1}$	UTS: UFG: 119 Mpa (3.5% NaCl); 172 Mpa (Air) FG: 136 Mpa (3.5% NaCl); 174 Mpa (Air) BM: 177 Mpa (3.5% NaCl); 192 Mpa (Air) Processed materials showed higher susceptibility than 'base material' (as received).
[88]	AZ31	Distilled Water ASTM D1387 solution 0.01 M NaCl	***SSRT*** - Flat Dog-bone specimen - Strain rate: 1 x $10^{-6}s^{-1}$	Longitudinal and transverse AZ31 sheet orientations demonstrated SCC in variuos solutions.
[89]	AZ31B with laser shock processing	1 wt% NaOH	***Constant Extension Testing*** -Rectangular specimen 150mm x 40mm x 2mm - 3-point bending - 5mm maximum deflection - 500h immersion time	LSP retards SCC initiation and propagation of pre-cracks on AZ31B.

1.8.1 Constant Extension Testing

Constant extension testing ('bent beam' or 'constant deflection' testing) involves the static loading of a specimen at a fixed deflection within a corrosive environment. Testing typically is performed via two, three, or four-point bending with guidance available in ASTM standard G39. The bent beam testing described in ASTM G39 generally applies to small deflection samples (prior to yield stress). Materials are chosen which resist corrosion and prevent galvanic coupling effects between the specimen and fixture contact points.

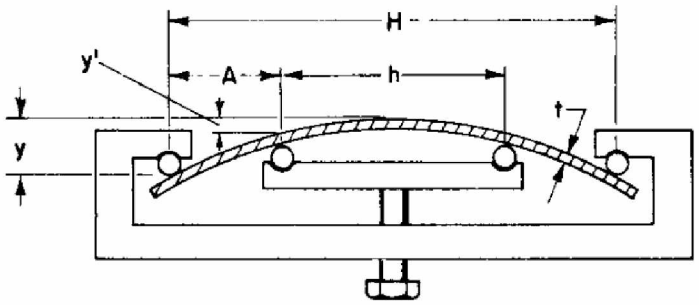

Figure 1.6: Four-point constant extension testing jig [90]

Specimens are subjected to the constant extension stress until failure/cracking occurs. Test outputs are time to failure at a given stress/extension position. The amount of applied deflection can be varied between samples in order to understand the influence of increasing stress on time to failure. For the experiment in Chapter 3, constant extension is combined with weight loss to compare the corrosion between unstressed and stressed samples.

1.9 Problem Statement and Scope of Experiments

The primary focus of this research involves the comparison of corrosion progression through MAO coating caused by two different simulated body fluids (c-SBF and EBSS). A secondary goal is the characterization of corrosion of a simple polymer dip-coating and the effect of loading on corrosion resistance. These experiments employ common elements of immersion testing, macroscopic evaluation, and electrochemical testing. The unique rationale and scope for each experiment is further explained in their respective chapters.

Chapter 2: Comparative Corrosion Performance of Process-varied MAO Coatings on AZ31 Alloy in c-SBF vs. EBSS

2.1 Test Rationale and Strategy

Recently, work has been done to understand the effect of process variation on MAO coating corrosion performance [22, 36]. This research used SBF (Kokubo), which has been suspected of overestimating corrosion rates for in vitro testing due to excessive chloride ions in the solution. Existing solutions, based on Earle's Balanced Salt Solution, have since been tested in vivo vs. in vitro and were found to show comparable results [51, 59]. The research outlined in Chapter 2, compares c-SBF and EBSS in vitro corrosion testing to understand the gap in corrosion rates between the solutions. The experiment also involves the evaluation of process varied MAO samples in EBSS which has not been observed in publications. A better understanding of the corrosion rate variations between the simulated solutions is required to understand whether performance of current MAO coatings is sufficient or excessive. This knowledge may also guide planning of animal studies with regards to expected implant time. A closer estimate of in vivo performance may limit the amount of animal studies required which is desired in medical device development. The process variations to be used to develop MAO samples are shown in Table 2.1 with the test outline for this experiment shown in Figure 2.1.

Table 2.1: MAO processing groups for the experiment outlined in Chapter 2

Group	Voltage	Frequency (Hz)	Duty Cycle	Deposition Period
1	250	100	0.3	5 min
2	300	100	0.3	5 min
3	325	100	0.3	5 min
4	350	100	0.3	5 min
5	325	300	0.3	5 min
6	325	500	0.3	5 min
7	325	1000	0.3	5 min
8	325	3000	0.3	5 min
9	Uncoated	--	--	--

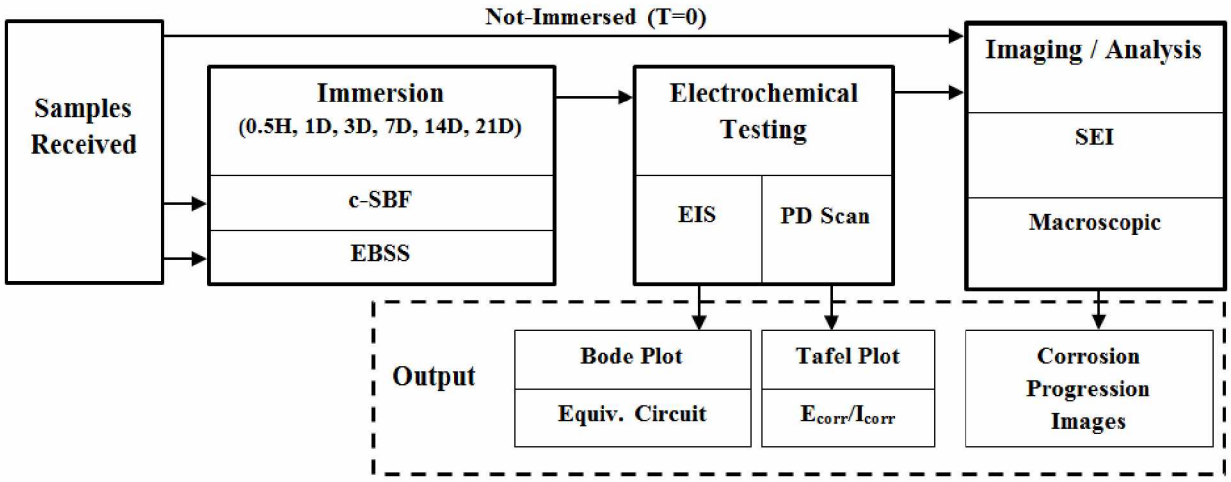

Figure 2.1: Test path for MAO coated AZ31 in c-SBF vs. EBSS

2.2 Experimental Setup

2.2.1 Sample Preparation

Substrate material AZ31 (2.5-3.5wt% Al, 0.7-1.3wt% Zn, 0.2-1.0wt% Mn, 0.05wt% Si, 0.01wt% Cu, and Mg balance) was cut to 20mm x 20mm x1mm and polished with SiC paper to a roughness of approximately 1.6μm. The samples were then cleaned ultrasonically in preparation for MAO treatment in an electrolyte bath of 10g/L Na_3PO_4 in distilled water. MAO was performed using MAD-20 (Chengdu PULSETECH Electrical Co., LTD China). The apparatus included stainless steel bath (cathode), AZ31 substrate (anode), stirring, and cooling system. Process parameters were varied to produce run groups corresponding to constant voltages of 250V, 300V, 325V, and 350V at a pulse frequency of 100Hz and deposition time of 5 minutes. Likewise, pulse frequency was varied producing additional run groups of 300Hz, 500Hz, 1000Hz, and 3000Hz at a constant voltage of 325V and 5 minutes deposition time. Samples for immersion were then cut to 10 x 10 x 1mm, including an uncoated variation, resulting in nine total test groups.

2.2.2 Immersion Solutions and Timepoints

Two SBF variants (c-SBF and EBSS) were produced for immersion and electrochemical testing with ion compositions shown in Table 1.9. All solution preparation, sample immersion, and electrochemical testing was conducted within a pH range of 7.2-7.4 at 37°C. The c-SBF solution was buffered with Tris (hydroxymethyle) minomethane $(CH_2OH)_3CNH_2$ and pH adjusted using 1 kmol/m^3 HCl. The solution was prepared by combining the reagents (Table 1.8) in order in deionized water with constant stirring. The EBSS solution was produced by combining NaCl, $NaHCO_3$, KCl, $MgSO_4$, NaH_2PO_4-H_2O, and Glucose in deionized water with constant stirring. The portion of $CaCl_2$ was dissolved separate in 150ml

deionized water then added to the salt solution. The pH of EBSS was adjusted to 7.2-7.4 by bubbling CO_2 through the solution. A specimen from each group, for each body solution (c-SBF or EBSS), was immersed in 50ml (0.20ml/mm^2) of SBF for periods of 0.5hr, 1d, 3d, 7d, 14d, and 21d with solution replaced daily.

2.2.3 Electrochemical Testing

The electrochemical equipment used was a 3-cell system consisting of glass test vessel, graphite counter electrode, SCE (saturated calomel electrode), and the working electrode (Specimen). The system was driven by a Gamry G300 potentiostat and Echem Analysis software. Samples removed from immersion at each timepoint were rinsed with DI water and attached to the electrochemical working electrode post and immersed in 300ml of the solution of interest (EBSS or c-SBF) at 37±2°C. The non-specimen portion of the working electrode rod was coated in wax, leaving an exposed specimen area of approximately 1.86cm^2. The specimen was immersed for 10 minutes prior to monitoring of Open Circuit Potential (10 minutes), EIS, and Potentiodynamic Scans. Electrochemical Impedance Spectroscopy (EIS) was conducted in the range of 100kHz to 0.2Hz with an AC voltage amplitude of 10mv. Potentiodynamic scans were conducted at a rate of 1mV/s.

2.2.4 Sample Characterization and Morphology

Non-corroded specimens from each process setting were potted in epoxy, cross-sectioned, and carbon coated for Energy Dispersive Spectrometry (EDS) mapping. EDS was performed at 20kev and 20nA. NSS analysis software was used to capture EDS map of cross section and measure thickness of MAO coating. Coating boundaries were determined by viewing phosphorous elemental map overlay on SEM image. Samples removed from immersion were digitally photographed before and after electrochemical testing. Secondary Electron Imaging was performed to observe differences in morphology between timepoints. SEM images were captured at 2500x, 1000x, and 200x, using a JEOL JXA-8530F electron microprobe (20kev, 20nA).

2.3 Results

2.3.1 MAO Coating Surface Imaging and Thickness

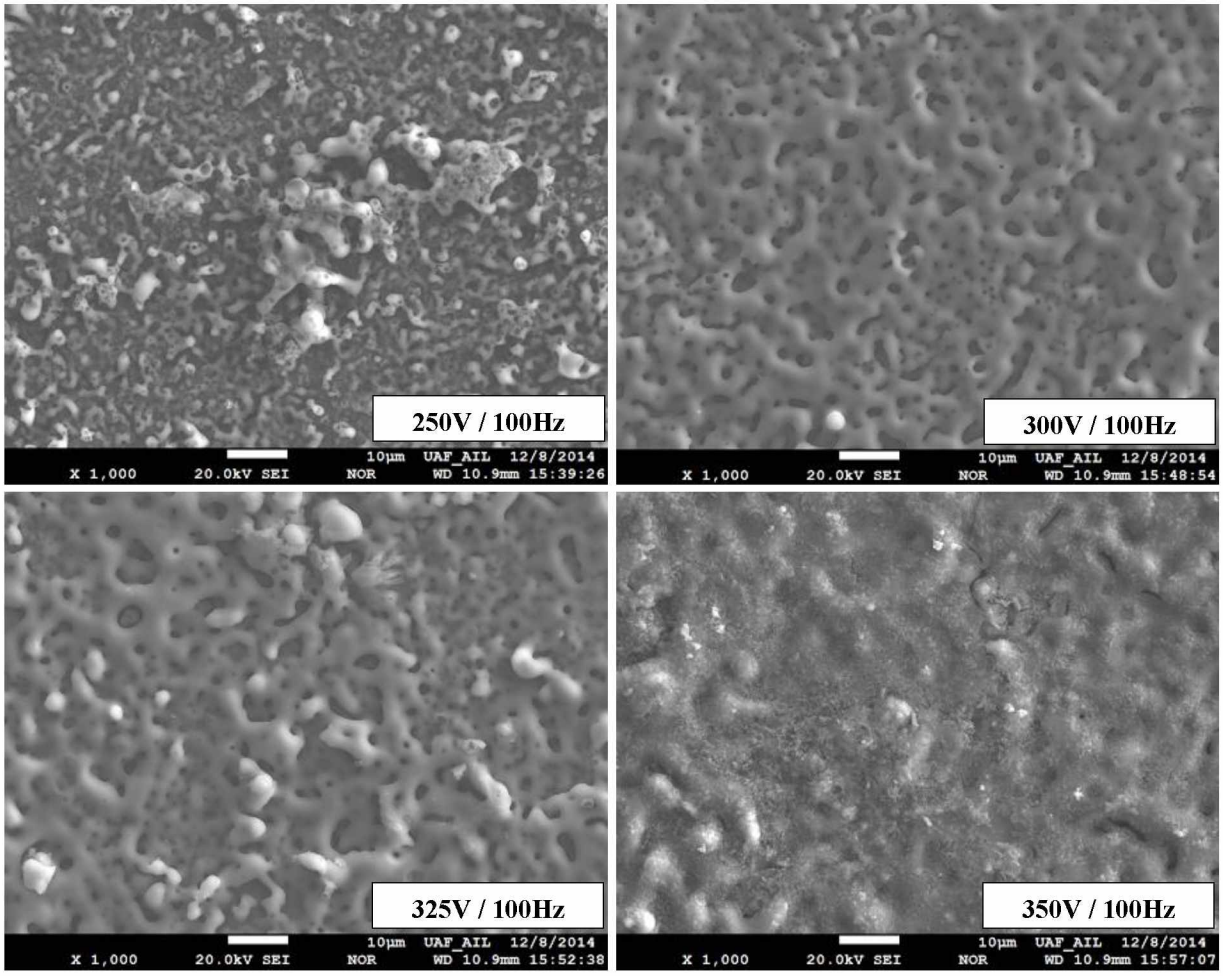

Figure 2.2: SEM imaging (1000x) of MAO surface prior to corrosion testing for groups of increasing voltage, Group 1 (top left), Group 2 (top right), Group 3 (bottom left), Group 4 (bottom right)

At 250V surface contains many small 'finger-like' projections from the surface and pores are visible along the projections typically below 1µm in diameter. With increasing voltage (300V and 325V) the small pores grow in size and surface appears more homogenous without the uneven projections seen at 250V. Pore diameter is similar at 300V and 325V ranging from 1-5µm. Very small micro-cracks appear at 325V. At 350V surface appears much less porous than 325V with 'flakey' rough surface replacing the smooth struts between pores at 300V and 325V.

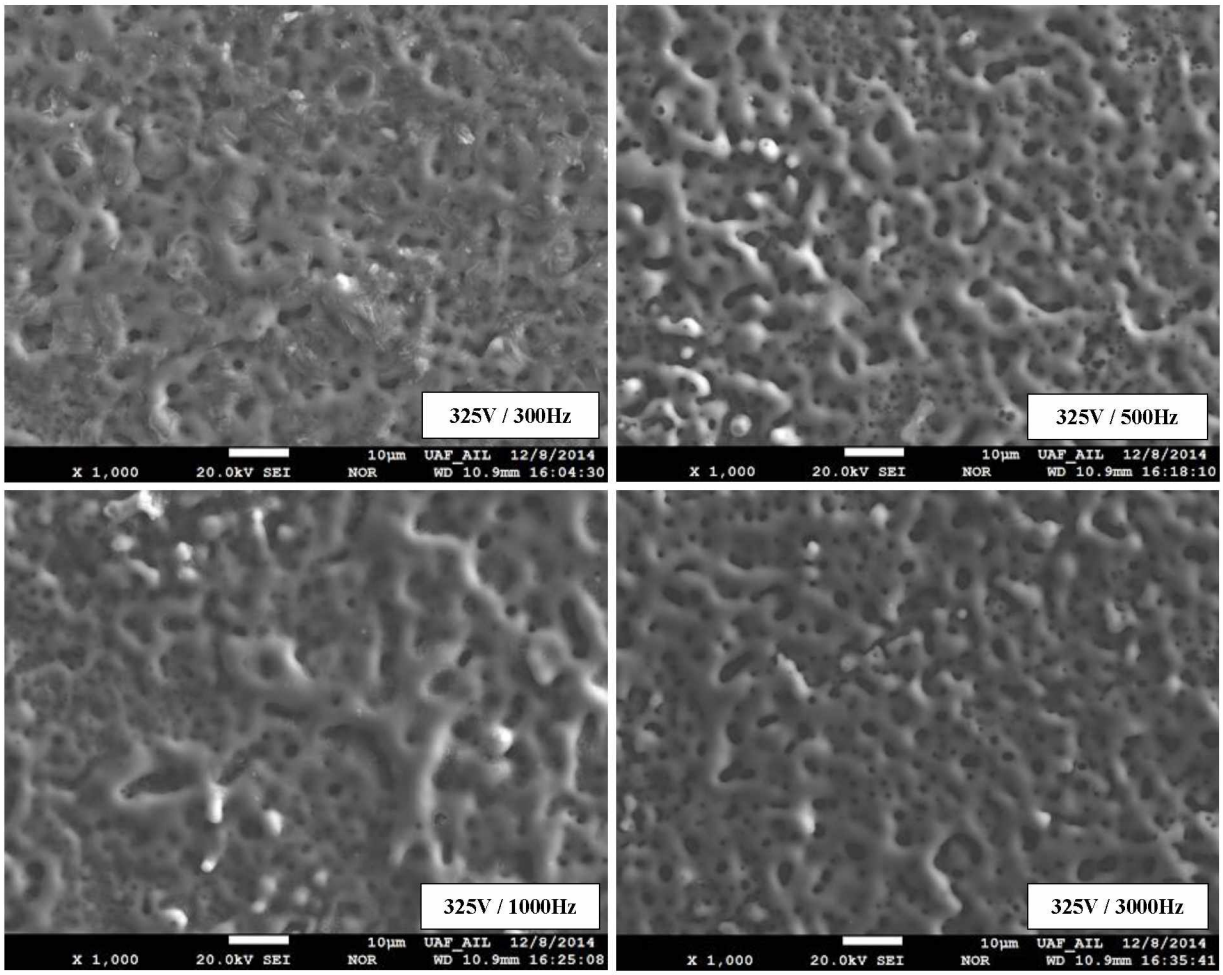

Figure 2.3: SEM imaging (1000x) of MAO surface prior to corrosion for groups of increasing frequency, Group 5 (top left), Group 6 (top right), Group 7 (bottom left), Group 8 (bottom right)

At 100Hz (Figure 2.2) and 300Hz the surface has many consistently spaced pores on the order of 1-5µm. As frequency moves to 500Hz, the number of visible micro-pores (<1µm) increases, appearing in place of the previously smooth struts between pores at 100Hz and 300Hz. Many larger pores, up to 10µm, become present at 500Hz. At 1000Hz the largest pores continue to expand while the micro-pores fade into the surface, now appearing as 'fuzzy' regions on the MAO struts. Pore size for 500Hz and 3000Hz is very similar with some micro-cracks visible on 3000Hz surface. Visible changes on the surface with frequency are not dramatic with a small increase in pore size appearing up to 1000Hz.

On cross-section, MAO coating boundaries are not easily delineated through SEM imaging alone, therefore EDS mapping was used to show high phosphorous concentration regions as shown in Figure 2.4 below.

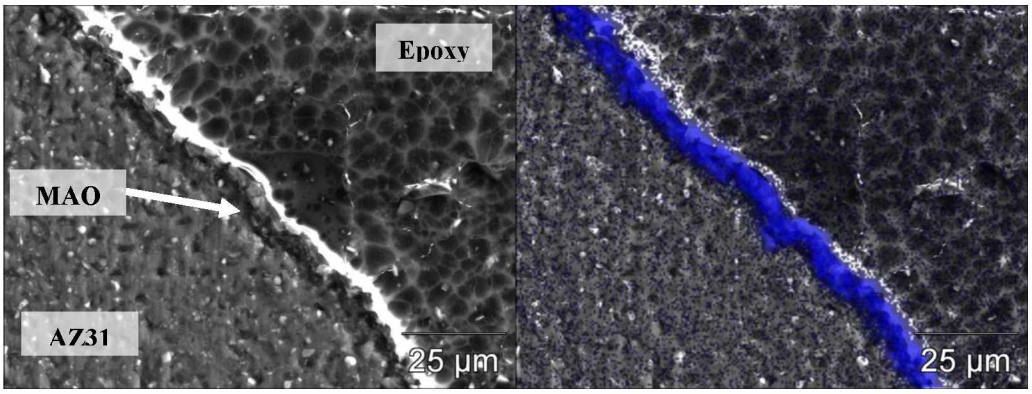

Figure 2.4: Cross section of 325V 300Hz MAO coating sample basic SEM image (left) and Phosphorous EDS mapping overlay (right)

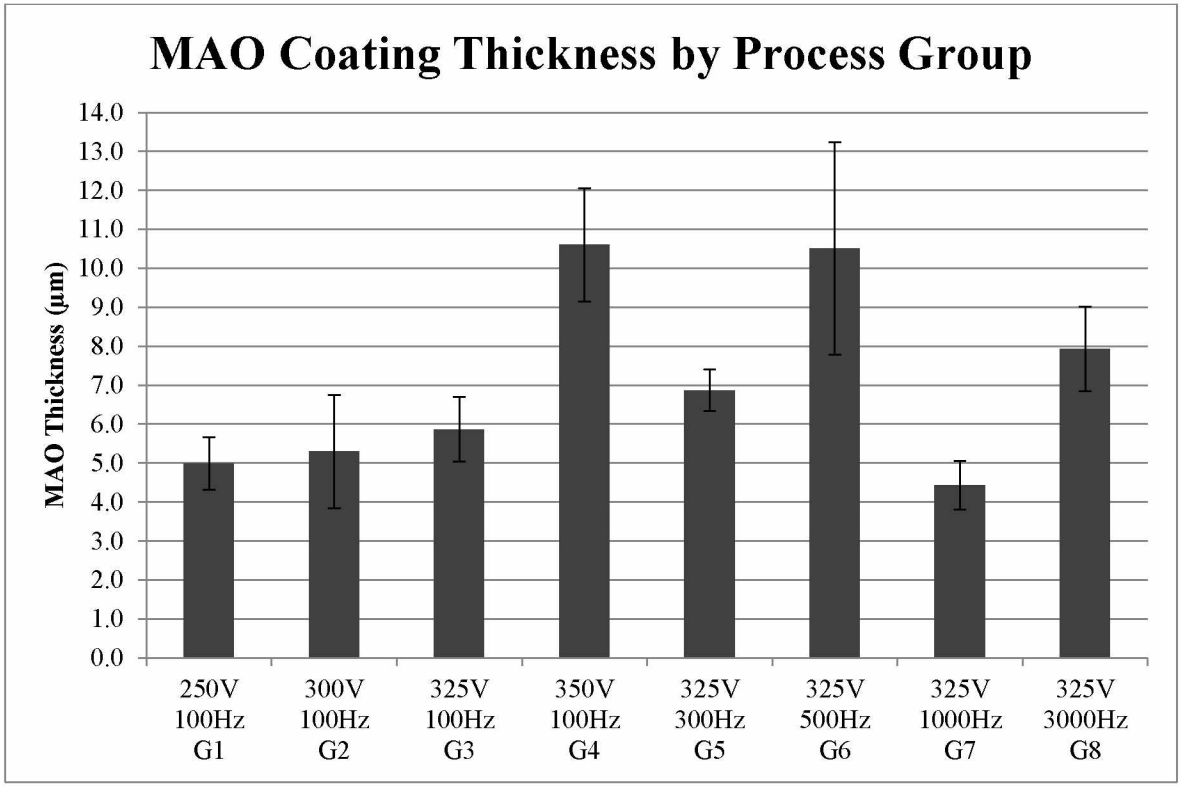

Figure 2.5: MAO coating thickness as measured using EDS mapping

MAO coating thickness increased with voltage for the first four processing groups, with maximum thickness seen at 350V and 100Hz. Coating thickness is also seen to increase with frequency up to a maximum at 500Hz then drop at 1000Hz followed by an increase again at 3000Hz. The minimum thickness was found at 325V 1000Hz (4.4µm) and a maximum at 350V 100Hz (10.6µm). This gives a range spanning all process variations of 6.2µm.

2.3.2 Electrochemical Impedance Spectroscopy / Equivalent Circuits

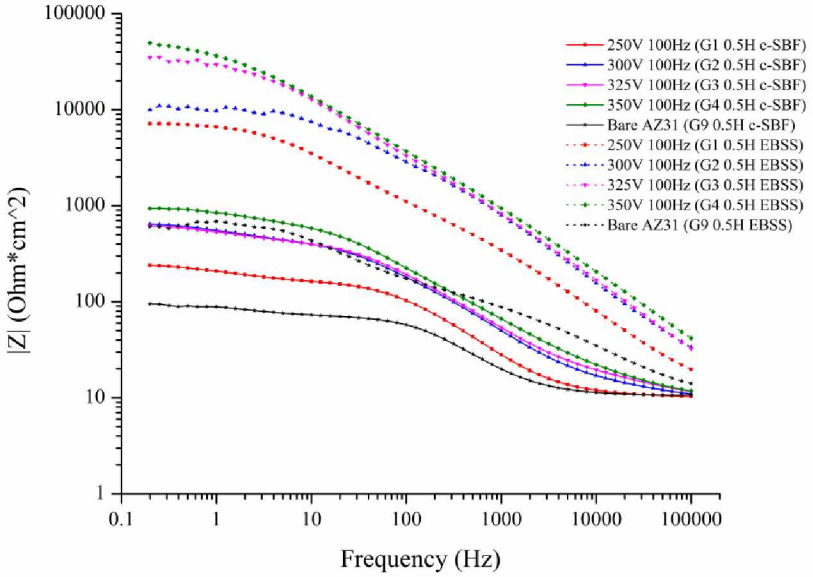

Figure 2.6: EIS Bode plot of 0.5H immersion samples for groups of increasing voltage

The curves increase in impedance in line with the trend observed in sample thickness. The lowest impedance group for either solution is G1 (smallest thickness), while the largest impedance values are seen for G4 (largest thickness).

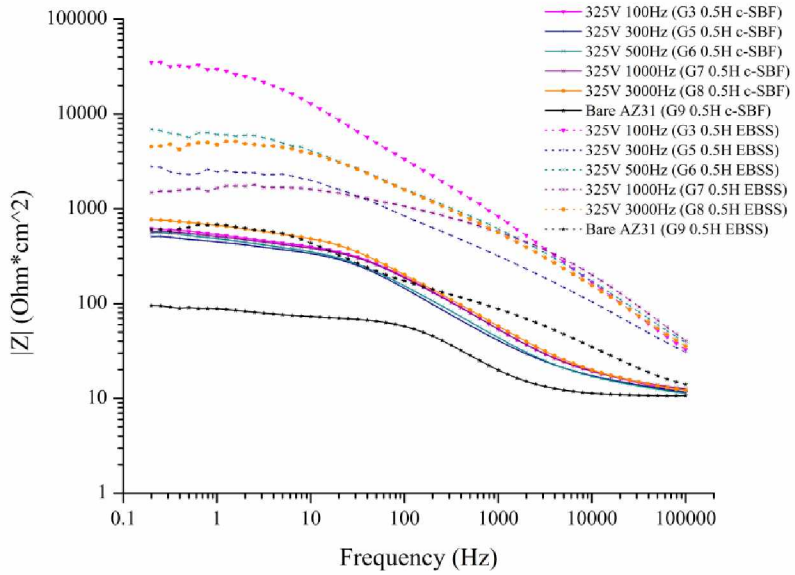

Figure 2.7: EIS Bode plot of 0.5H immersion samples for groups of increasing frequency

In both bode plots above, the lowest impedance at all frequencies for either solution, is seen for the bare AZ31 substrate. EBSS samples show a drastic increase in impedance over the c-SBF groups at 0.5H immersion.

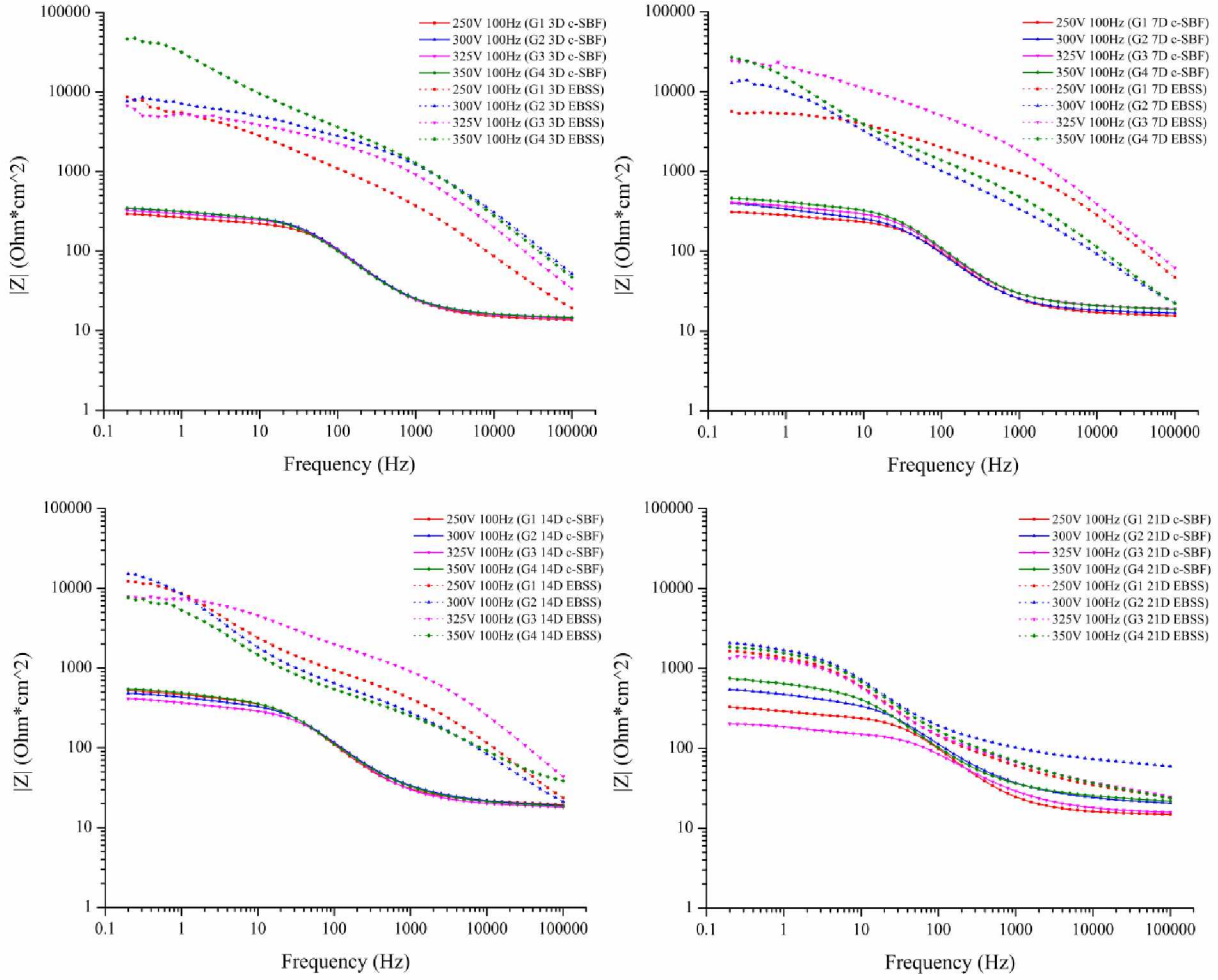

Figure 2.8: EIS Bode plots at increasing immersion time for groups of increasing voltage

Samples immersed in c-SBF remain at similar impedance levels throughout the first 14 days immersion. The EBSS samples, meanwhile, start at a very high impedance and gradually decrease until almost meeting the c-SBF curves at 21 days immersion.

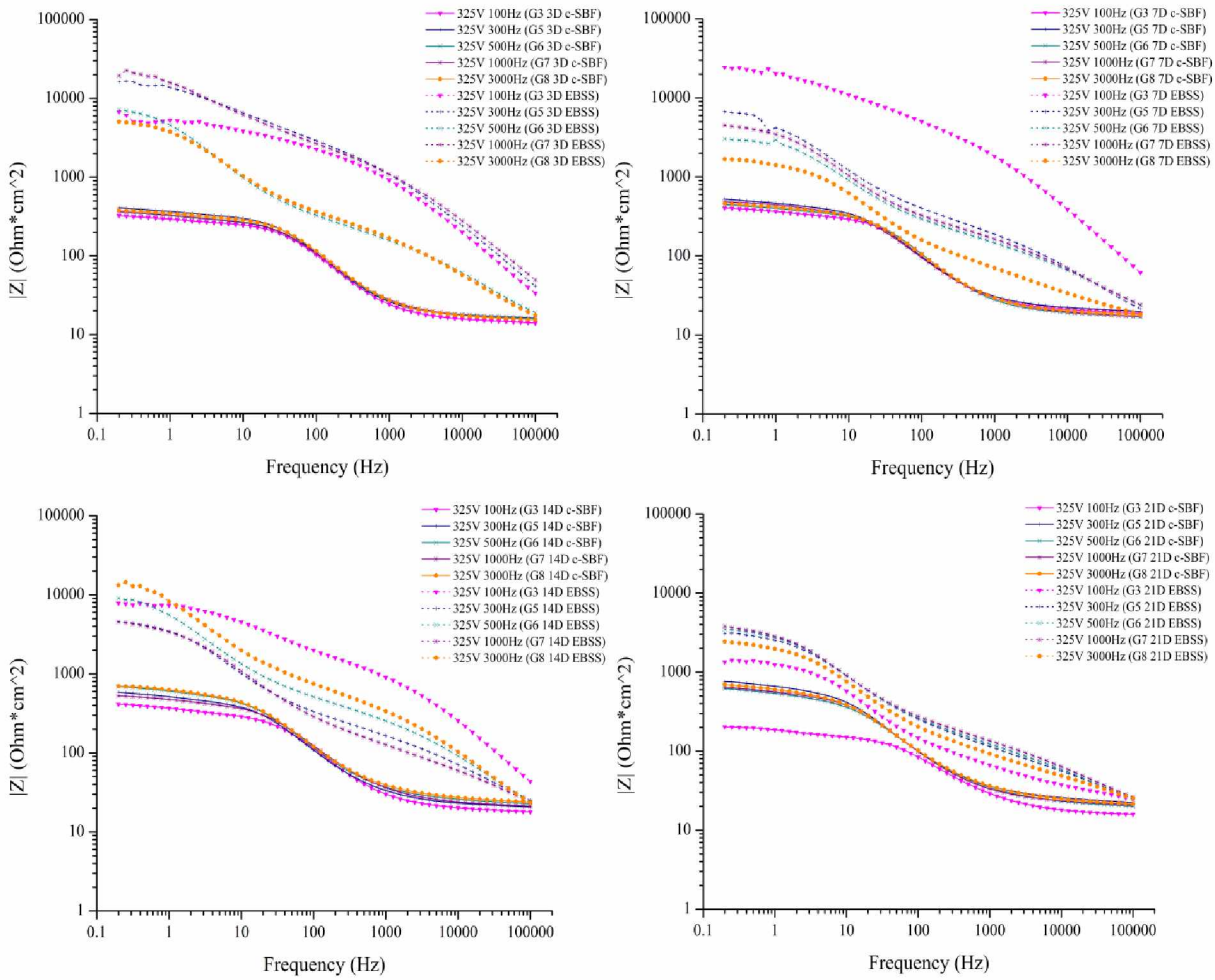

Figure 2.9: EIS Bode plots at increasing immersion time for groups of increasing frequency

A similar progression is shown for the groups of process frequency vs. immersion time. EBSS groups initially have very high impedance relative to c-SBF groups and decrease to more closely match the c-SBF curves at 21 days.

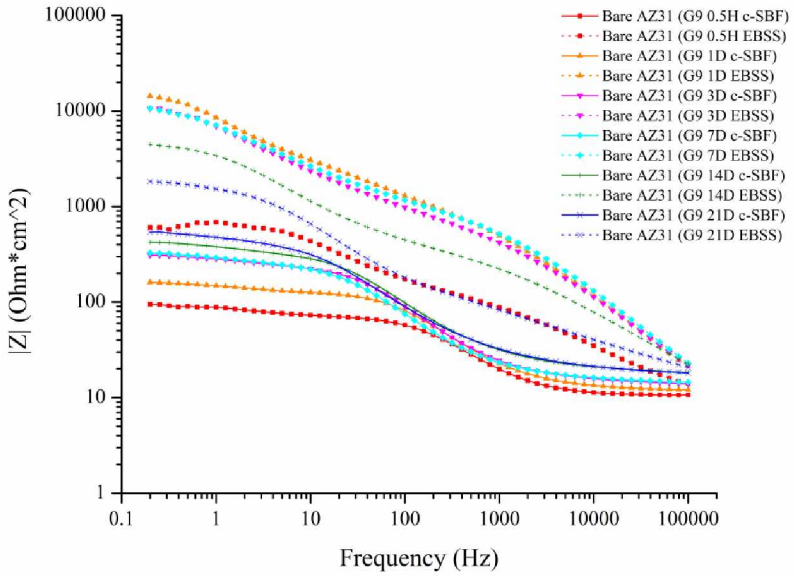

Figure 2.10: Bode plot of AZ31 substrate corrosion progression in EBSS and c-SBF

The uncoated substrate shows a gradual rise in the c-SBF impedance curve with immersion time. Conversely, the impedance curve for the EBSS immersion shows a gradual drop from 1 day and onward. All EBSS curves demonstrate higher impedance values as compared to the c-SBF samples. The barrier layer resistance, R_b, was found to be the dominant resistance in the equivalent circuit fit to the EIS data. R_b values derived from bode plots above are shown in Tables 2.2 and 2.3 below for c-SBF and EBSS.

Table 2.2: R_b values in c-SBF determined by EIS equivalent circuit fit

	c-SBF Immersion Rb (Ω/cm^2)					
Group	**0.5H**	**1D**	**3D**	**7D**	**14D**	**21D**
250V 100Hz (G1)	338	333	288	308	529	334
300V 100Hz (G2)	662	444	339	476	474	540
325V 100Hz (G3)	553	317	312	408	423	201
350V 100Hz (G4)	923	462	347	466	539	690
325V 300Hz (G5)	464	396	397	518	575	743
325V 500Hz (G6)	514	478	357	435	686	560
325V 1000Hz (G7)	531	468	348	473	520	627
325V 3000Hz (G8)	727	280	368	445	696	644
Bare AZ31	132	155	309	324	415	483

Table 2.3: R_b values in EBSS determined by EIS equivalent circuit fit

	EBSS Immersion Rb (Ω/cm^2)					
Group	**0.5H**	**1D**	**3D**	**7D**	**14D**	**21D**
250V 100Hz (G1)	6274	31200	7133	4656	13950	1655
300V 100Hz (G2)	6581	16100	6510	15320	19280	2021
325V 100Hz (G3)	32070	11750	3840	26870	6994	1424
350V 100Hz (G4)	51370	54350	61130	36680	8091	1877
325V 300Hz (G5)	1827	20810	15940	6995	5023	3441
325V 500Hz (G6)	5282	8056	8641	3265	11180	3841
325V 1000Hz (G7)	1663	18970	23050	4721	5104	4111
325V 3000Hz (G8)	5503	42170	5404	1713	16560	2576
Bare AZ31	474	23020	14180	13970	4422	1851

Comparing this value provides a good estimate of the relative corrosion resistance between samples at the various immersion timepoints. EBSS samples showed a much higher R_b than c-SBF samples which is reflective of the higher impedances observed on the EIS bode plots. R_b values for EBSS samples generally start very high and decrease with a large drop in resistance seen between 14 and 21 days. c-SBF samples hold consistent values throughout the immersion period with a gradual rise seen for the bare AZ31 samples. These values are plotted graphically below:

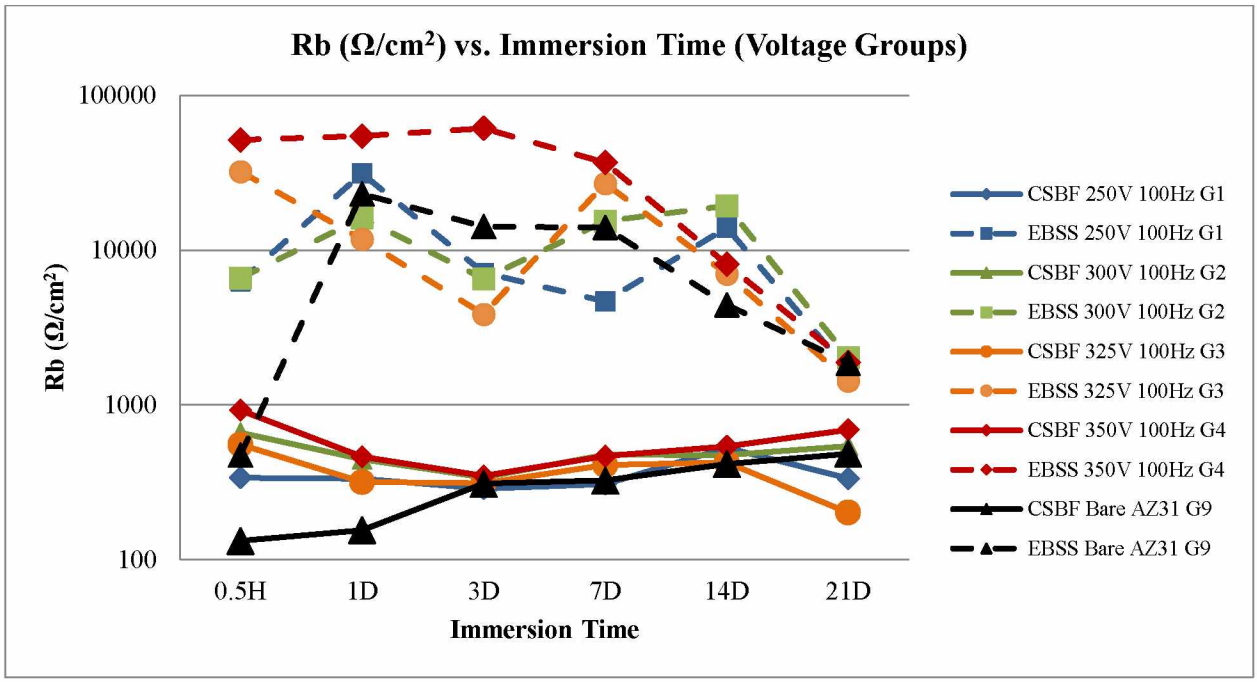

Figure 2.11: R_b values plotted vs. immersion time for groups of increasing voltage

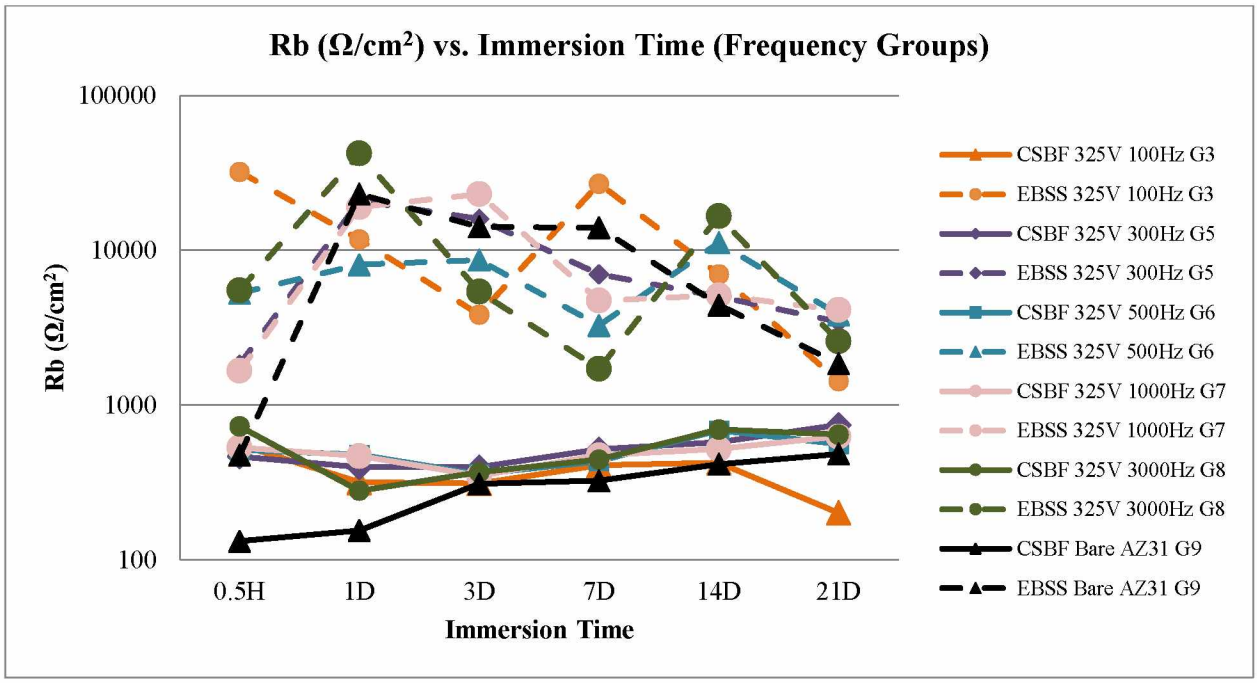

Figure 2.12: R_b values plotted vs. immersion time for groups of increasing frequency

The bare AZ31 substrate showed the lowest initial R_b values for both solutions as compared with all groups. This shows the improved corrosion resistance provided by the MAO coating regardless of process parameters. As all groups approach 21 days, the c-SBF and EBSS R_b values are trending toward

each other. The EBSS curves fall as the MAO layer is finally broken down at a higher rate, while the c-SBF curves rise due to formation of protective corrosion products on the surface.

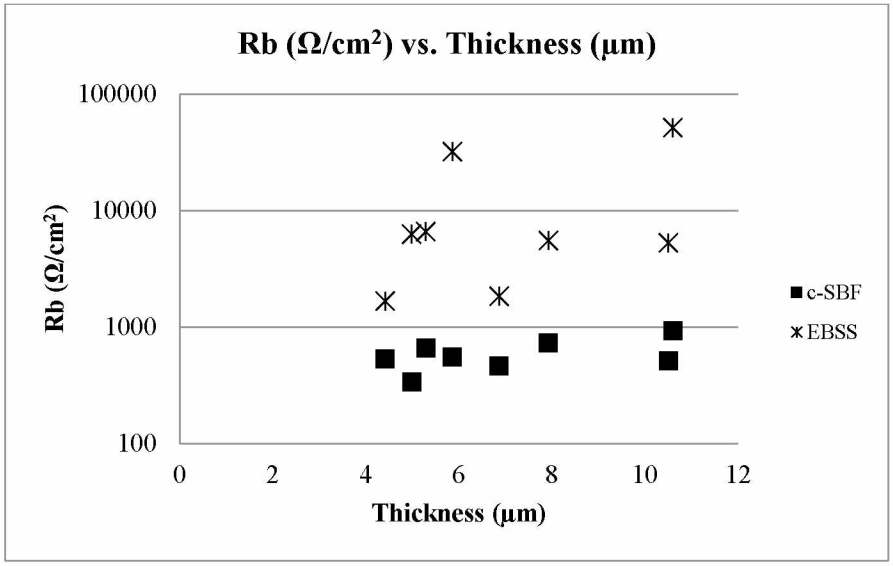

Figure 2.13: MAO coating thickness vs. barrier resistance at 0.5H immersion

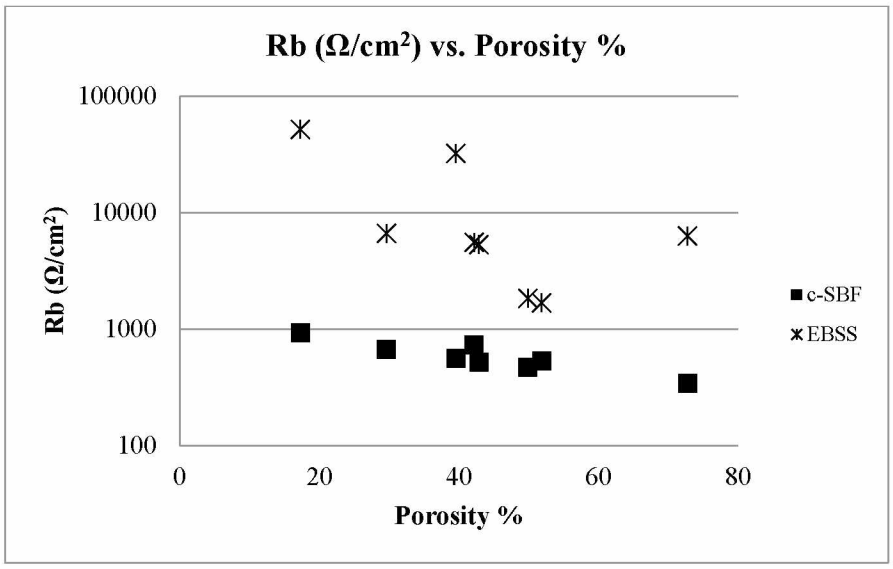

Figure 2.14: MAO porosity vs. barrier resistance at 0.5H immersion

Barrier resistance tends to increase with increased coating thickness and decrease for increased porosity in both c-SBF and EBSS. This is in line with the expectation that a thicker, less porous, coating provides a larger impedance in the equivalent circuit and higher resistance to corrosion.

2.3.3 Potentiodynamic Polarization

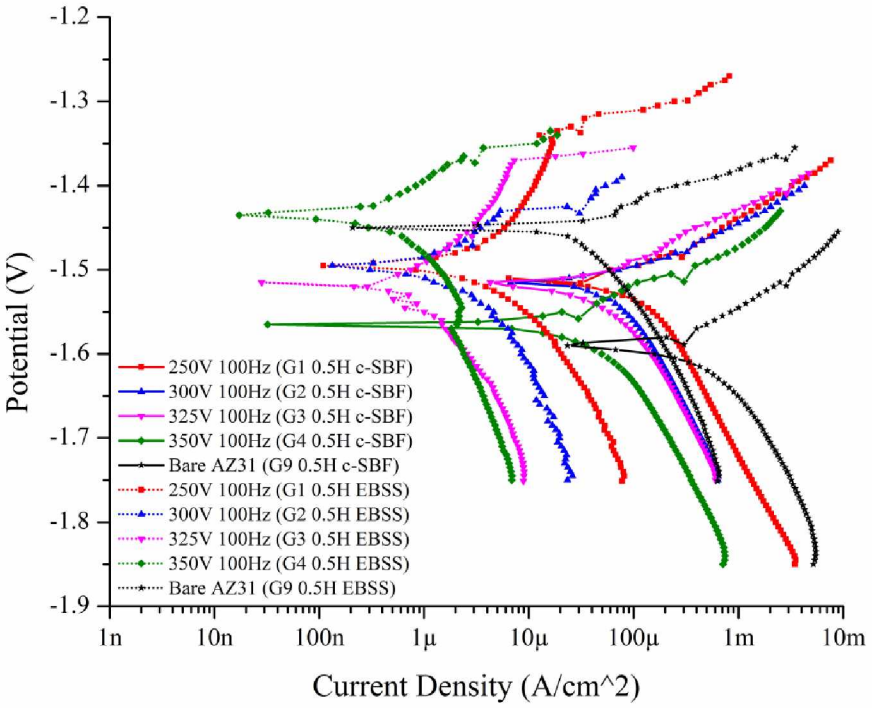

Figure 2.15: Potentiodynamic scans of 0.5H immersion samples in c-SBF and EBSS for groups of increasing voltage

At 0.5H immersion the 350V group shows the smallest current density, located left of the other voltage groups in both solutions. The bare AZ31 substrate is positioned furthest right (largest current density) for both corrosion solutions indicating a larger rate of corrosion than the MAO coated samples. With regards to potential, the uncoated material shows the highest negative potential in the c-SBF with the coated samples positioned in the more passive direction (less negative).

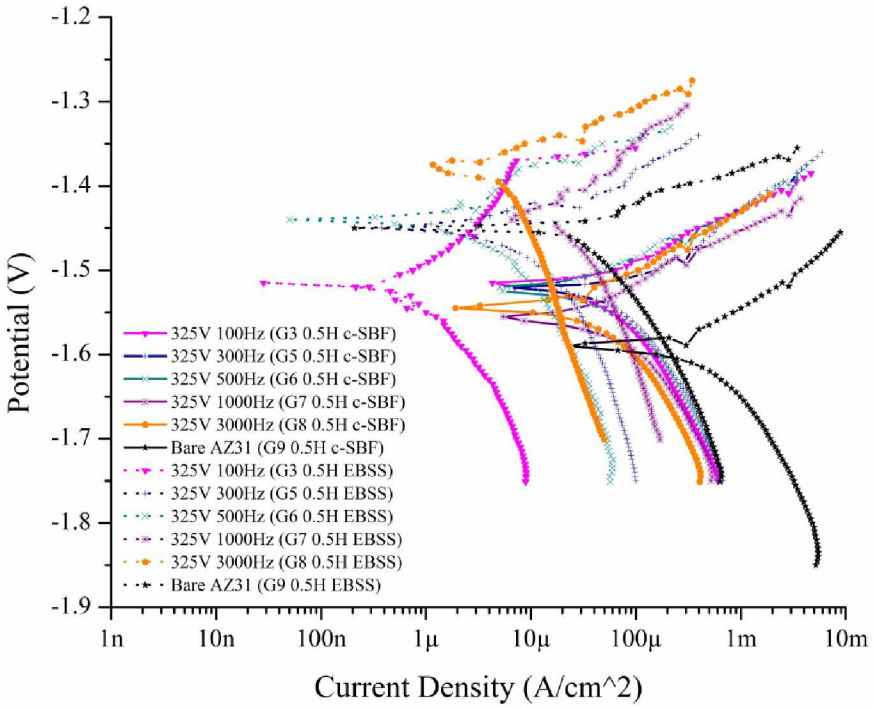

Figure 2.16: Potentiodynamic scans of 0.5H immersion samples in c-SBF and EBSS for groups of increasing process frequency

Groups of increasing frequency, for 0.5H immersion in c-SBF, are located very close to each other on the tafel plot in terms of potential and current density suggesting similar corrosion performance at this time point. The bare substrate, again, shows a higher current density than the coated samples in both EBSS and c-SBF. For EBSS samples, the groups are more dispersed on the tafel plot with the lowest frequency showing the most negative potential and lowest current density. In the EBSS groups the higher frequency groups show increasing passivity as well as increasing current density.

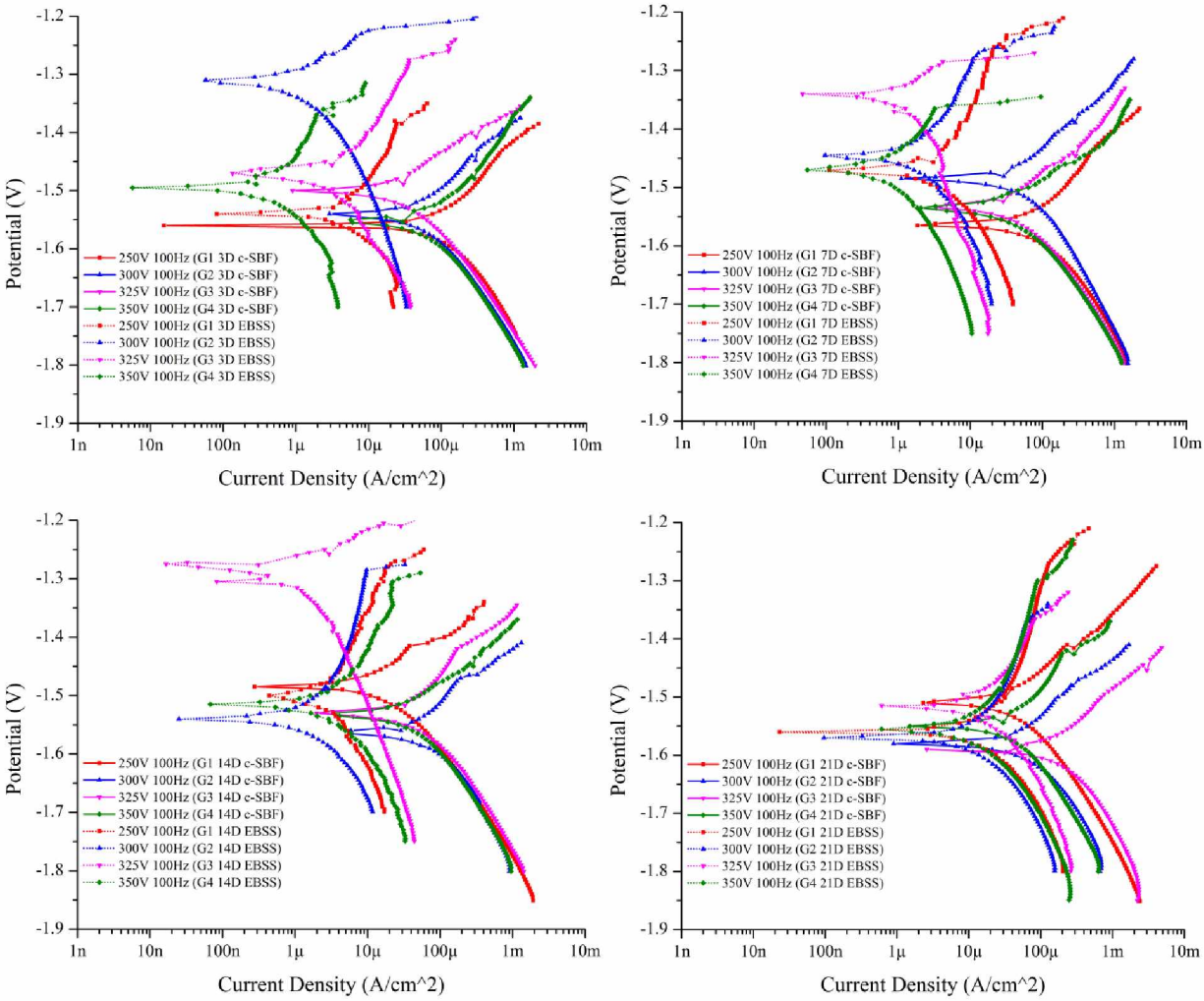

Figure 2.17: Potentiodynamic scans at increasing immersion time for groups of increasing voltage

For immersion times up to 14 days the EBSS and c-SBF show clear separation in current density with the EBSS being lower. At 21 days immersion the EBSS samples approach the same values of current density as those in c-SBF.

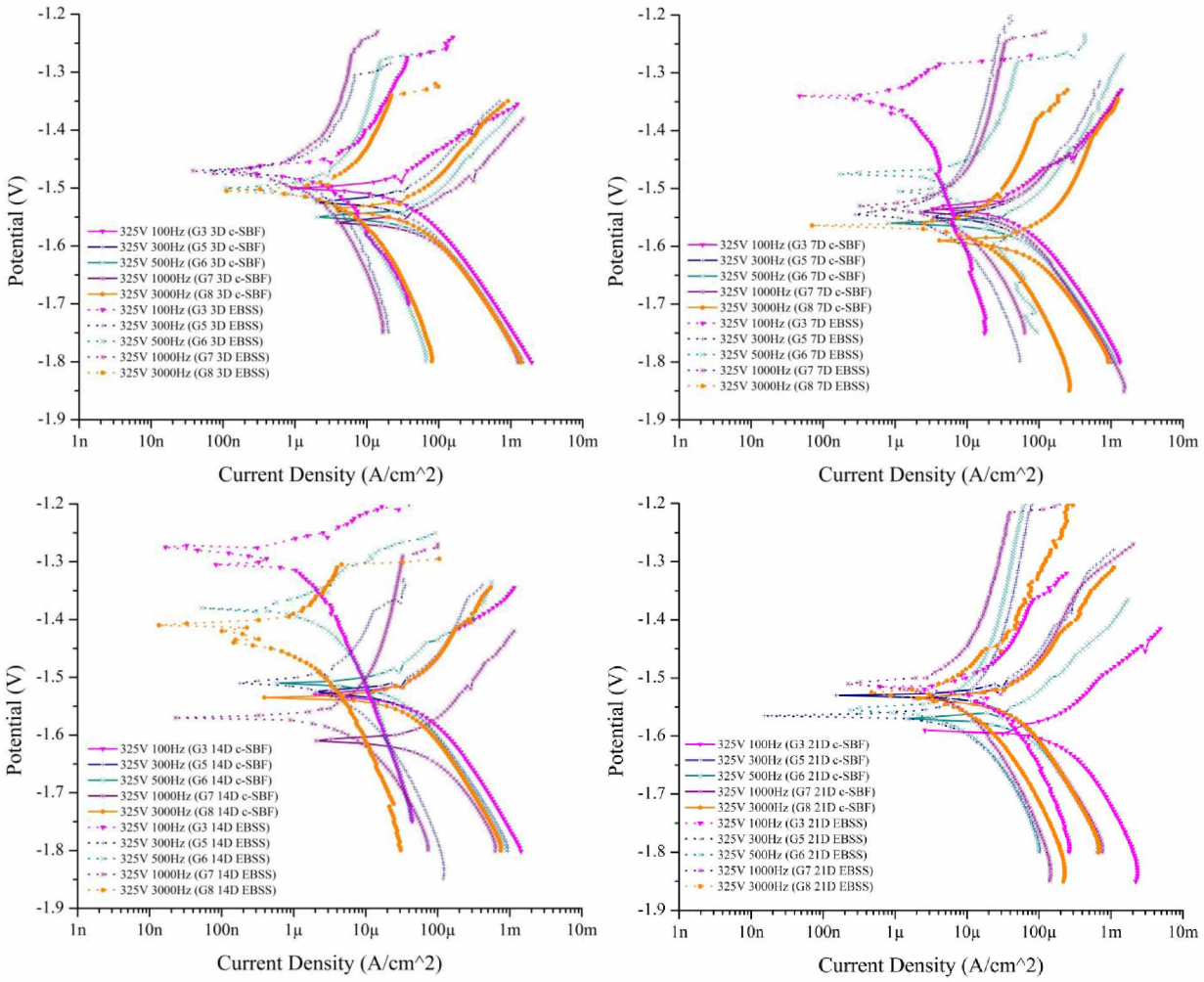

Figure 2.18: Potentiodynamic scans at increasing immersion time for groups of increasing frequency

The plots of frequency groups shows a similar trend to that observed for the voltage groups comparing EBSS and c-SBF over time. The EBSS groups start at a much lower current density than the c-SBF samples for short immersion periods and approach c-SBF values at 21 days.

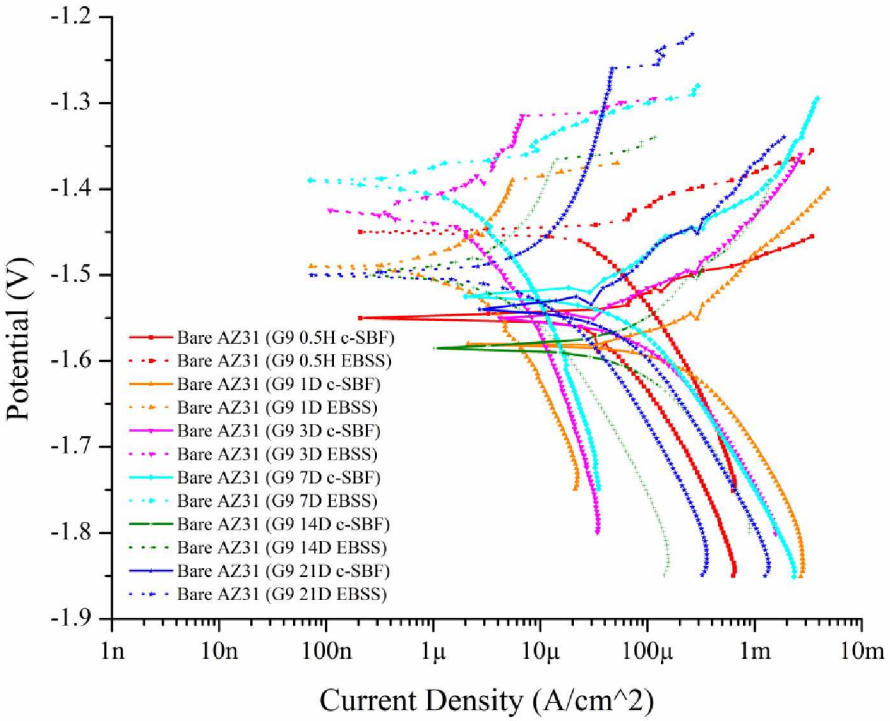

Figure 2.19: Bare AZ31 substrate corrosion progression in EBSS and c-SBF

The bare AZ31 substrate curve shows a shift left (lower current density) after the initial timepoint for both EBSS and c-SBF. The c-SBF plots show a gradual shift to lower current density and slightly less negative potential over the course of 21 days immersion. The EBSS plot shows a shift toward lower current density initially followed by eventual shift toward higher current density and more active performance at 21 days. These trends are consistent with the shifts in impedance seen on bode EIS plots. The EBSS curves are generally located to the left (lower current density) and higher (less negative potential) when compared to the c-SBF groups. This suggests that the effect of an initial reduction in corrosion rate for the EBSS cascades through all time points resulting in a slower overall corrosion progression. I_{corr} values were extracted via tafel fit of the curves above and are presented below:

Table 2.4: I_{corr} values for c-SBF corrosion samples determined by tafel curve fit

	c-SBF Immersion Icorr (μA/cm²)					
Group	**0.5H**	**1D**	**3D**	**7D**	**14D**	**21D**
250V 100Hz (G1)	121.0	42.3	102.0	118.0	38.0	54.5
300V 100Hz (G2)	82.2	79.5	86.8	63.6	101.0	84.9
325V 100Hz (G3)	56.5	146.0	37.8	55.4	87.1	214.0
350V 100Hz (G4)	35.8	84.6	102.0	37.6	49.2	86.6
325V 300Hz (G5)	110.0	96.5	55.1	72.1	62.1	54.5
325V 500Hz (G6)	52.5	72.8	75.8	79.3	32.7	70.8
325V 1000Hz (G7)	65.4	87.2	88.2	60.5	82.5	69.2
325V 3000Hz (G8)	47.7	85.9	67.7	184.0	61.2	65.2
Bare AZ31	528.0	240.0	93.3	63.7	87.5	55.6

Table 2.5: I_{corr} values for EBSS corrosion samples determined by tafel curve fit

	EBSS Immersion Icorr (μA/cm²)					
Group	**0.5H**	**1D**	**3D**	**7D**	**14D**	**21D**
250V 100Hz (G1)	13.4	0.8	53.2	9.1	57.7	59.4
300V 100Hz (G2)	8.3	9.8	3.2	13.4	6.4	22.0
325V 100Hz (G3)	1.7	8.7	3.5	2.2	3.4	72.1
350V 100Hz (G4)	1.1	1.3	1.2	2.2	9.7	35.9
325V 300Hz (G5)	8.0	1.7	8.5	15.9	15.1	23.2
325V 500Hz (G6)	6.1	75.6	12.8	14.6	4.4	18.9
325V 1000Hz (G7)	51.6	2.2	3.4	21.5	15.3	13.9
325V 3000Hz (G8)	6.2	2.9	13.6	39.2	1.0	14.5
Bare AZ31	36.1	4.7	4.7	6.0	10.8	18.4

I_{corr} values extracted demonstrate the gap in corrosion rates between the EBSS and c-SBF. The bare substrate showed a drop in I_{corr} following the 0.5H timepoint which is due to the oxidation of the surface and generation of corrosion products hindering further corrosion. I_{corr} values at 0.5H for both c-SBF and EBSS samples decrease with increasing process voltage (at 100Hz) consistent with the increase in coating thickness. This trend does not hold beyond the initial timepoint with I_{corr} values becoming more erratic and falling in the range of 35-150μA/cm^2.

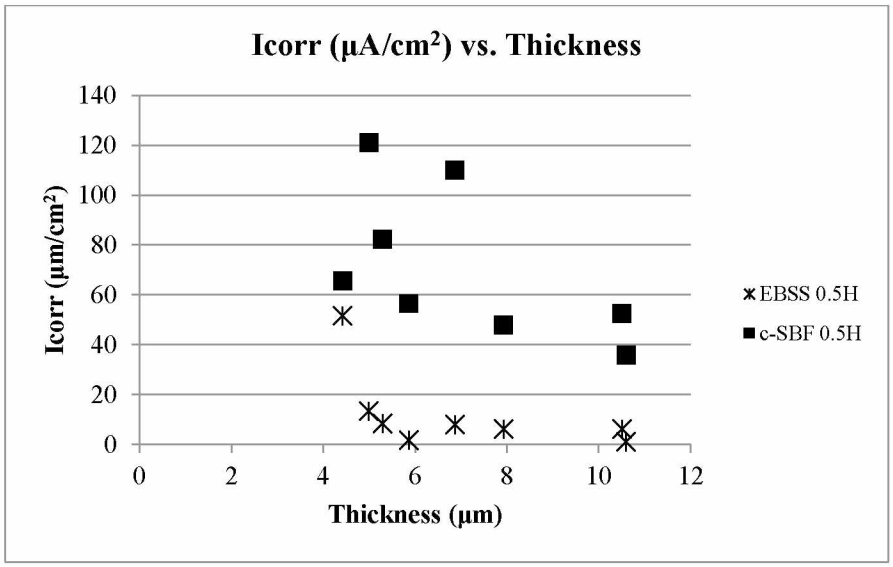

Figure 2.20: MAO coating thickness vs. current density at 0.5H immersion

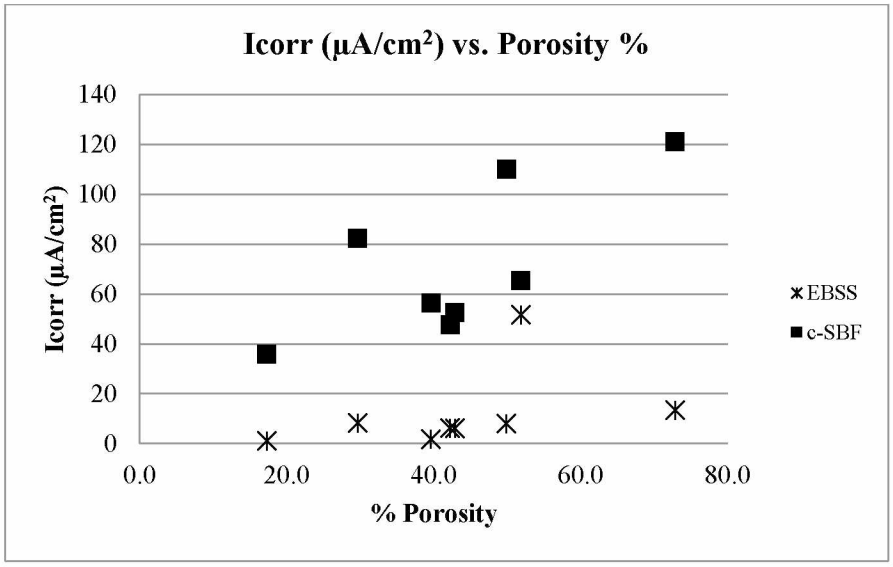

Figure 2.21: MAO coating porosity vs. current density at 0.5H immersion

Current density was seen to decrease with increased sample thickness and decrease with increased porosity in both c-SBF and EBSS. This is in line with barrier resistance values seen above and the understanding that a thicker, less porous coating, provides for a lower corrosion rate at the initial timepoint.

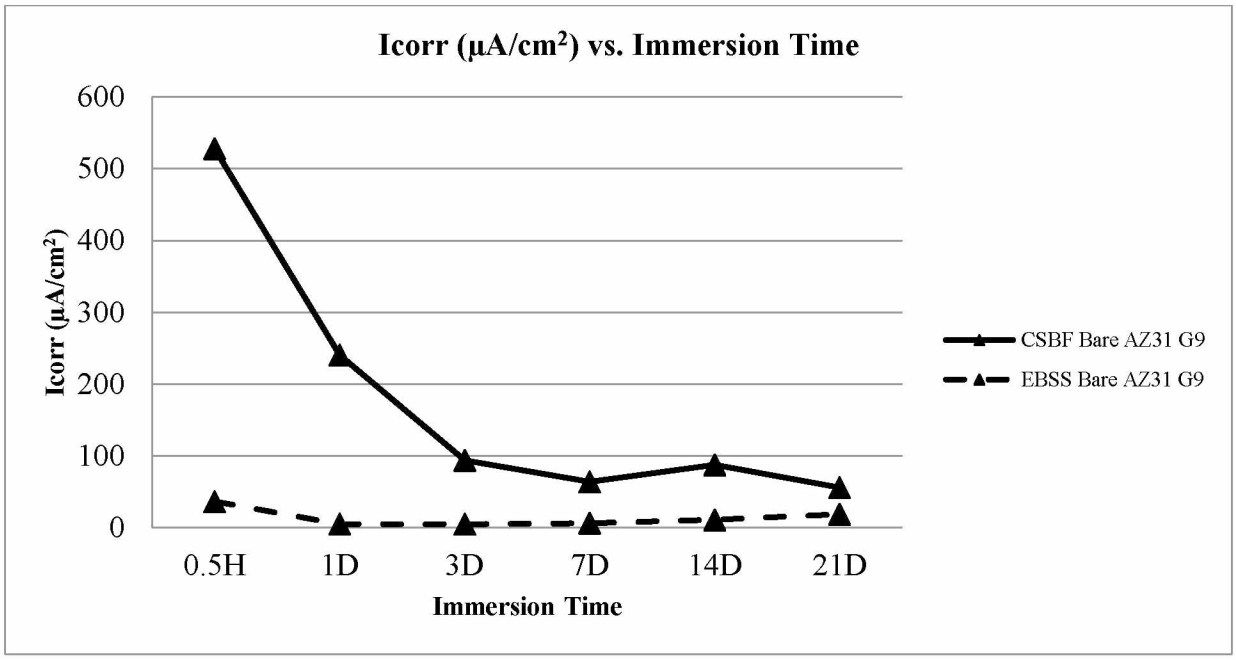

Figure 2.22: I_{corr} vs. immersion time for bare AZ31 substrate

The plot of the uncoated substrate shows a significant initial corrosion rate followed by a leveling off after 3 days immersion. Although current density values level off for the uncoated material, they remain among the highest of any sample tested.

2.3.4 Corroded Surface Morphology

2.3.4.1 Macroscopic Images

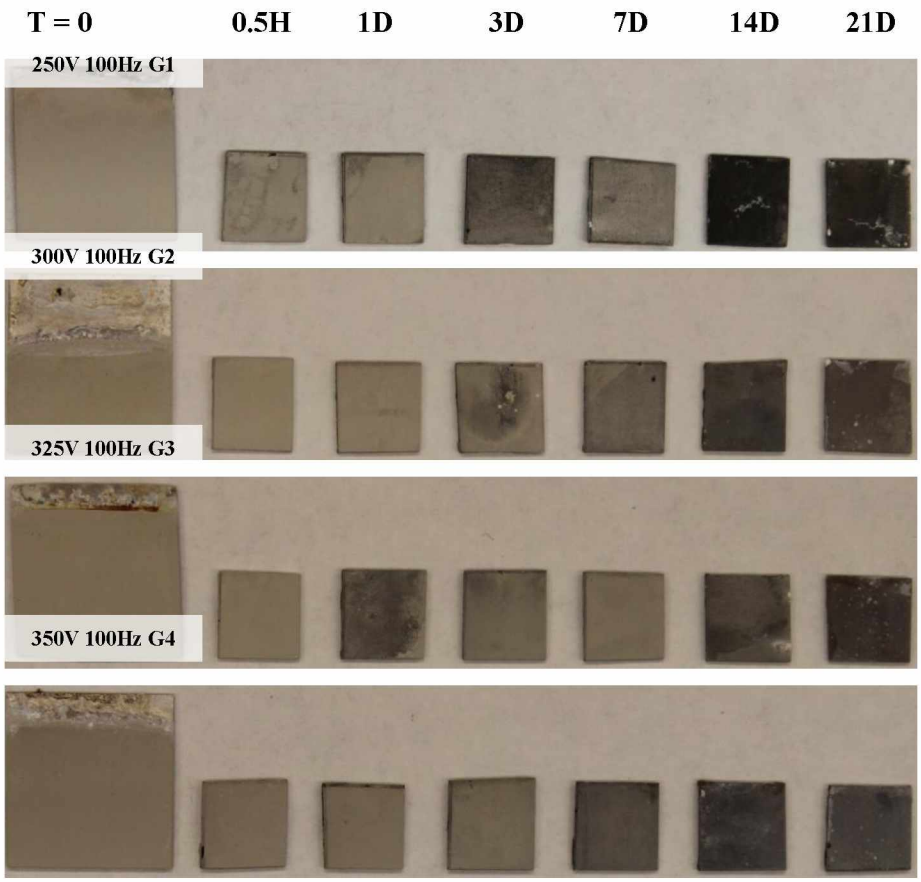

Figure 2.23: EBSS macroscopic corrosion progression for groups of increasing voltage

The MAO surface is visibly darkened as soon as 1 day immersion for group 3 in the EBSS, while some samples show a light gray surface out to 7 days. By 14 days immersion all samples have a significantly darker appearance and at 21 days white corrosion products are visible.

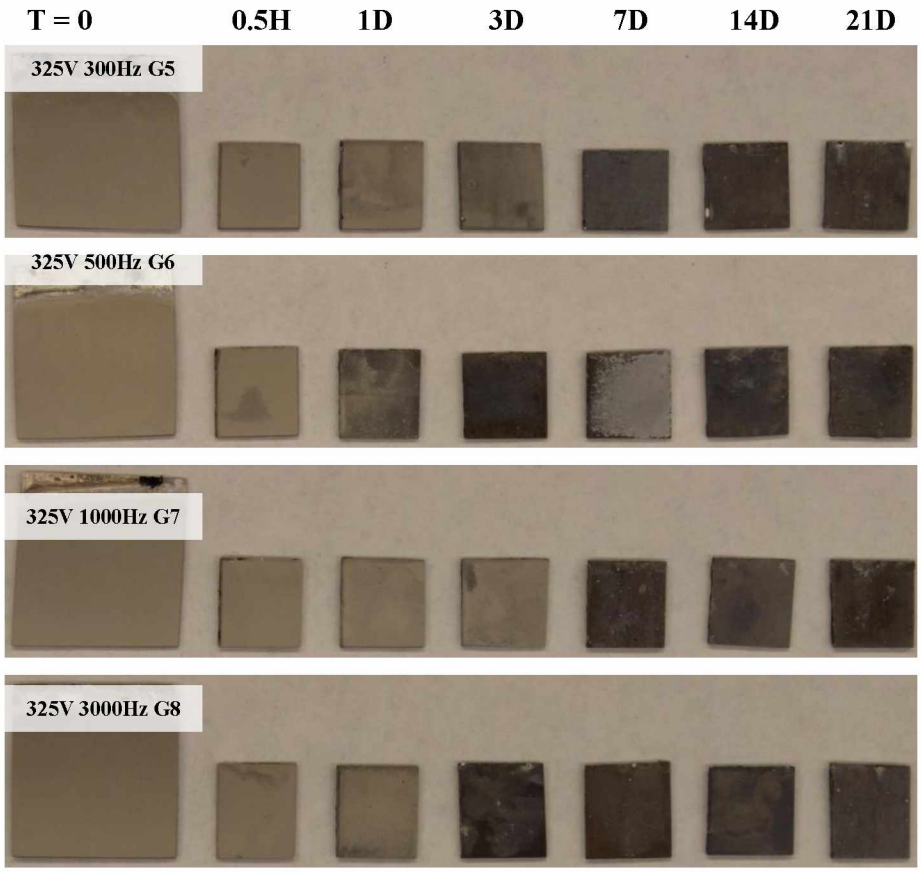

Figure 2.24: EBSS macroscopic corrosion progression for groups of increasing frequency

Similar overall trends are seen in the macroscopic pictures of the increasing frequency groups in EBSS (above). At 1 day immersion, most samples retain light gray MAO appearance except groups 3 and 6. Most groups show dark gray surface at 7 days immersion with large pits developing at 21 days immersion.

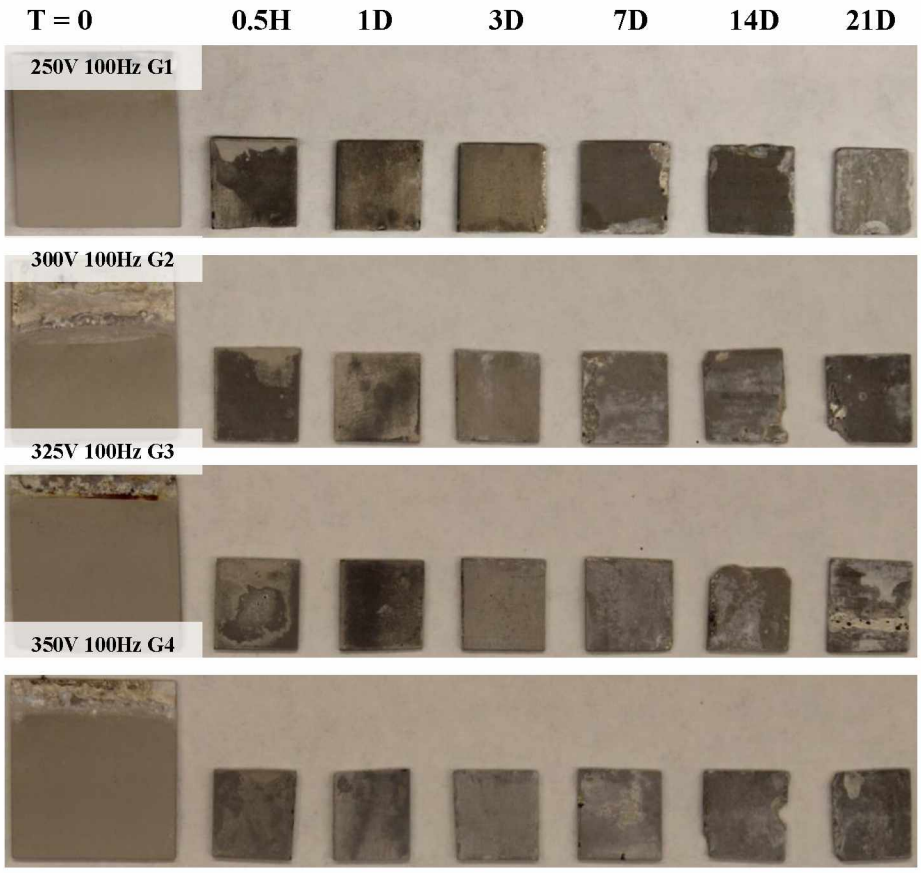

Figure 2.25: c-SBF macroscopic corrosion progression for groups of increasing voltage

Samples for c-SBF immersion show immediate loss of light gray MAO surface at 0.5H immersion. This demonstrates the quick onset of corrosion in c-SBF as compared to EBSS. Pits are visible on the surface of samples as soon as 1 day immersion. At 7 days immersion sample groups 1-3 show clear edge defects and loss of material. Corrosion progresses for all groups with the most damage observed at 21 days and a white corrosion product surface presence on all groups from 7 days onward.

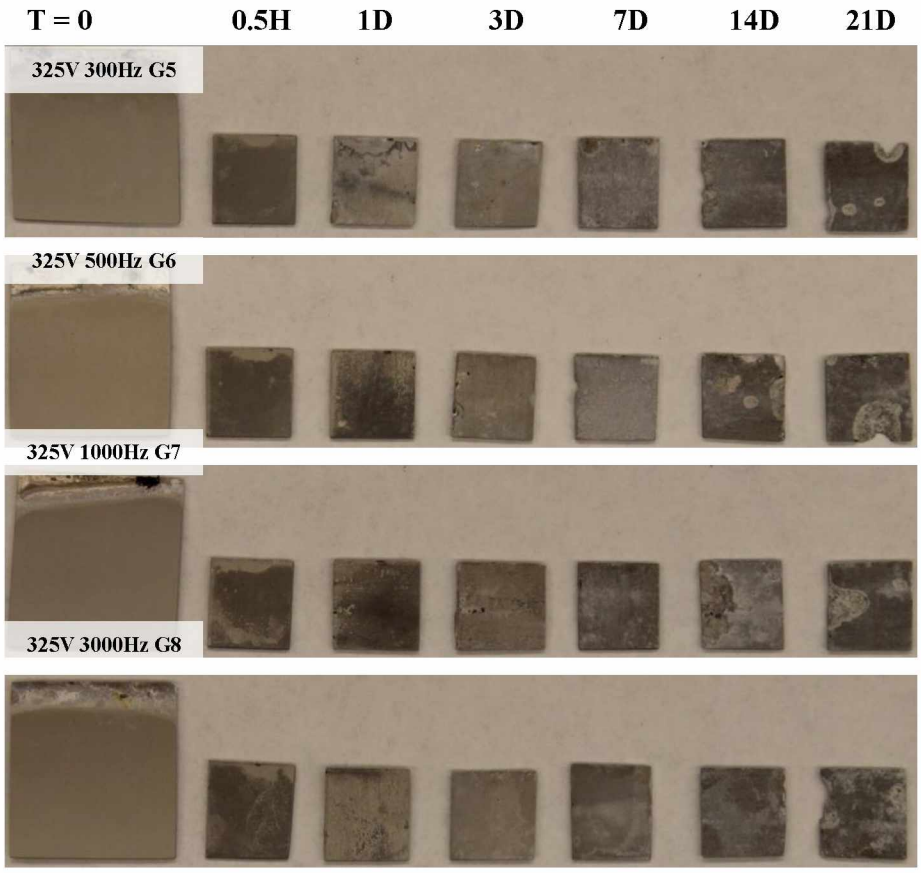

Figure 2.26: c-SBF macroscopic corrosion progression for groups of increasing frequency

Across groups of increasing frequency an immediate loss of the gray MAO surface appearance is shown at 0.5H immersion. Pits are seen developing as soon as 1 day immersion with corrosion progressing out to 21 days. As with the voltage groups, a white corrosion product surface is visible for all samples from 7 days and onward. The bare substrate immersed in EBSS vs. c-SBF is compared below:

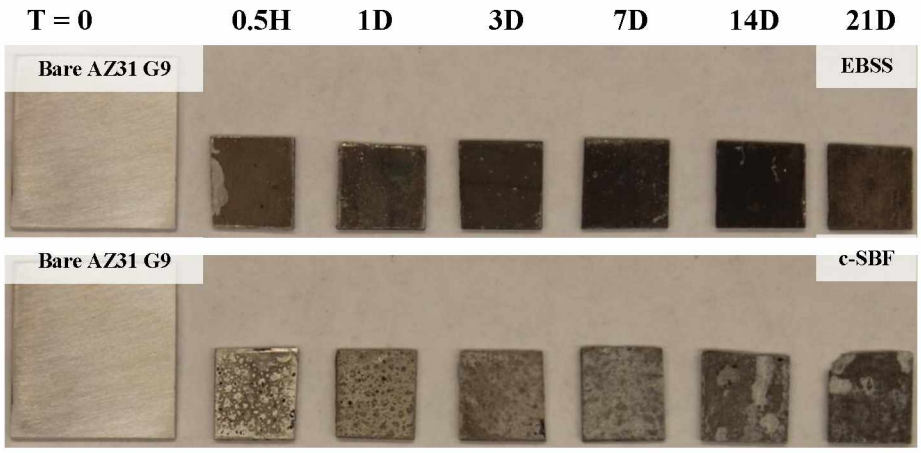

Figure 2.27: Bare AZ31 substrate macroscopic corrosion progression in EBSS and c-SBF

The shiny gray AZ31 surface is immediately replaced within 0.5H immersion for both solution groups. The EBSS surface appears dark gray while the c-SBF solution appears as blotches of silver and gray. A white corrosion product layer and corrosion of the sample edge can be seen from days 3 and onward for the c-SBF group. At 21 days the c-SBF group shows very large pores and material loss while the EBSS group appears darkened but without obvious pitting.

2.3.4.2 Secondary Electron Imaging

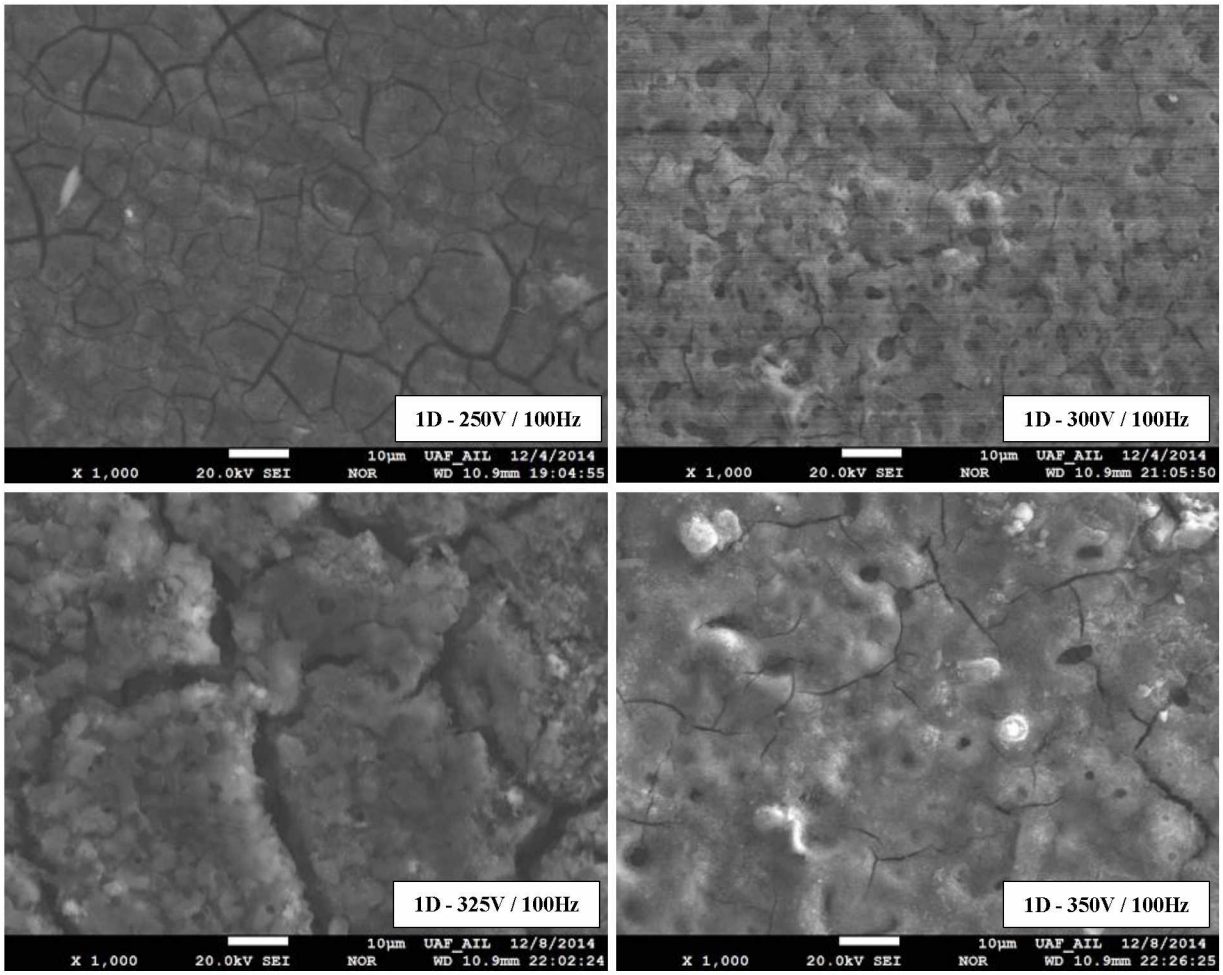

Figure 2.28: c-SBF 1D immersion SEM imaging (1000x) for groups of increasing voltage, Group 1 (top left), Group 2 (top right), Group 3 (bottom left), Group 4 (bottom right)

At 1 day immersion in the c-SBF solution, the porous MAO surfaces for all 100Hz samples show micro-cracks developing. The largest cracks are seen for the 325V group which had previously shown micro-cracks prior to immersion (T=0D). The surface projections have been dissolved for the 250V group leaving a non-porous surface between developing cracks.

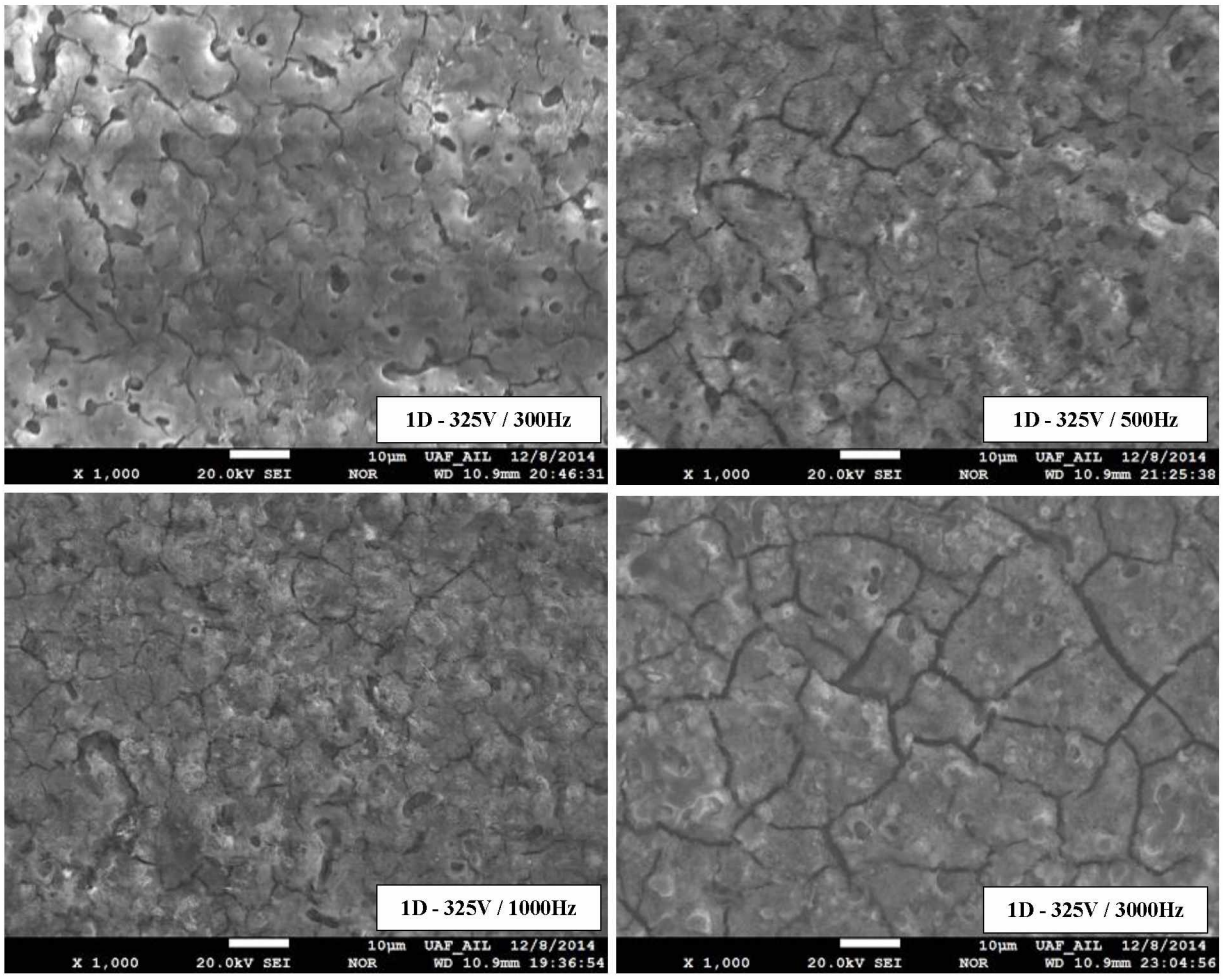

Figure 2.29: c-SBF 1D immersion SEM imaging (1000x) for groups of increasing frequency, Group 5 (top left), Group 6 (top right), Group 7 (bottom left), Group 8 (bottom right)

Process frequency groups ranging from 100Hz t 3000Hz, which showed similar surface appearance to each other prior to immersion, show similar corrosion after 1D with some MAO pores still visible and cracks developing on the surface. The largest cracks are found for the 100Hz group, while the largest cracks for the 300Hz-3000Hz groups fall in the range of 1.0-2.5µm.

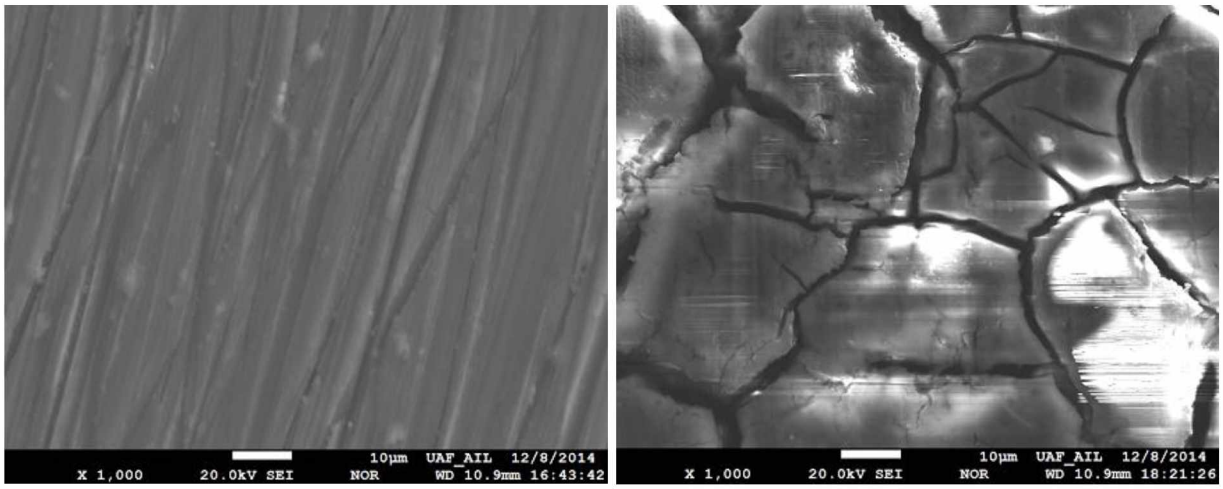

Figure 2.30: Bare AZ31 SEM imaging (1000x) for non-corroded (left), 1D immersion in c-SBF (right)

The bare AZ31 substrate material shows cracking of uncoated surface after 1D c-SBF immersion. This demonstrates the corrosion protection provided by any process variant of the oxidation coating, regardless of thickness or porosity.

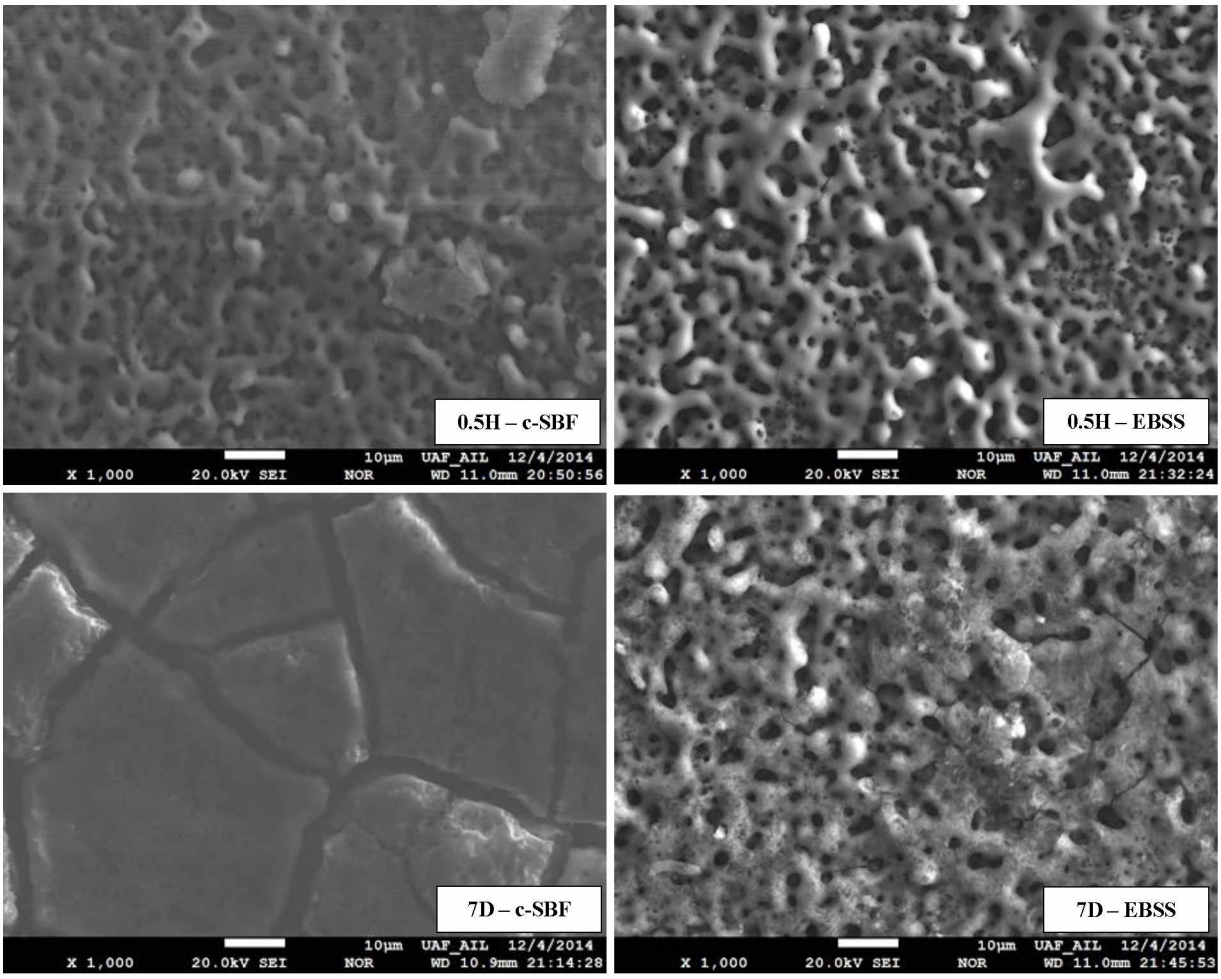

Figure 2.31: Process Group 2 (300V, 100Hz) SEM imaging (1000x) of corrosion progression in c-SBF (left column) vs. EBSS (right column) 0.5H-7D

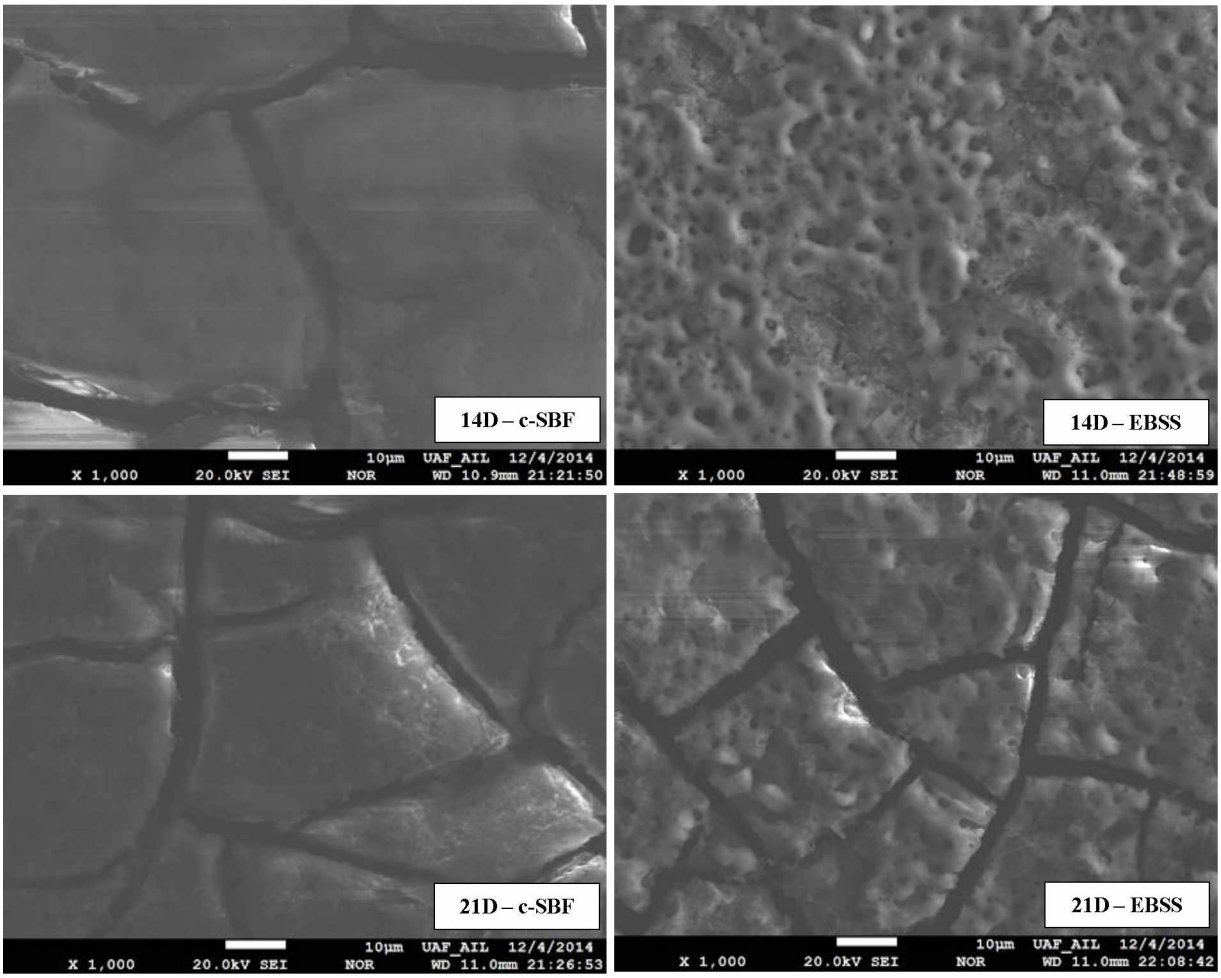

Figure 2.32: Process Group 2 (300V, 100Hz) SEM imaging (1000x) of corrosion progression in c-SBF (left column) vs. EBSS (right column) 14D-21D

A significant reduction in visible corrosion was observed for samples immersed in EBSS when compared to c-SBF across all groups. The corrosion progression for Group 2 (Figures 2.31 and 2.32) shows that, for the low thickness, coating c-SBF causes a rapid loss of the MAO coating and ensuing crack formation prior to 7 days immersion. The EBSS delays this corrosion, showing reduced micro-crack development up to 14 days immersion.

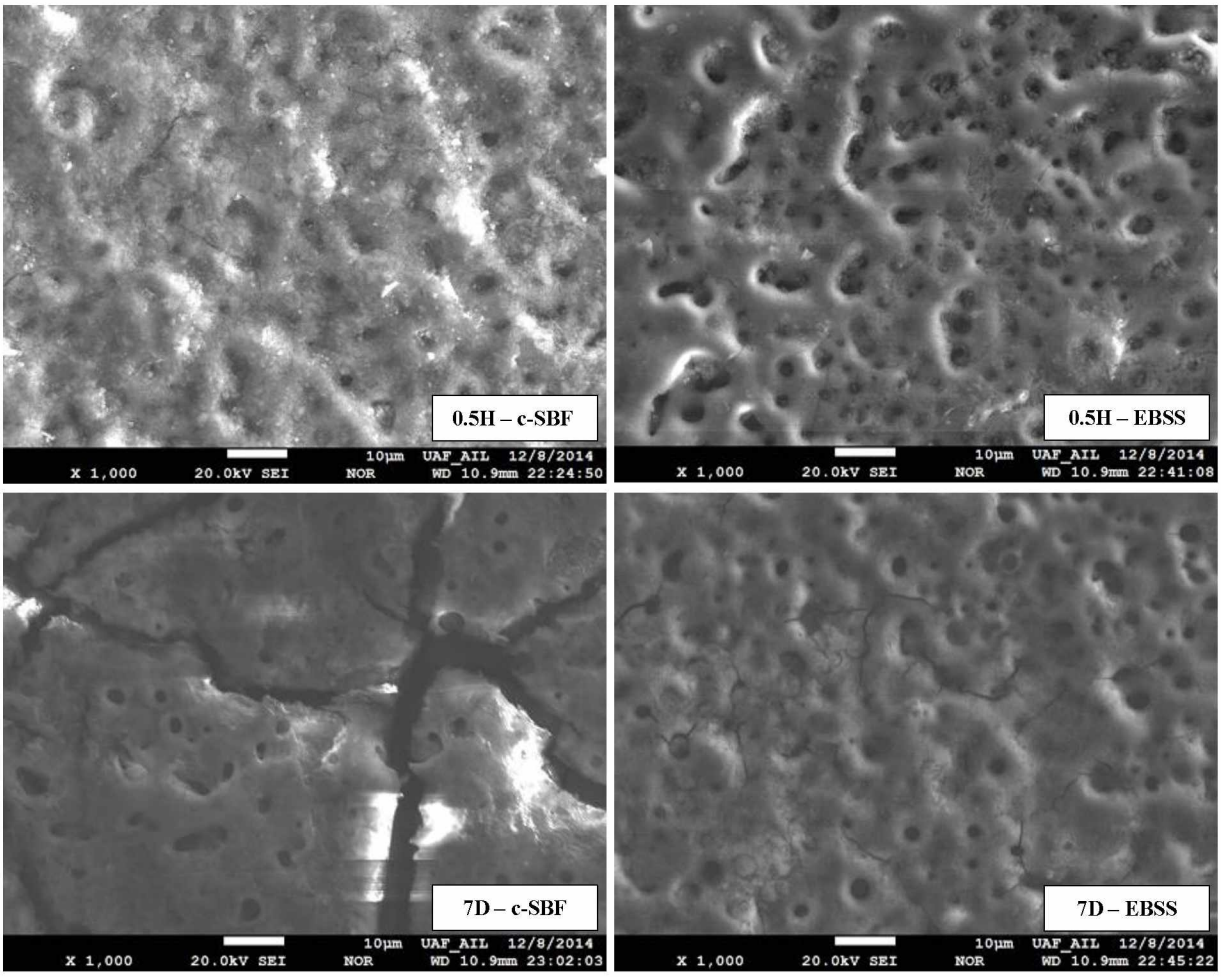

Figure 2.33: Process Group 4 (350V, 100Hz) SEM imaging (1000x) of corrosion progression in c-SBF (left column) vs. EBSS (right column) 0.5H-7D

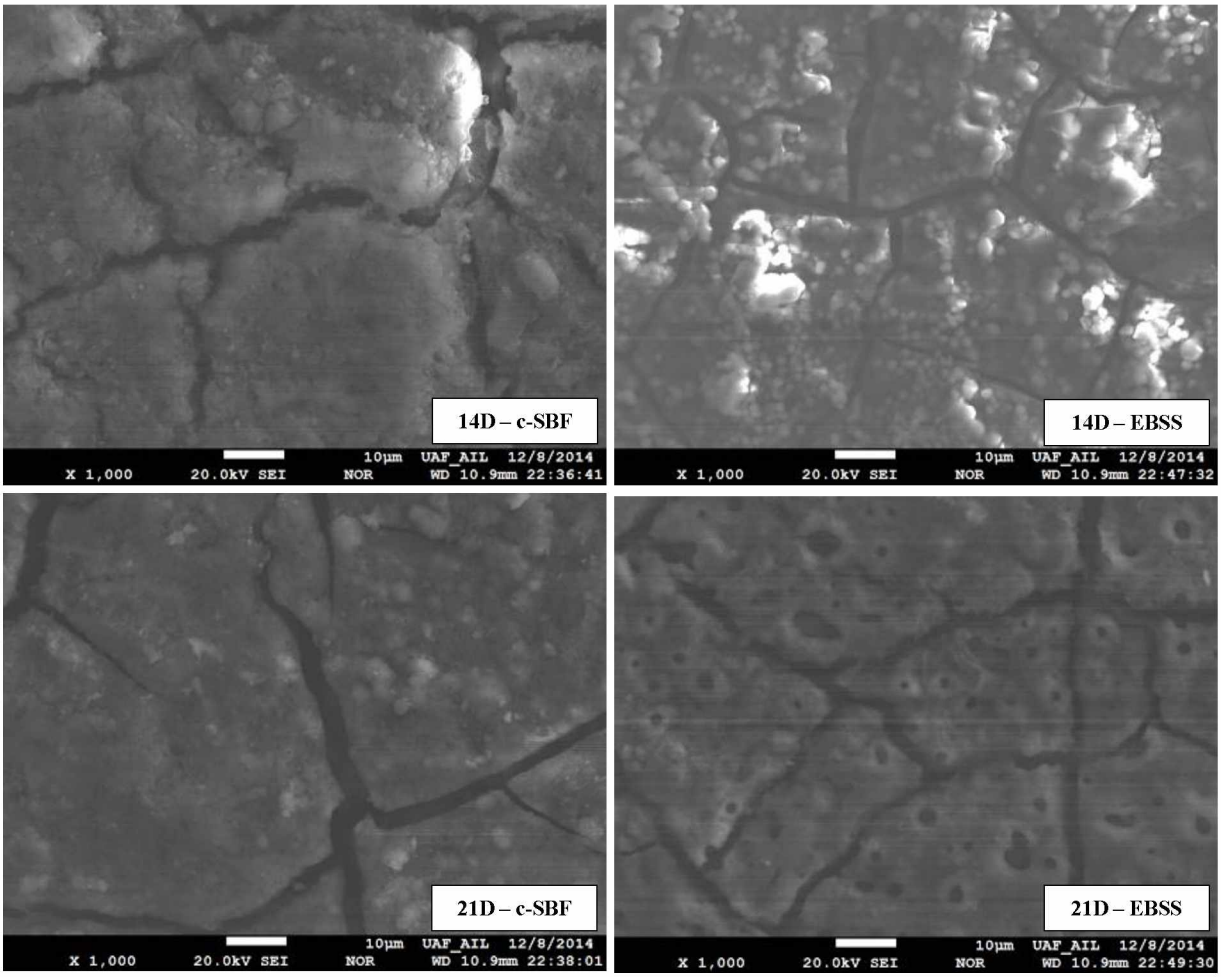

Figure 2.34: Process Group 4 (350V, 100Hz) SEM imaging (1000x) of corrosion progression in c-SBF (left column) vs. EBSS (right column) 14D-21D

In c-SBF immersion, Group 4 (highest thickness) progression, shown in Figures 2.33 and 2.34 shows micro-crack growth occurs rapidly over the first 7 days while the porous MAO surface is dissolved, and no longer visible, by 14D. In contrast, the EBSS shows delayed crack growth up to 7D, with the porous MAO surface visible up to 21 days immersion.

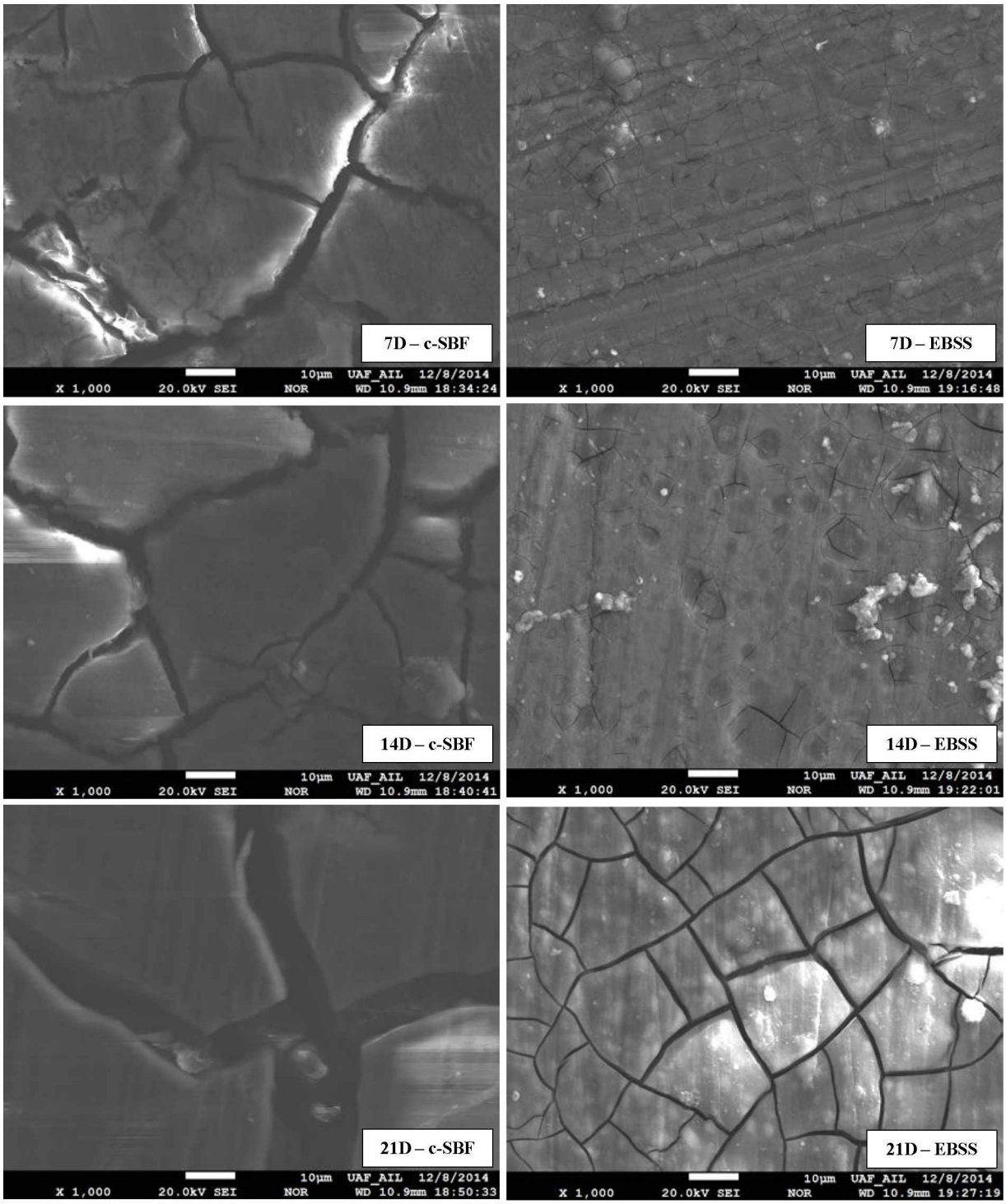

Figure 2.35: Bare AZ31 substrate SEM imaging (1000x) of corrosion progression in c-SBF (left column) vs. EBSS (right column)

The Bare AZ31 shows a significant difference in corrosion progression between the c-SBF and EBSS solutions. At 7 days immersion the c-SBF samples show large surface micro-cracks, the largest of which

remain at approximately 6 μm in width until a sharp increase at 21 days immersion. The EBSS samples show small, localized, cracks beginning to develop on the surface at 1 day. These small cracks are more numerous and evenly distributed at 7 days immersion (shown above). The crack growth progresses and reaches a typical width of 1-2μm at 21 days in the EBSS.

Each SEM image was evaluated for maximum crack width in an effort to organize and visualize the large amount of SEM data in one chart. The maximum crack width is plotted against immersion time for each sample group below:

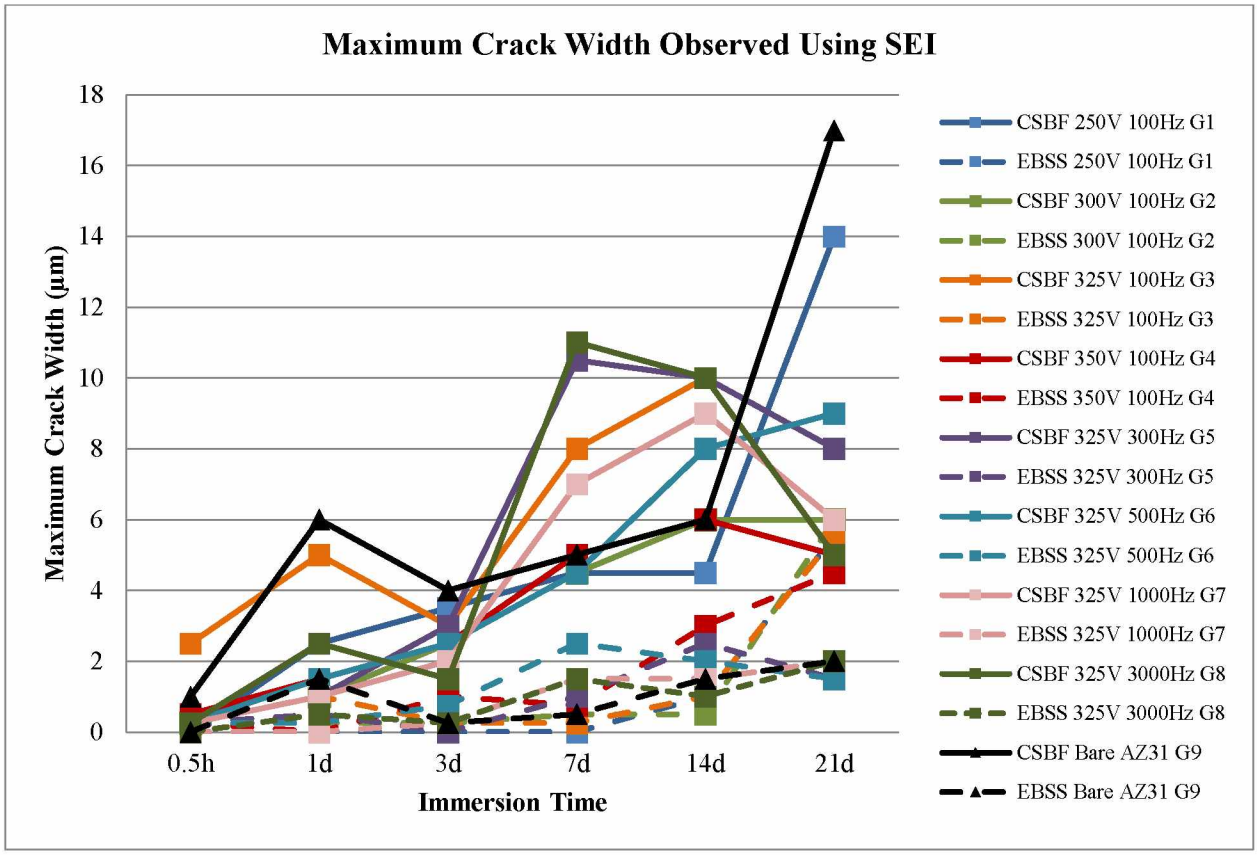

Figure 2.36: EBSS vs. c-SBF immersion effect on maximum crack width observed

Maximum crack width observed on SEM for c-SBF groups was generally larger than that seen in the EBSS specimens. A larger variation between immersion timepoints and groups is seen for the c-SBF samples. EBSS samples show very slow increase in maximum crack width with many groups showing 'hairline' (<0.50μm) cracks up to 14 days immersion. All EBSS groups achieve crack sizes > 2μm at or before 21 days immersion.

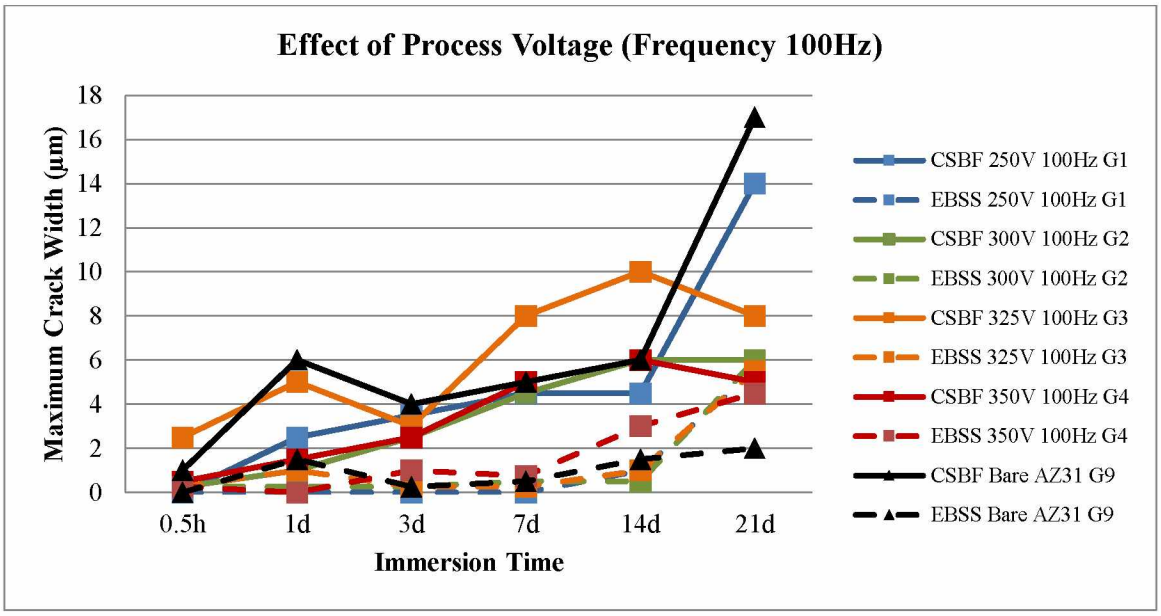

Figure 2.37: Maximum crack width observed on SEM for groups of varying process voltage

The slowest crack width progression for c-SBF samples is seen for the 300V and 350V groups with the 250V group showing similar performance up to 14 days immersion. All MAO coated EBSS samples show similar (<2µm) max crack width up to 7 days with a dramatic increase observed at the 21 day timepoint.

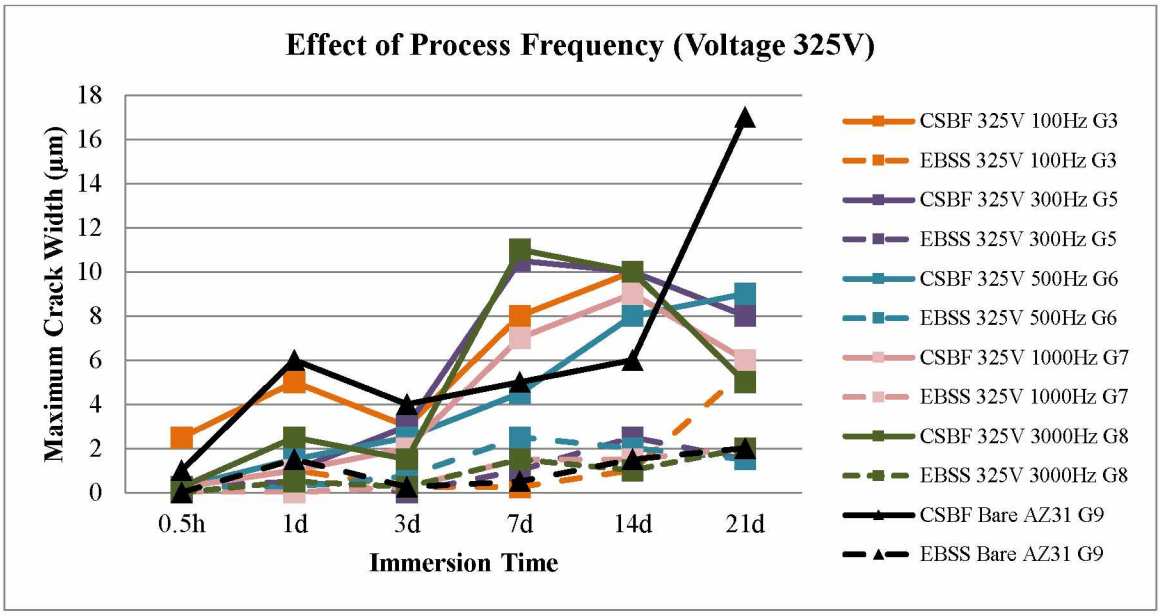

Figure 2.38: Maximum crack width observed on SEM for groups of varying process frequency

Among c-SBF groups, the slowest increase in crack width up to 3 days immersion was seen in the four highest frequency groups. Process groups of 500Hz and 1000Hz were consistently lower in crack width than the other MAO groups between 3 and 14 days immersion. The bare AZ31 substrate showed similar surface crack propagation as the lowest frequency MAO groups until a dramatic increase in crack size at 21 days immersion. All EBSS groups showed a crack size < 2μm prior to 7 days immersion with the highest frequency groups (1000Hz, 3000Hz) staying at or below 2μm crack size for the entire immersion period.

2.3.4.3 Energy Dispersive Spectrometry

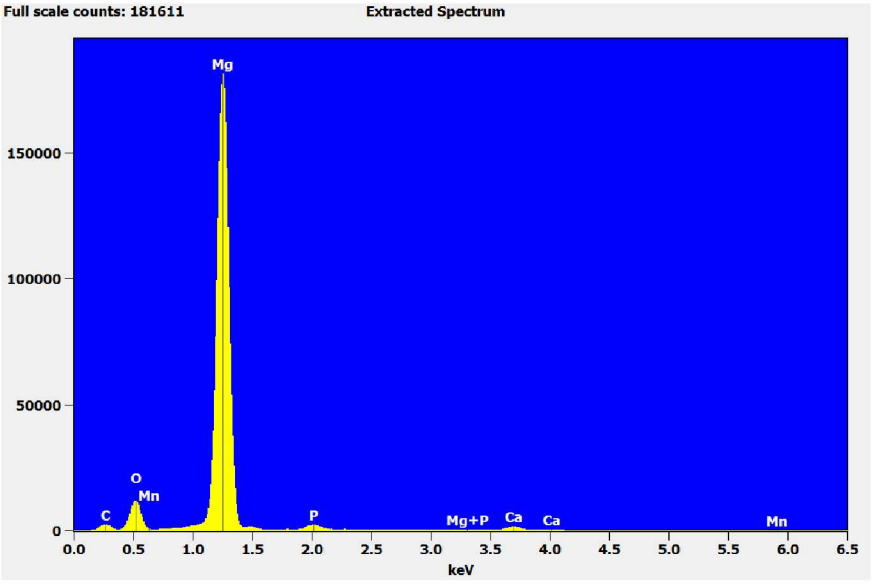

Figure 2.39: EDS mapping of Bare AZ31 substrate at 0.5H immersion in c-SBF

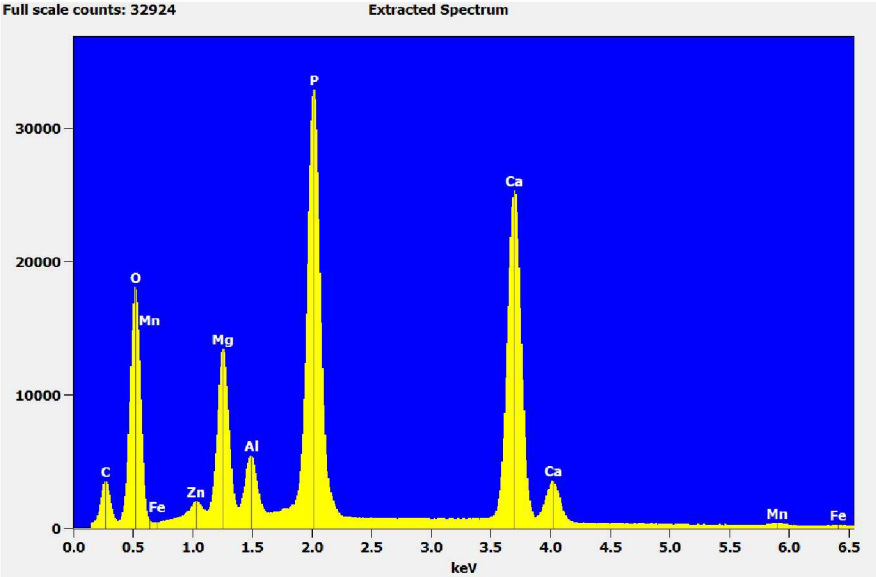

Figure 2.40: EDS mapping of Bare AZ31 substrate at 7D immersion in c-SBF

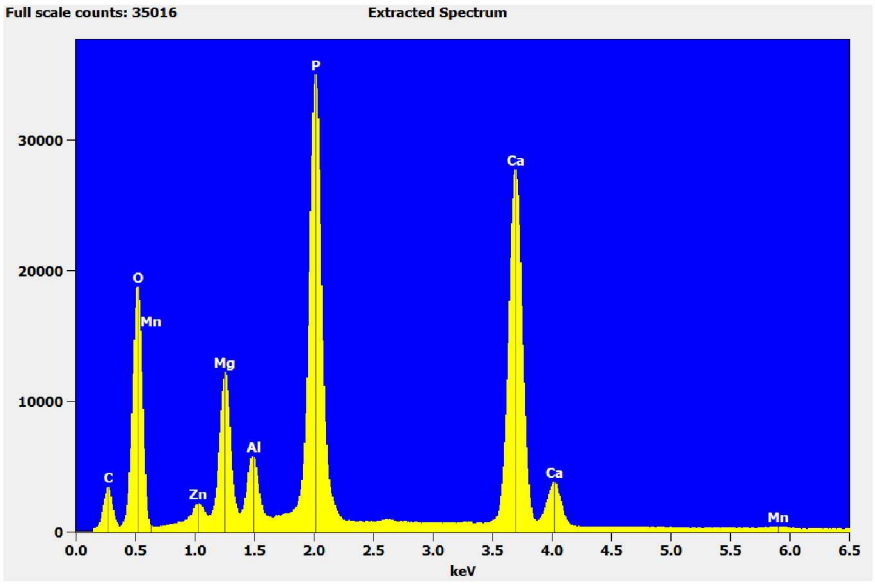

Figure 2.41: EDS mapping of Bare AZ31 substrate at 21D immersion in c-SBF

With increasing immersion time, the uncoated AZ31 material shows a rapid onset of corrosion products as seen by the increase of oxygen, phosphorous, and calcium element composition. These products act as a passive layer of protection for the underlying AZ31 material and results in an increase in barrier resistance and decrease in current density seen through EIS and PD scans.

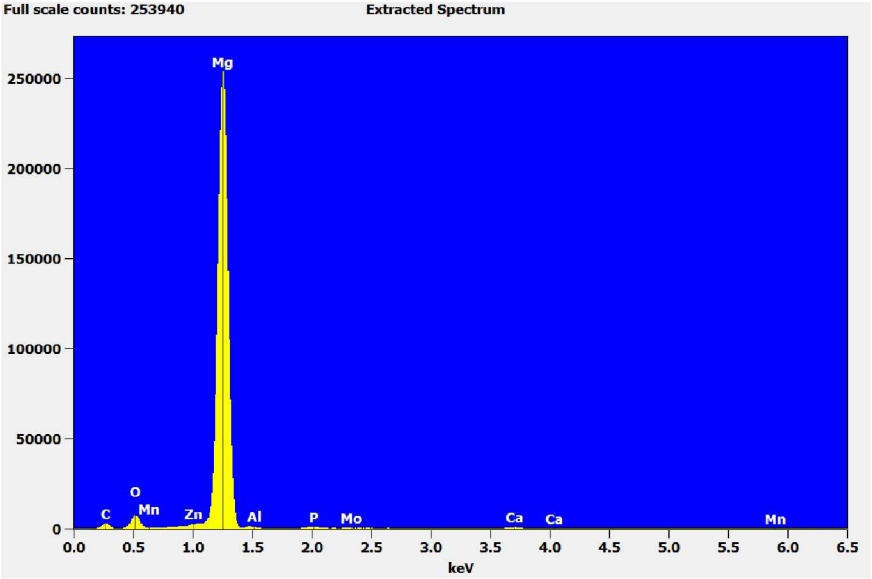

Figure 2.42: EDS mapping of Bare AZ31 substrate at 0.5H immersion in EBSS

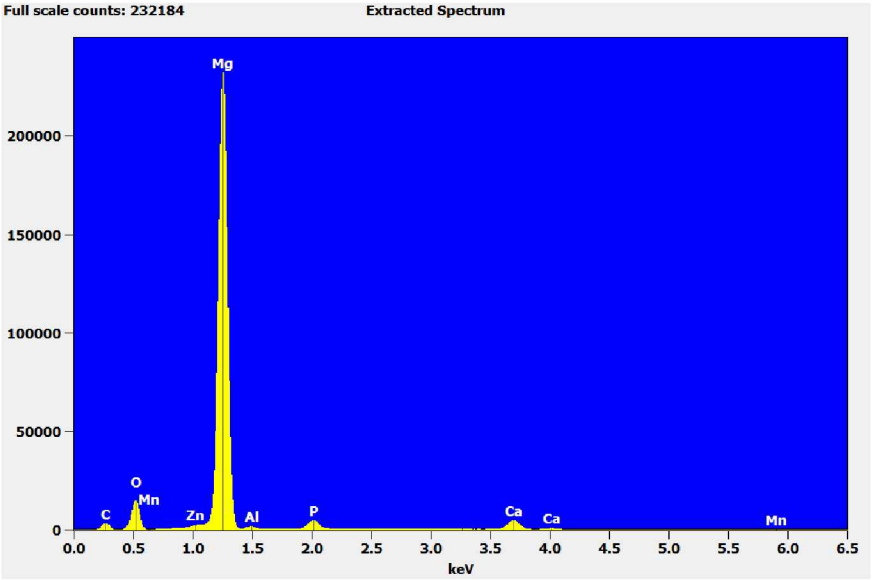

Figure 2.43: EDS mapping of Bare AZ31 substrate at 7D immersion in EBSS

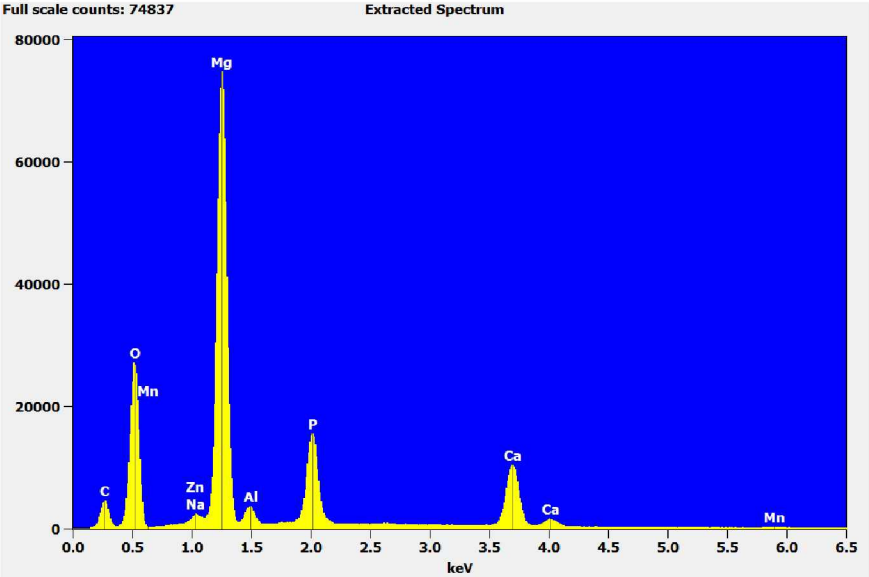

Figure 2.44: EDS mapping of Bare AZ31 substrate at 21D immersion in EBSS

In contrast to the c-SBF, EBSS shows a less aggressive attack and breakdown of the uncoated material. A slight increase in oxygen, phosphorous, and calcium elements can be seen from 0.5H-7D immersion due to a thin passive coating forming on the sample (seen in macroscopic images). This film layer sustains until breakdown around 21D and further corrosion of the base material. As corrosion progresses, corrosion products are visible from macroscopic imaging and can be seen in EDS mapping through a spike in oxygen, phosphorous, and calcium element composition at 21D.

2.4 Discussion

An increase in MAO coating thickness with an increase in process voltage was observed for groups with a constant frequency of 100Hz. This trend is in line with previous research performed using these same process settings and materials. However, the largest thickness observed here (10.6μm) was well below that observed in the previous research (around 20μm) [36]. Also, all MAO process groups showed thicknesses within a 6.2μm window. As a result, the c-SBF showed an immediate breakdown and quick progression of cracks observed by SEM. Group 1, with the lowest thickness, showed earliest dissolution of MAO pores within 1 day immersion. All c-SBF group samples demonstrated visible change in surface color within 0.5H immersion with corrosion progressing to large pits and mass loss beyond 14 days. In contrast, the EBSS groups retained a light gray MAO appearance out to as far as 3 days for some groups. Macroscopic appearance of EBSS samples at 21 days most matched the appearance of 0.5H and 1D c-SBF samples. SEM surface imaging of 7D c-SBF and 21D EBSS (Group 4) appeared very similar, demonstrating the immersion time required for the EBSS solution to match the corrosion produced in the

c-SBF solution. This gap in corrosion vs. immersion time was consistent across all groups and shows the delay provided by the lower chloride composition EBSS. The bare AZ31 material showed the largest microscopic cracking of any group as early as 0.5H immersion. This demonstrates the corrosion protection provided by the MAO coating regardless of process variation.

Qualitative trends in morphology were reflected in the EIS bode plots of impedance vs. frequency. For the 100Hz groups of increasing voltage, the largest impedance was found for groups of increased voltage. This trend fits well with the increase in thickness observed with voltage on cross section imaging. The bare AZ31 material showed the lowest impedance of any group for both EBSS and c-SBF. The EBSS samples showed a much higher impedance on the bode plots when compared to c-SBF at 0.5H immersion, corresponding to the higher corrosion resistance at this time period. The bare AZ31 material showed a gradual rise in c-SBF impedance with time brought on by oxidation of the surface and formation of corrosion products visible on macroscopic observation.

The potentiodynamic scans showed a similar trend to those seen by EIS observation, the EBSS samples demonstrated a higher corrosion resistance compared to c-SBF. For groups of increasing voltage and 100Hz frequency at 0.5H immersion, I_{corr} values decrease with increasing voltage. This trend matches that seen in EIS data and with cross section thickness increase vs. voltage. EBSS curves were located more passive and at lower current density when compared to c-SBF curves. With increasing immersion time the EBSS curves moved toward higher current density, approaching the c-SBF counterparts. This transformation corresponds to the impedance changes observed by EIS and shows the corrosion time gap between the fluids.

Through the observations discussed above (EIS, PD Scan, SEM image, and EDS results) an explanation of corrosion progression between the different sample groups can be developed.

2.4.1 MAO c-SBF Sample Progression

The MAO coated samples in c-SBF show a rapid attack by the solution forming cracks and dissolving the MAO layer (fully dissolved by 7-14D). This is seen through immediate discoloration and onset of cracking in macroscopic and SEM imaging. The cracking of the MAO layer allows for the c-SBF to corrode the underlying substrate and the overall circuit resistance decreases in the EIS data. After an initial corrosion period (3-7D) a gradual rise is seen for barrier resistance values and a large amount of corrosion products are seen on EDS. These corrosion products aid in slowing the corrosion rate of the sample with increased time.

2.4.2 MAO EBSS Sample Progression

In EBSS the attack is less severe as seen in c-SBF due to the lower chloride concentration and the ability for the solution to form protective calcium phosphate layers [51]. The MAO layer remains on the sample up to 21D immersion and demonstrates an approximate 2 week gap in corrosion damage as compared to c-SBF samples. As the MAO breaks down at 14D, large cracks appear resulting in a drop in barrier resistance and increase in current density. At 21D these cracks allow corrosion of the underlying substrate and corrosion products are seen to be forming on the surface.

2.4.3 Uncoated c-SBF Sample Progression

With an early onset of large cracks, the uncoated group shows the highest initial corrosion rate. This rate drops as the samples approach 3D immersion time due to the development of corrosion products on the sample surface. These corrosion products result in a drop in current density and increase in barrier resistance. A large increase in corrosion product elements is seen on EDS and SEM imaging at later timepoints.

2.4.4 Uncoated EBSS Sample Progression

There is an immediate discoloration of the surface visible on macroscopic imaging (i.e. thin film layer forming). This film layer provides an early increase in barrier resistance and decrease in current density for the bare substrate material. The film, an oxide layer of Mg and small amounts of Ca and P, provides for a slower progression of damage compared to the c-SBF groups. Eventually, 14-21D, the protective layer is broken down by the solution and corrosion products form on the surface. The gap between EBSS and c-SBF is due to the less aggressive nature of the lower chloride concentration and the CO2 buffering mechanism which provides for formation of protective calcium phosphate layers [51].

2.5 Conclusions

Qualitative macroscopic and SEM imaging was compared with quantitative data extracted from potentiodynamic polarization scans and electrochemical impedance spectroscopy for MAO samples of various process parameters immersed in EBSS vs. c-SBF. The results provide clear trends with regards to the following:

- EBSS samples showed increased impedance and decreased current density compared to c-SBF samples at the same immersion timepoints. The c-SBF demonstrated a much higher corrosion rate (I_{corr}) than EBSS across all process variation groups.

- EDS mapping of MAO cross section samples highlighted boundaries of coating via elemental composition and showed an increase in thickness with increased process voltage. Increased thickness for 100Hz samples was reflected in increased impedance (EIS) and decreased I_{corr} values for 0.5H immersion.

- EIS and potentiodynamic curve progression vs. immersion time showed EBSS samples trending toward c-SBF values at 21 days immersion. c-SBF samples are reaching a steady corrosion rate with corrosion product layers providing some protection of substrate. EBSS samples are reaching the point of MAO layer dissolution previously seen for c-SBF samples 7-14 days prior.

Chapter 3: Preliminary Characterization of PCL Dip-coated AZ31 Corrosion Resistance Evaluated by Electrochemical and Mechanical Testing in Simulated Body Fluid

3.1 Test Rationale and Strategy

Biodegradable polymer coatings have been gaining interest for use as coating materials in magnesium alloy research. These materials can be prepared easily within a lab setting and can potentially be modified for drug delivery and nanoparticle doping [33]. With a long history of use as biodegradable suture materials, PCL, PLGA, and PLA coatings have been recently explored on magnesium substrates for orthopedic applications [39, 41, 45, 46]. While corrosion resistance has been improved by these materials through in vitro and in vivo testing, there has not been published work comparing c-SBF and EBSS. Nor has there been research focused on the influence of stress or sample deflection during corrosion. Additionally, it is suspected that surface imperfections and the production of hydrogen gas, through Mg corrosion, could undermine a polymer coating [45]. As AZ31 is an alloy type which is said to be susceptible to stress corrosion cracking (environmentally assisted cracking), mechanical testing is important in progressing the evaluation of these coatings. Large dimension constant extension test samples are not common in this research area as the focus has been toward electrochemical coupons and small cylindrical tensile specimens. The experiment in Chapter 3 aims to observe basic mechanical-corrosion testing on samples which conform more closely to ASTM bend test guidance (ASTM G39). Comparison of coated vs. uncoated sample performance explores the influence of polymer coatings in delaying mechanical failure in a corrosive environment. The results of this experiment may guide future research goals relating to coating adhesion, stress limitations, and experiment development. The outline for this experiment is shown below with materials, methods, and results presented in Chapter 3.

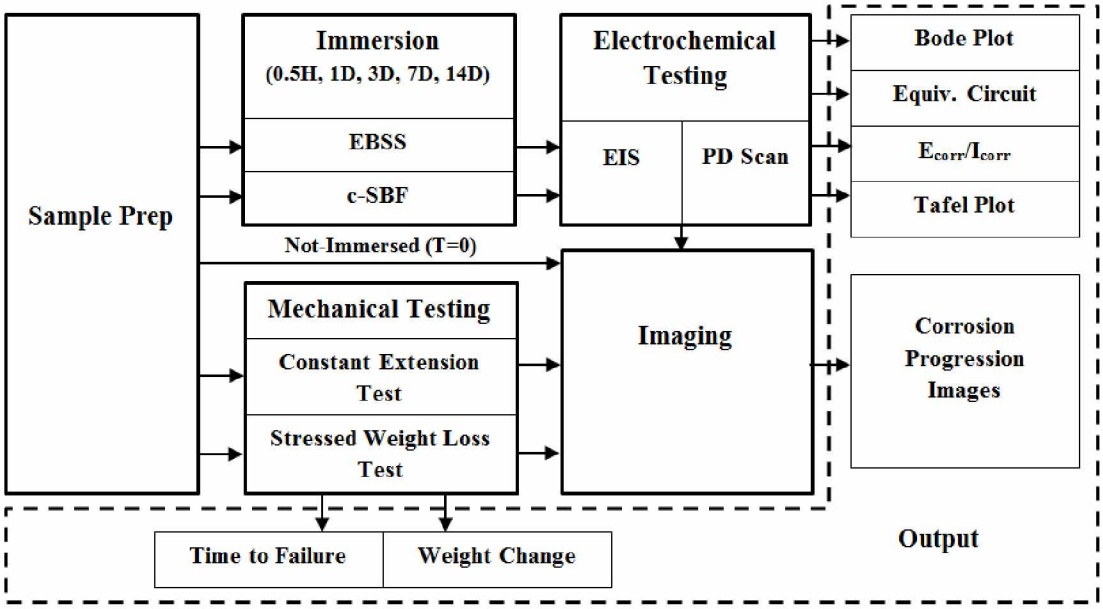

Figure 3.1: Test path for PCL coated vs. uncoated AZ31 sample immersion and mechanical testing

3.2 Experimental Setup

3.2.1 Sample Preparation

Commercially obtained AZ31B sheet metal (0.040" thickness) was polished with SiC paper at grits up to 1200 and cleaned with Acetone. Rectangular specimens were cut from the sheet of dimensions 1x1cm for immersion and electrochemical testing. Four point bending specimens were cut with footprint of 1x5 inches (2.54x12.5cm). Polycaprolactone, PCL (80,000mw) was mixed with Dichloromethane (DCM) to obtain a dip coating solution of 5% w/v. The solution was stirred continuously for 5 hours in a covered glass beaker. Dip coating sequence involved immersing the specimen for 30 seconds, holding in fume hood for 1 minute, then a repeated immersion for 30 seconds, after which the sample was dried in a fume hood for at least 24 hours prior to testing.

3.2.2. Immersion Solutions and Timepoints

Two SBF variants (c-SBF and EBSS) were produced for immersion and electrochemical testing with ion compositions shown in Table 1.9. All solution preparation, sample immersion, and electrochemical testing was conducted within a pH range of 7.2-7.4 at 37°C. The c-SBF solution was buffered with Tris (hydroxymethyle) minomethane $(CH_2OH)_3CNH_2$ and pH adjusted using 1 kmol/m^3 HCl. The solution was prepared by combining the reagents (Table 1.8) in order in deionized water with constant stirring. The EBSS solution was produced by combining NaCl, $NaHCO_3$, KCl, $MgSO_4$, NaH_2PO_4-H_2O, and Glucose in deionized water with constant stirring. The portion of $CaCl_2$ was dissolved separate in 150ml deionized water then added to the salt solution. The pH of EBSS was adjusted to 7.2-7.4 by bubbling

CO_2 through the solution. A specimen from each group, for each SBF, was immersed in 50ml (0.20ml/mm^2) of SBF for periods of 0.5hr, 1d, 3d, 7d, and 14d with solution replaced daily. For constant extension testing, c-SBF was used with a volume of 1400 ml (0.20ml/mm^2) replaced every 7 days for up to 21 days immersion.

3.2.3 Electrochemical Testing

The electrochemical equipment used was a 3-cell system consisting of glass test vessel, graphite counter electrode, SCE (saturated calomel electrode), and the working electrode (Specimen). The system was driven by a Gamry G300 potentiostat and Echem Analysis software. Samples removed from immersion at each timepoint were rinsed with DI water and attached to the electrochemical working electrode post and immersed in 300ml of the solution of interest (EBSS or c-SBF) at 37±2°C. The non-specimen portion of the working electrode rod was coated in wax, leaving an exposed specimen area of approximately (1.86 cm^2). The specimen was immersed for 10 minutes prior to monitoring Open Circuit Potential (10 minutes), EIS, and Potentiodynamic Scans. Electrochemical Impedance Spectroscopy (EIS) was conducted in the range of 100kHz to 0.2Hz with an AC voltage amplitude of 10mv. Potentiodynamic scans were conducted at a rate of 1 mV/s.

3.2.4 Sample Characterization and Morphology

Non-corroded PCL specimens were potted in epoxy, cross-sectioned, and carbon coated for SEM imaging. SEM was performed at 20kev and 20nA at a magnification of 400X. Samples removed from immersion were digitally photographed before and after electrochemical testing.

3.2.5 Mechanical Testing

It is desired to set up constant extension specimen at an estimated applied stress level such that the influence of various stress amounts can be observed when multiple sample groups are tested. Sample groups may be classified as applied stress (ex. 100MPa, 150MPa) or % of YS (Ex. Group 1: 50% YS; Group 2: 5% YS, etc). For the experiment outlined here, the deflection amount for constant extension testing was determined through Solidworks FEA simulation of a four-point bending event. The simulation was configured with dimensions corresponding to ASTM G39 fixture (Figure 1.11): h = 2in, H = 4in, A 1in, t = 0.038in. Sample footprint was 1 x 5 inches with assigned elastic modulus of 45000 MPa (Solidworks Magnesium Alloy).

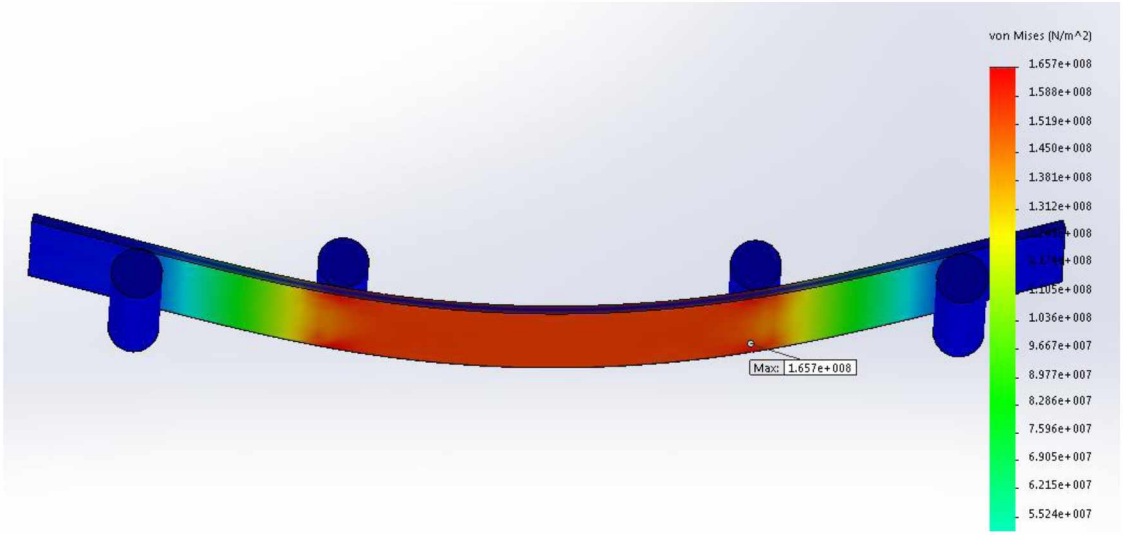

Figure 3.2: Solidworks FEA four-point loading of AZ31 sample

ASTM G39 provides guidance for estimating the midspan stress of four point bend samples conforming to the geometry shown in Figure 1.6. The stress is estimated through the equation below:

$$\sigma = \frac{12 \cdot E \cdot t \cdot y}{(3 \cdot H^2 - 4 \cdot A^2)} \tag{15}$$

Where E and t are the material elastic modulus and thickness while y, H, and A are determined by the parameters of the test/fixture. Yield strength was estimated at 220MPa for AZ31B H24 sheet material [91]. The Figure below shows the results of the FEA analysis vs. theoretical midspan stress estimation per ASTM G39.

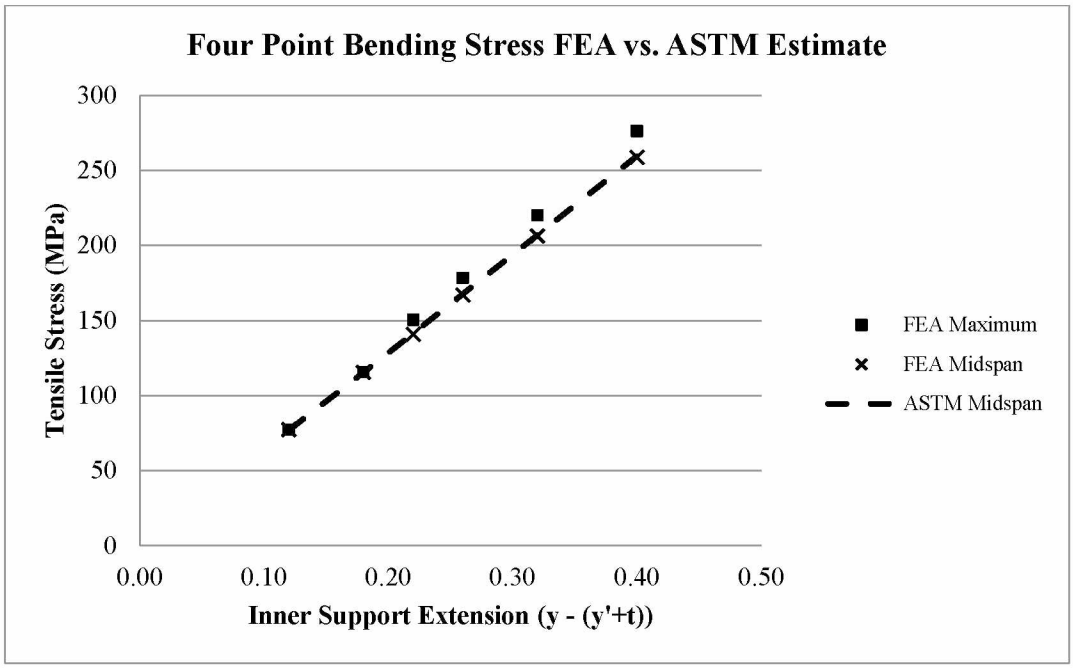

Figure 3.3: FEA Simulation Results vs. ASTM Estimate

The maximum tensile stress typically appeared just inside of the inner supports of the bend fixture. The variation between mid-span stresses and maximum stress for each deflection simulation was less than 7%.

A four point constant extension jig, constructed of high density polyethylene was used matching the design shown in Figure 1.6. The dimensions corresponding to the guidance in ASTM G39 were: h = 2in, H = 4in, and A = 1in. The constant extension test samples were measured and weighed prior to loading and immersion.

Table 3.1: Test specimen variants for constant extension testing in c-SBF

Sample Type	Replicates	Applied Extension (y-(y'+t))	Estimated Applied Stress (MPa)
Bare AZ31	3	N/A	N/A
	3	0.18"	115.6
	3	0.32"	220.1
PCL + AZ31	3	N/A	N/A
	3	0.18"	115.6
	3	0.32"	220.1

A total of 18 samples were loaded into stress jigs (if applicable) and immersed for up to 21 days with pictures taken at 3, 7, 14, and 21 days. At 21 days immersion the samples were rinsed with DI water, dried, and weighed for final weigh loss calculation.

3.3 Results

3.3.1 PCL Coating Thickness

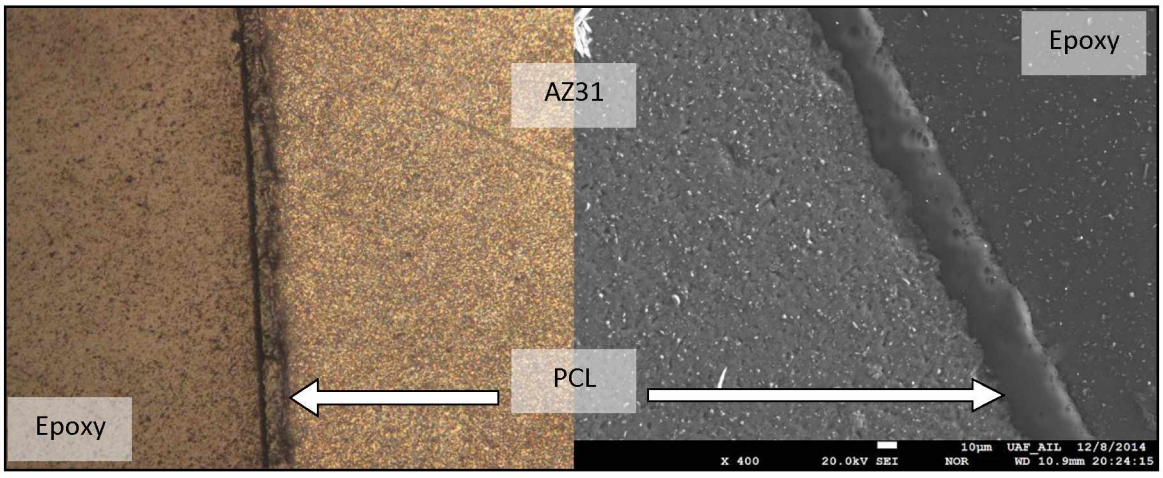

Figure 3.4: Microscope (Left) and SEM (Right) imaging of PCL on AZ31 cross section

The dip coating process produced a well-defined, consistent layer of PCL coating on the substrate. This layer was shown to be approximately 20-25 µm through SEM inspection. The thin layer appeared

translucent on the AZ31 substrate and did not provide a noticeable increase in overall sample thickness when compared with groups of non-coated samples.

3.3.2 Electrochemical Impedance Spectroscopy / Equivalent Circuits

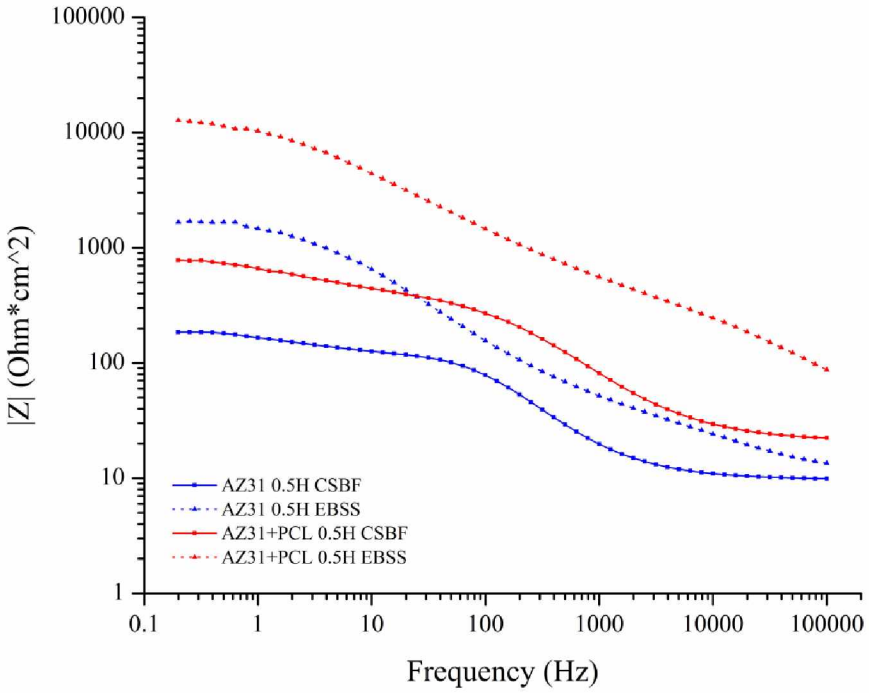

Figure 3.5: EIS Bode plot at 0.5H immersion time for coated vs. uncoated samples in c-SBF and EBSS

The bode plot for 0.5H immersion shows an increased impedance for PCL coated samples when compared to the bare AZ31 substrate. The EBSS samples also show increased impedance over the c-SBF samples with uncoated AZ31 in EBSS performing at a similar impedance level as coated c-SBF.

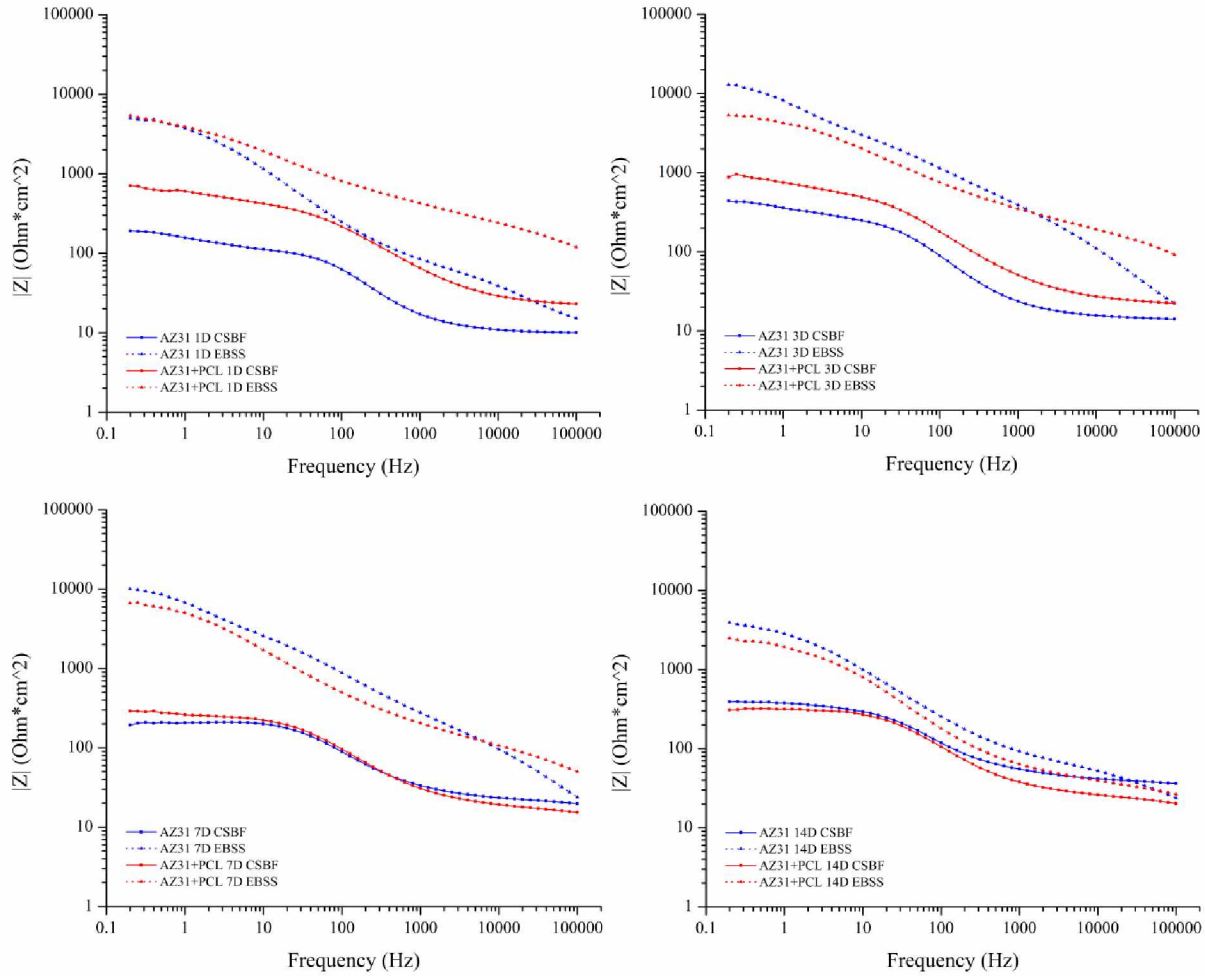

Figure 3.6: EIS Bode plots of increasing immersion time for coated vs. uncoated samples in c-SBF and EBSS

The progression of bode plots over the immersion period shows a drop in impedance with time for the coated samples. The uncoated samples show a brief rise then fall in impedance with increased immersion time. The EBSS samples show consistently higher impedance throughout the entire test period for both coated and uncoated samples.

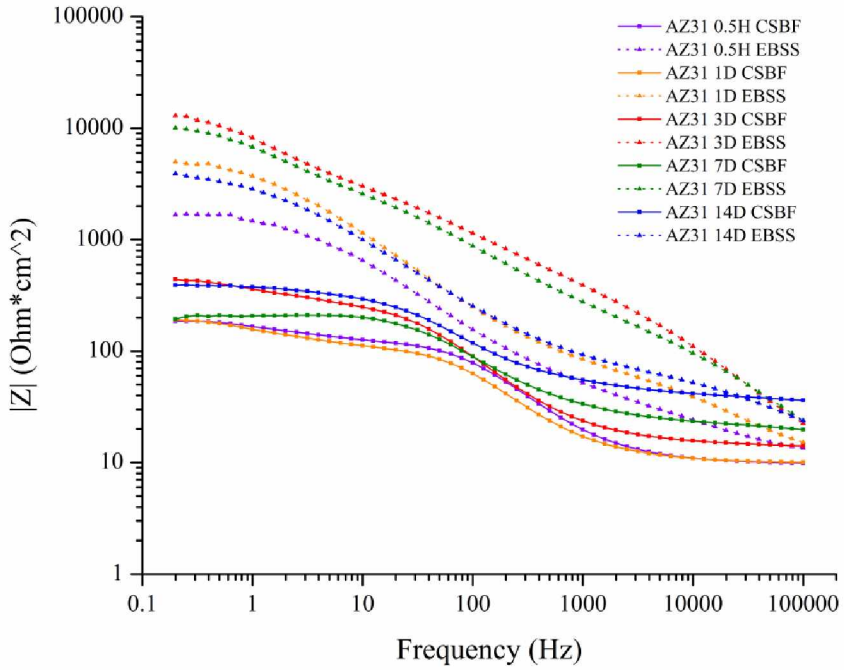

Figure 3.7: Bode plot of AZ31 substrate corrosion progression in EBSS and c-SBF

Impedance plots for the bare substrate rise with immersion time in c-SBF. In EBSS, the bode plot rises initially then falls back toward the initial values at 0.5H.

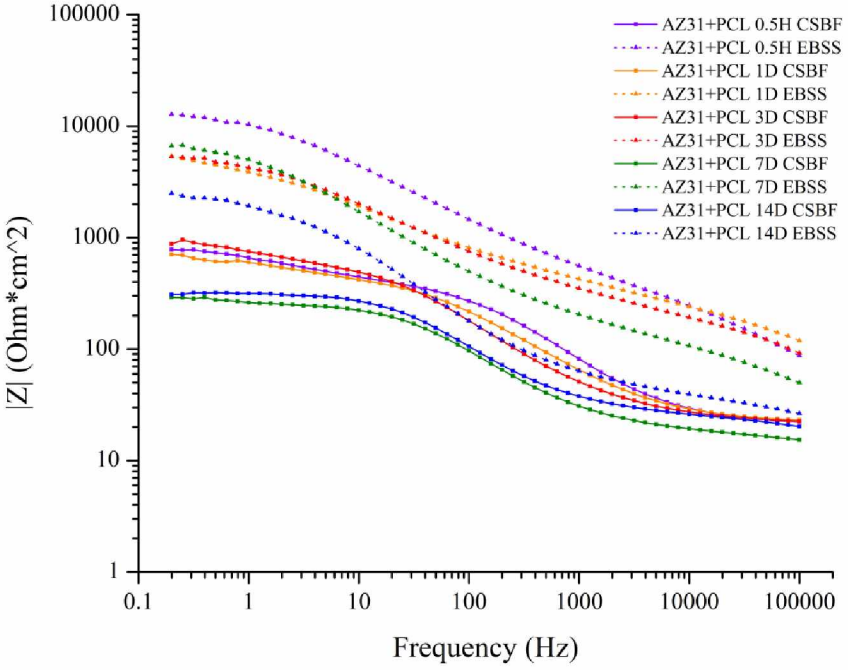

Figure 3.8: Bode plot of PCL coated AZ31 corrosion progression in EBSS and c-SBF

For coated samples, both c-SBF and EBSS groups fall in impedance with increased immersion time. At 14 days immersion the EBSS impedance plots approach the early immersion time plots for c-SBF samples.

Table 3.2: R_b values determined by EIS equivalent circuit fit

	EIS Result Rb (Ω/cm^2)				
Group	**0.5H**	**1D**	**3D**	**7D**	**14D**
AZ31 c-SBF	341	167	609	184	338
AZ31 EBSS	1815	5514	27490	15280	4277
PCL + AZ31 c-SBF	1283	1208	1125	251	294
PCL + AZ31 EBSS	14500	5981	6004	8091	2713

R_b values for coated samples are consistently higher than for uncoated in c-SBF. The barrier resistance decreases with increased immersion time for the coated samples, consistent with the bode plots above. For the EBSS solution the resistance values increase for the uncoated sample, then decrease after 3 days immersion. All EBSS resistance values are higher than all c-SBF resistance values showing the difference in corrosion resistance for samples immersed in the different solutions.

3.3.3 Potentiodynamic Polarization

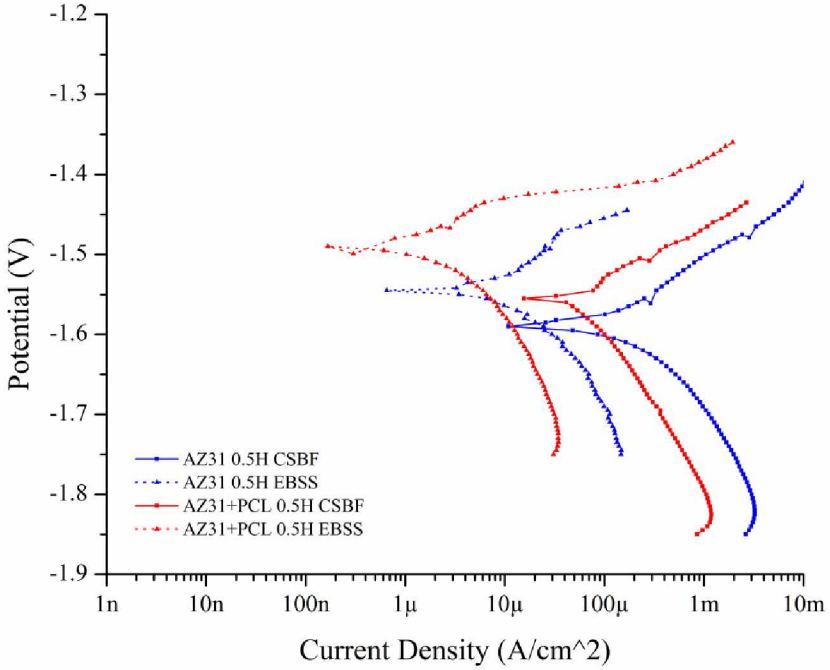

Figure 3.9: Potentiodynamic scans of 0.5H immersion samples coated vs. uncoated in c-SBF and EBSS

The tafel plot shows decreased current density for coated samples compared to uncoated samples in each solution type. Also, the EBSS solution shows a lower current density and slightly more passive potential compared to c-SBF.

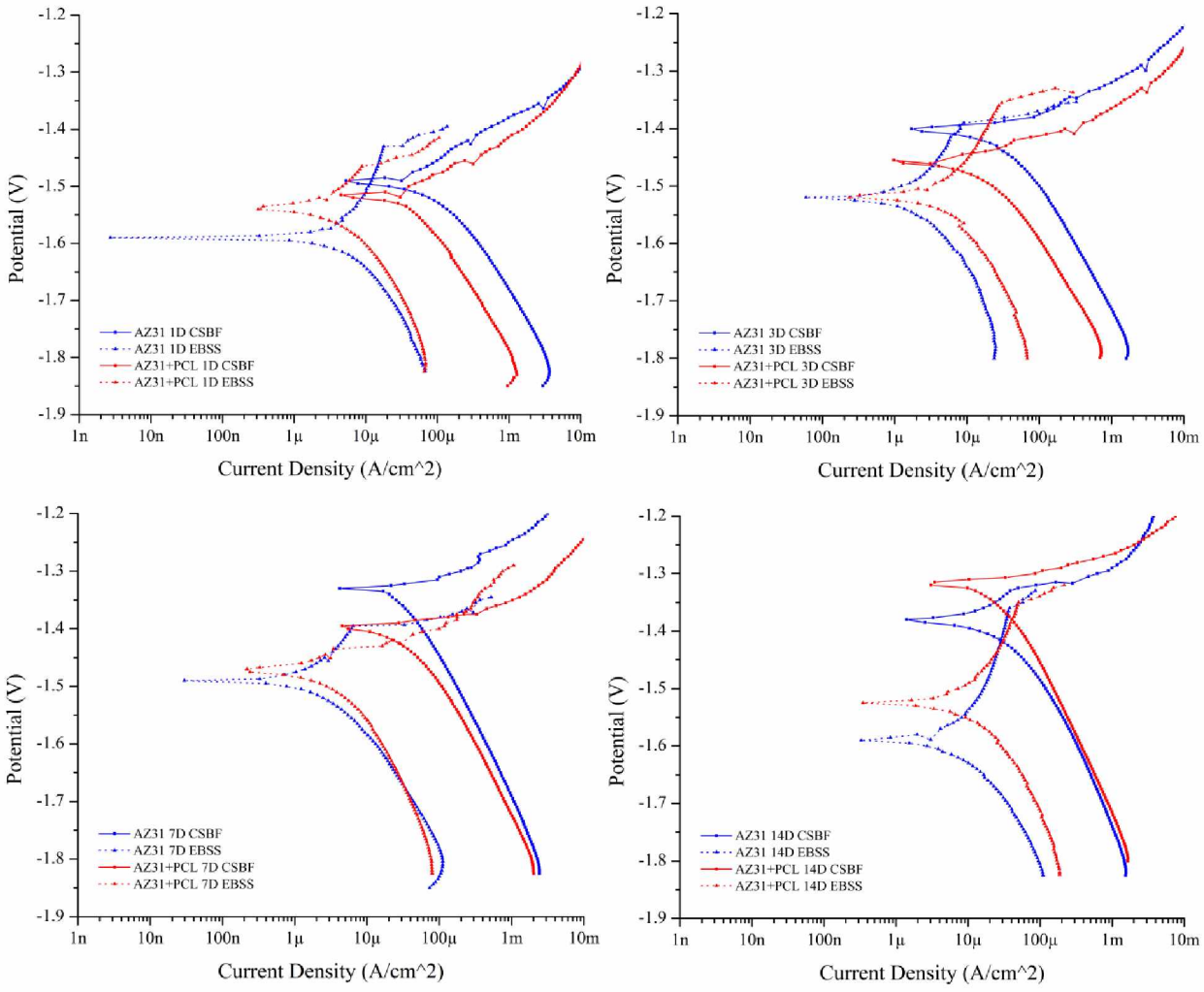

Figure 3.10: Potentiodynamic scans of increasing immersion time for coated vs. uncoated samples in c-SBF and EBSS

Progression of the tafel plots over the entire immersion period show similar trends as at 0.5H. The EBSS samples are located at a lower current density relative to c-SBF samples. With increasing immersion time, the separation between coated and uncoated current density for each solution appears to decrease. Also, the potential values for both coated and uncoated samples, in both solutions, increase with increasing time of immersion.

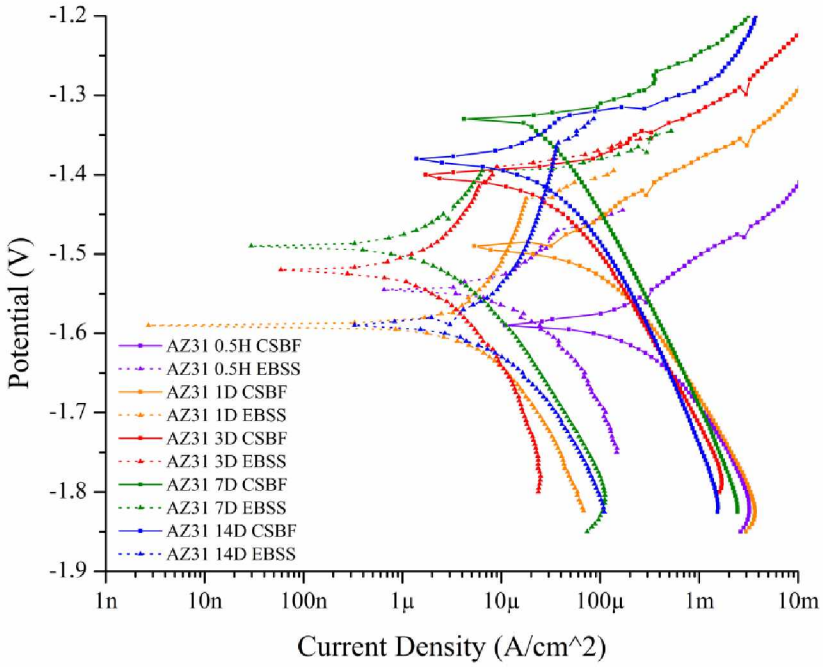

Figure 3.11: Bare AZ31 substrate corrosion progression in c-SBF and EBSS

The progression of the bare AZ31 substrate tafel plot demonstrates a passive shift with increasing immersion time for both EBSS and c-SBF samples. Current density for EBSS samples appears to decrease up to 7 days immersion, then increase back toward the starting point at 14 days.

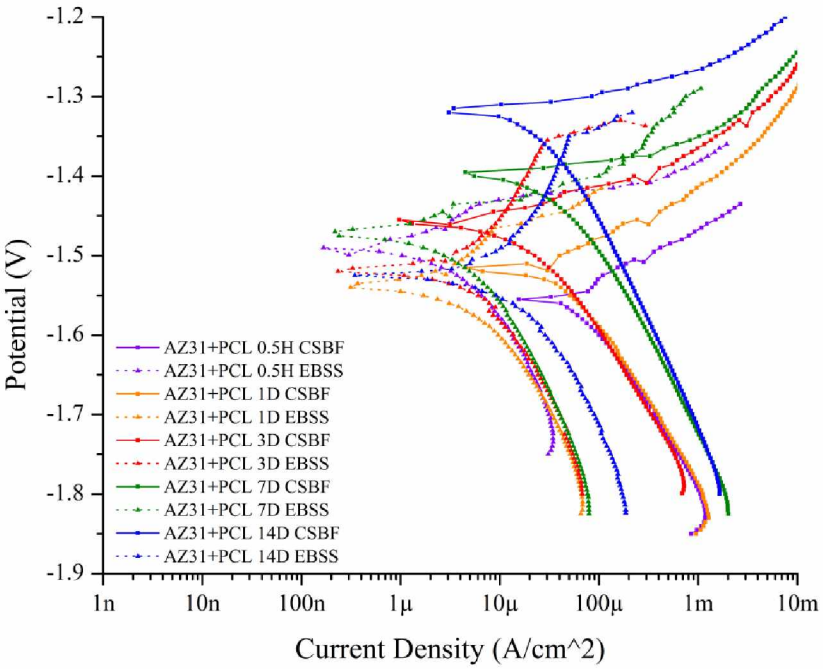

Figure 3.12: PCL coated AZ31 corrosion progression in c-SBF and EBSS

Progression of the tafel curves for the coated samples shows similar trends as seen in the uncoated sample with a gradual decrease in current density for c-SBF and passivation of the sample with increased immersion time. I_{corr} values were extracted for the plots and are presented graphically below:

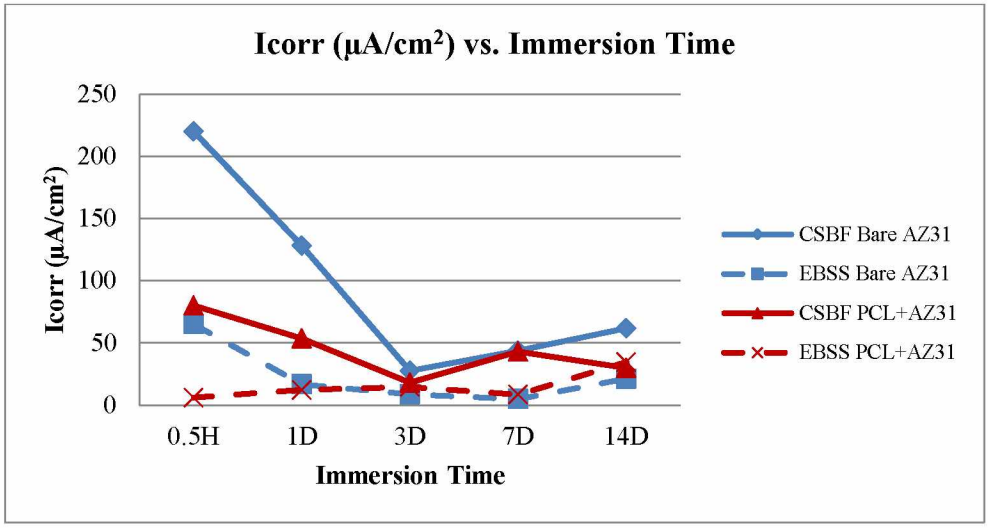

Figure 3.13: I_{corr} values vs. immersion time for coated and uncoated samples in CSBF and EBSS

The plot reflects the shifts observed in the potentiodynamic plots above where the c-SBF bare AZ31 samples show largest corrosion rate early and level off after 3 days immersion. At the initial timepoint coated samples show a much lower current density compared with uncoated samples in the same solution. With increasing immersion time the current density for coated and uncoated samples appears to converge.

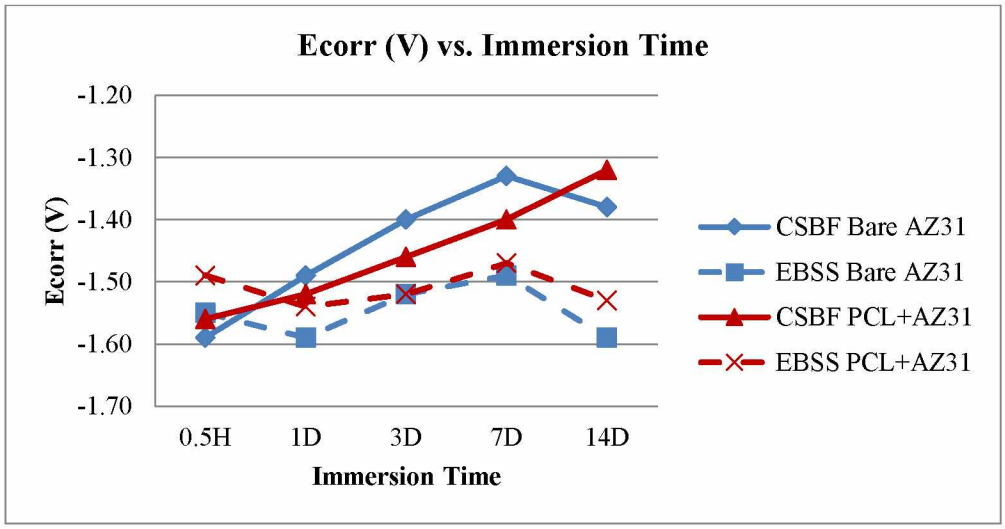

Figure 3.14: Ecorr values for coated and uncoated samples vs. immersion time

Ecorr values are plotted above highlighting the trend observed in the tafel plots. With increasing immersion time the c-SBF samples show increased passivity. Initially the coated samples show a higher passivity than the bare substrate. With increased time the bare c-SBF samples rise in Ecorr and level off around 7 days immersion as corrosion products form a layer of protection then begin to breakdown (at 14D).

3.3.4 Corroded Surface Morphology

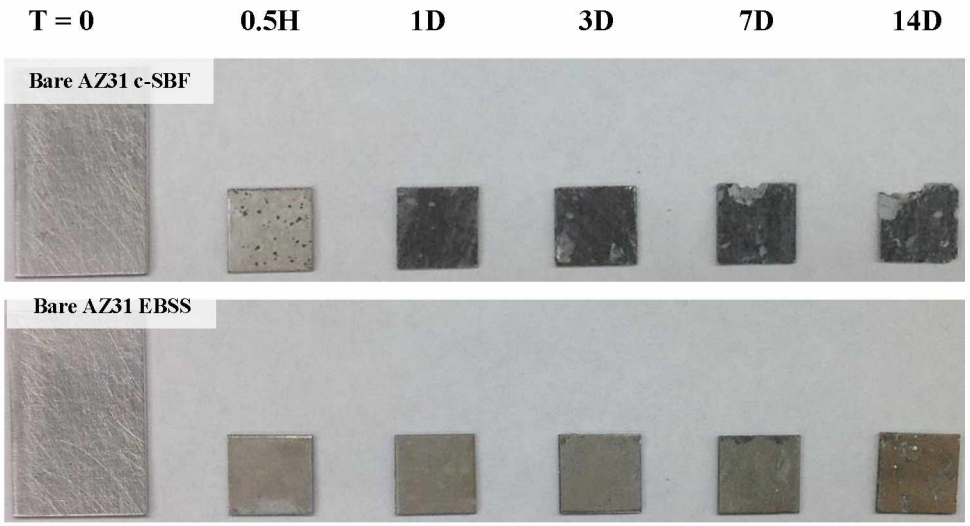

Figure 3.15: Bare AZ31 substrate macroscopic corrosion progression in EBSS and c-SBF

The uncoated sample show immediate change in surface appearance at 0.5H immersion. For EBSS the surface appears as a dull gray/brown while the c-SBF shows dark blotches across the surface. After 1 day immersion the c-SBF samples have become dark gray with some faint appearance of white corrosion products on the surface. The EBSS samples continue to darken in appearance with some edge corrosion/defects appearing around 7 days immersion and corrosion products at 14 days. The c-SBF samples show significantly more corrosion than EBSS with large mass loss and defects starting at 3 days.

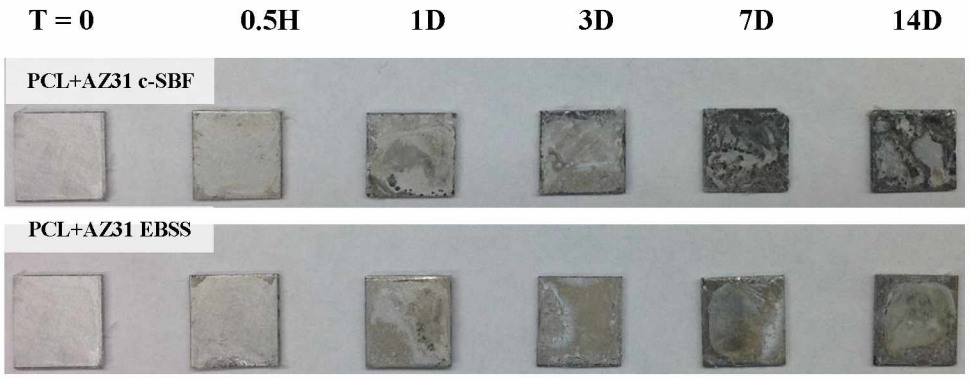

Figure 3.16: PCL coated AZ31 macroscopic corrosion progression in EBSS and c-SBF

The PCL coated samples show similar appearance after 0.5H immersion in either solution. There is little visible corrosion beyond the corners, where the PCL coating is least adhered to surface (visibly frayed). At 1 day immersion the c-SBF appears to be attacking the edges of the PCL coating turning the exposed substrate a darker gray color. The EBSS samples show minor edge defects up to 7 days where the PCL is visibly delaminating from the edges inward. By 7 days the c-SBF has significantly damaged the PCL coating and begun forming pits on the substrate surface. At 14 days there is little evidence of the PCL coating for the c-SBF sample and a heavy amount of white corrosion product appearing on the surface pits. In the EBSS at 14 days there remains a large section of PCL covering the center of the sample.

3.3.5 Constant Extension Testing

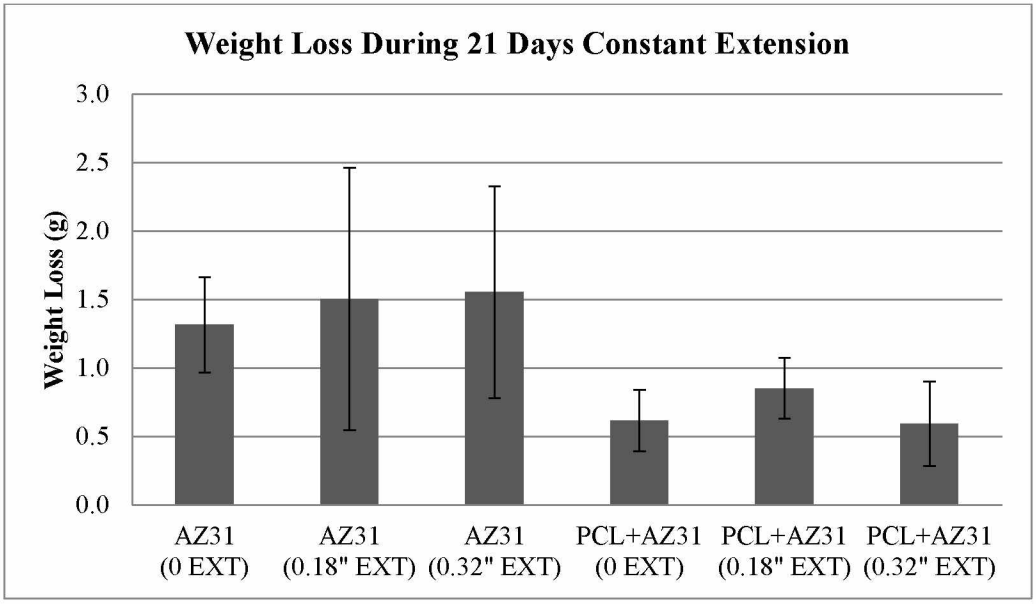

Figure 3.17: Weight loss of 21 day constant extension testing samples

On average weight loss values for both coated and uncoated samples were level with increasing extension. There is no notable increase or decrease in mass loss with increasing stress level imparted on the sample. Coated samples show a decreased average mass loss compared to uncoated samples, demonstrating the protective nature of the PCL coating.

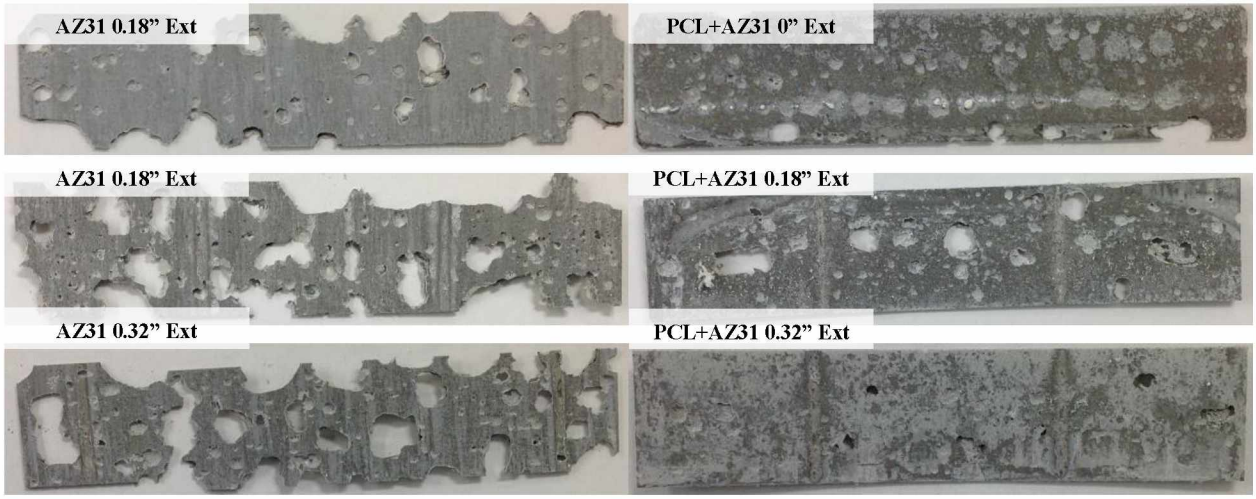

Figure 3.18: Macroscopic damage of 21 day constant extension samples

Macroscopic images show a clear increase in corrosion for uncoated vs. coated samples. All samples show consistent corrosion across sample (i.e. there is no preferential location with increased corrosion). One sample failed at 21 days immersion through cracking just outside a central loading contact point (Type: AZ31 0.32" EXT). However, this appears to be due to mass loss rather than a focused area of corrosion. Overall, the quantity of pits and loss of material, for all samples, appears equal at the center of sample (highest stress region) to the outside ends (where stress is lowest).

3.4 Discussion

The PCL dip coat process produced a relatively thin (20-25μm) layer of protection on the AZ31. However, this thin coating produced a noticeable increase in impedance plots for coated vs. uncoated samples at the initial immersion timepoint. With increasing immersion time the coated impedance values dropped gradually while uncoated values increased briefly before decreasing. EBSS barrier resistance values determined via EIS equivalent circuit fit were all higher than those for c-SBF immersion, showing the reduced corrosion provided by EBSS.

The tafel curves share many of the same trends seen in the EIS bode plots as the EBSS solution shows a consistently lower current density than that found in c-SBF. At the initial timepoint of 0.5H the coated samples show a decreased current density (lower corrosion rate) and increased Ecorr (increased passivity) compared to uncoated samples. This demonstrates the resistance to corrosion provided by the PCL coating. As immersion time approaches 3 days, the protection layer built up by corrosion of the bare AZ31 material decreases the current density before breaking down and increasing again after 3 days. Due to the PCL coating, the initial current density for the coated sample in c-SBF is significantly lower than that of the bare substrate. However, this coating quickly breaks down as the sample appears to match corrosion performance of the bare substrate after 3 days immersion. Current density for the coated EBSS sample remains low until the PCL begins to delaminate around 7-14 days as seen with a rise in current density.

Macroscopic observation shows stages of PCL coating breakdown and severe corrosion damage brought on by the c-SBF. At 1 day immersion in c-SBF the coated samples begin to delaminate at the edges and passivation of the underlying AZ31 material occurs through the corrosion reaction. This corrosion spreads inward forcing the PCL to separate from the underlying material until the coated sample appearance nearly matches that of the uncoated sample at 7 days immersion. This similarity in appearance reflects the similar corrosion performance observed by electrochemical testing at this timepoint. In the EBSS solution breakdown of the PCL coating occurs more slowly working inward from the edges of the sample. At 14 days immersion the EBSS sample retains a large section of PCL coating protecting the center face of the square sample. Summaries of the corrosion progression for each sample type are discussed in the sub-sections below.

3.4.1 PCL Coated c-SBF Sample Progression

The more aggressive c-SBF solution attacks frayed corners and thin sections of the PCL coating working to delaminate the protective layer from the edges inward. Rapid hydrogen development as c-SBF contacts the underlying substrate may exacerbate PDL delamination in the c-SBF over EBSS [45]. As underlying substrate is exposed, rapid corrosion and pit development takes place resulting in corrosion products and damage at increased immersion time. The electrochemical results for coated and uncoated samples approach similar values for impedance and current density as the coating is broken down.

3.4.2 PCL Coated EBSS Sample Progression

The solution produces a thin gray film layer at areas of frayed edges or thin coating. The delamination/breakdown of the coating occurs from the edges inward but at a much slower rate than with

the c-SBF solution. Large sections of PCL coating are still visible on the sample out to 14 days immersion demonstrating the less aggressive attack in EBSS vs. c-SBF.

3.4.3 Uncoated c-SBF Sample Progression

Similar to the results in Experiment 1, an early onset of large cracks and highest initial corrosion rate is seen for the uncoated sample in c-SBF. The current density drops as the sample approaches 3D with the development of corrosion products on the sample surface. The corrosion products result in a drop in current density and increase in barrier resistance. The worst damage is seen for this sample group, representing the worst case scenario in both experiments.

3.4.4 Uncoated EBSS Sample Progression

Early formation of a gray film coating provides increase in barrier resistance and decrease in current density. This protective layer leads to a slower progression of damage compared to the c-SBF solution. As discussed in Experiment 1, the film layer is sustained due to the less aggressive attack (lower chloride concentration) and ability to form protective calcium phosphate layers [51]. An increase in current density is seen at 7-14D as the film layer begins to breakdown and expose the substrate below.

3.4.5 Constant Extension Testing Discussion

Constant extension mechanical testing yielded no trend with increased stress level and mass loss. Variations within groups were larger than variations between stress level groups. Both mass loss and macroscopic imaging showed lower corrosion damage in the coated samples, demonstrating the protection provided by the PCL coating. There is no visible preference for corrosion at higher stressed regions of the sample. The lack of a trend with stress is likely due to the passive nature of the testing. With this form of constant extension testing there is no concentration point created and the sample tends to fail through mass loss rather than cracking due to constantly increasing applied load. More common testing in this area is slow strain rate testing (SSRT) which may allow a focus on crack nucleation and local progression of a specific region of increased corrosion.

3.5 Conclusions

A PCL coating was successfully applied to a polished AZ31 substrate resulting in improved corrosion performance in both EBSS and c-SBF body fluids. Observation over the course of 14 days revealed:

- At time of initial immersion (0.5H) coated samples provided a reduction in current density and less negative corrosion potential compared to uncoated samples demonstrating an improvement in corrosion resistance.

- Barrier layer resistance values found via EIS circuit fitting were consistently higher for EBSS samples than c-SBF samples demonstrating a gap in corrosion rate between the two solutions.

- PCL coating for immersion samples broke down at the edges of the sample and spread inward as the corrosive fluid spread beneath the PCL layer forcing the materials to separate. Breakdown of the coating occurred more quickly in c-SBF as compared to EBSS.

- Constant extension testing showed a lower mass loss for coated samples compared to uncoated samples. No trend was observed in mass loss vs. extension. No preference was seen for corrosion at areas of higher or lower stress (damage was uniform across surface).

Chapter 4: General Conclusions and Future Work

4.1 Conclusions

The experiments presented in Chapters 2 and 3 utilized both c-SBF and EBSS for immersion testing in an effort to compare the corrosion progression brought on by the differing ion concentrations. In both experiments the EBSS provided a clear reduction in corrosion rate as observed via electrochemical and qualitative test methods. This is consistent with observations made in literature that the c-SBF provides a harsh environment for corrosion testing due to the unnaturally high chloride ion concentration in the solution. While EBSS is believed to provide a closer fit with in vivo results seen in recent literature [51, 59] there may be some benefit to applying c-SBF to quickly test concept coatings.

The MAO coating method provided a noticeable improvement in corrosion resistance over non-coated samples despite a low thickness (5-10μm) across process groups. It was observed that MAO thickness increased with increasing voltage which provided an increase in initial impedance values observed on EIS bode plots. This result is consistent with previous findings for this material and coating method.

The basic PCL dip coating method resulted in a 20-25μm thick polymer layer which provided an improvement in corrosion resistance in both c-SBF and EBSS. While the MAO surfaces showed a gradual dissipation of pores and growth of microcracks across the surface, the PCL coating showed a noticeable breakdown in coating from the edges of the sample inward. It was seen that the PCL broke down quicker in c-SBF vs. EBSS and typically resulted in large sections delaminating/peeling off from the surface. In the less aggressive EBSS the PCL coating showed consistently low current density values up to 14 days immersion.

The results of constant extension testing did not yield any trends for increasing stress level vs. corrosion. The coating provided for a lower mass loss, however no preference for corrosion in locations of higher/lower stress was observed. The passive nature of the CET may have contributed to the lack of sample failures and observed trends with stress. Improvements may be made in this area for future work which will be discussed below.

4.2 Future Work

Through this work the reduced corrosion rate in EBSS has been well demonstrated as compared to c-SBF. Efforts should be made to improve consistent solution preparation and usage across research labs. Planning of in-vitro and in-vivo testing should be aimed at comparing reduced corrosion solutions (such

as EBSS) with results from animal studies. One possible method to accomplish both of these goals would be to attempt to reproduce in-vitro testing which was conducted as a direct comparison to in-vivo animal studies such as those conducted by Walker and Shadanbaz [51, 59]. Confirmation of the similarity of EBSS to in vivo performance for MAO coated magnesium has not been reported in literature and may be observed through a small animal study. Further development of an accurate in vitro solution would provide a more humane and quick method of evaluating future implant prototypes.

With respect to mechanical testing, further expansion on large dimension testing should be carried out to bring concept coatings closer to real world simulation. Although small scale mechanical SCC testing has been carried out on a range of coated Mg samples, exploration of large dimension MAO coated magnesium samples in constant extension testing has not been explored. Testing is required to better understand the macro-scale performance of these implant materials under stress in a corrosive environment. In order to produce large samples (1in x 5in footprint) improvements in MAO coating processing may be required. Additionally, methods of loading other than constant extension testing should be explored such as slow strain rate testing (SSRT) where sample failure is forced and observations are made on progress of corrosion cracking across a stressed cross section.

Composite materials, such as PCL on MAO are beginning to be explored in publications and may provide polymer advantages of drug delivery along with favorable base layer adhesion inherent in MAO coating. Exploration of these coatings is just beginning and may be aided in the knowledge gained through the experiments performed in our UAF lab.

Literature Cited

[1] S. Bauer, P. Schmuki, K. Von Der Mark, J. Park, Engineering biocompatible implant surfaces Part I: Materials and surfaces, Progress in Materials Science, 58 (2013) 261-326

[2] M.P. Staiger, A.M. Pietak, J. Huadmai, G. Dias, Magnesium and its alloys as orthopedic biomaterials: A review, Biomaterials, 27 (2006) 1728-1734

[3] M. Niinomi, Recent metallic materials for biomedical applications, Metallurgical and Materials Transactions A, Volume 33A (2002) 477-486

[4] Q. Chen, G.A. Thouas, Metallic implant biomaterials, Materials Science and Engineering R, 87 (2015) 1-57

[5] M. Geetha, A.K. Singh, R. Asokamani, A.K. Gogia, Ti based biomaterials, the ultimate choice for orthopaedic implants – A review, Progress in Materials Science, 54 (2009) 397-425

[6] T.W. Duerig, K.N. Melton, D. Stockel, C.M. Wayman, Engineering aspects of shape memory alloy, Butterworth-Heinemann, London, 1990

[7] B. Heublein, R. Rohde, V. Kaese, M. Niemeyer, W. Hartung, A. Haverich, Heart, 89 (2003) 651-656

[8] J.Y. Wong, J.D. Bronzino, Biomaterials, CRC Press, New York, 2007

[9] C. Lhotka, T. Szekeres, I. Steffan, K. Zhuber, K. Zweymuller, Four-year study of cobalt and chromium blood levels in patients managed with two different metal-on-metal total hip replacements, Journal of Orthopaedic Research, 21 (2003) 189-195

[10] J.J. Jacobs, A.K. Skipor, L.M. Patterson, N.J. Hallab, W.G. Paprosky, J. Black, J.O. Galante, Metal release in patients who have had a primary total hip arthroplasty. A prospective, controlled, longitudinal study, J Bone Joint Surg Am, Volume 80A (1998) 1447-1458

[11] J. Nagels, M. Stokdijk, P.M. Rozing, Stress shielding and bone resorption in shoulder arthroplasty, Journal of Shoulder and Elbow Surgery, 12 (2003) 35-39

[12] L. Tan, X. Yu, P. Wan, K. Yang, Biodegradable materials for bone repairs: A review, Journal of Materials Science and Technology, 29(6) (2013) 503-513

[13] F. Witte, N. Hort, C. Vogt, S. Cohen, K.U. Kainer, R. Willumeit, F. Feyerabend, Degradable biomaterials based on magnesium corrosion, Current Opinion in Solid State and Materials Science, 12 (2008) 63-72

[14] Z. Li, M. Kawashita, Current progress in inorganic artificial biomaterials, The Japanese Journal of Artificial Organs, 39 (2010) 190-193

[15] N.E.L. Saris, E. Mervaala, H. Karppanen, J.A. Khawaja, A. Lewenstam, Magnesium an update on physiological, clinical and analytical aspects, Clinica Chimica Acta, 294 (2000) 1-26

[16] T.S.N. Narayanan, I.S. Park, M.H. Lee, Strategies to improve the corrosion resistance of microarc oxidation (MAO) coated magnesium alloys for degradable implants: prospects and challenges, Progress in Materials Science, 60 (2014) 1-71

[17] T. Okuma, Magnesium and bone strength, Nutrition, 17 (2001) 679-680

[18] G. Song, A. Atrens, Understanding magnesium corrosion a framework for improved alloy performance, Advanced Engineering Materials, 5 (2003) 837-858

[19] L. Zhao, C. Cui, Q. Wang, S. Bu, Growth characteristics and corrosion resistance of micro-arc oxidation coating on pure magnesium for biomedical applications, Corrosion Science, 52 (2010) 2228-2234

[20] W.D. Mueller, M.L. Nascimento, M.F.L. de Mele, Critical discussion of the results from different corrosion studies of Mg and Mg alloys for biomaterials applications, Acta Biomaterialia, 6 (2010) 1749-1755

[21] Y. Song, D. Shan, R. Chen, F. Zhang, E.H. Han, Biodegradable behaviors of AZ31 magnesium alloy in simulated body fluid, Materials Science and Engineering C, 29 (2009) 1039-1045

[22] Y. Gu, C.F. Chen, S. Bandopadhyay, C. Ning, Y. Zhang, Y. Guo, Corrosion mechanism model of pulsed DC microarc oxidation treated AZ31 alloy in simulated body fluid, Applied Surface Science, 258 (2012) 6116-6126

[23] Y. Xin, T. Hu, P.K. Chu, In vitro studies of biomedical magnesium alloys in a simulated physiological environment: a review, Acta Biomaterialia, 7 (2011) 1452-1459

[24] Z. Wen, C. Wu, C. Dai, F. Yang, Corrosion behaviors of Mg and its alloys with different Al contents in a modified simulated body fluid, Journal of Alloys and Compounds, 488 (2009) 392-399

[25] B.P. Zhang, Y. Wang, L. Geng, Research on Mg-Zn-Ca alloy as degradable biomaterial, Biomaterials Physics and Chemistry, 2011

[26] H. Hornberger, S. Virtanen, A.R. Boccaccini, Biomedical coatings on magnesium alloys – A review, Acta Biomaterialia, 8 (2012) 2442-2455

[27] J. Cai, F. Cao, L. Chang, J. Zheng, J. Zhang, C. Cao, The preparation and corrosion behaviors of MAO coating on AZ91D with rare earth conversion precursor film, Applied Surface Science, 257 (2011)

[28] L. Yang, J. Li, C. Lin, M. Zhang, J. Wu, Study of molybdenum/lanthanum-based composite conversion coatings on AZ31 magnesium alloy, Applied Surface Science, 257 (2011)

[29] Y. Mizutani, S.J. Kim, R. Ichino, M. Okido, Anodizing of Mg alloys in alkaline solutions, Surface and Coatings Technology, 169-170 (2003) 143-146

[30] B.D. Hahn, D.S. Park, J.J. Choi, J. Ryu, W.H. Yoon, J.H. Choi, H.E. Kim, S.G. Kim, Aerosol deposition of hydroxyapatite-chitosan composite coatings on biodegradable magnesium alloy, Surface and Coatings Technology, 205 (2011) 3112-3118

[31] J. Hu, C. Zhang, B. Cui, K. Bai, S. Guan, L. Wang, S. Zhu, In vitro degradation of AZ31 magnesium alloy coated with nano TiO2 film by sol-gel method, Applied Surface Science, 257 (2011) 8772-8777

[32] C. Wen, S. Guan, L. Peng, C. Ren, X. Wang, Z. Hu, Characterization and degradation behavior of AZ31 alloy surface modified by bone-like hydroxyapatite for implant applications, Applied Surface Science, 255 (2009) 6433-6438

[33] A. Abdal-Hay, N.A.M. Barakat, J.K. Lim, Hydroxyapatite-doped poly(lactic acid) porous film coating for enhanced bioactivity and corrosion behavior of AZ31 Mg alloy for orthopedic applications, Ceramics International, 39 (2013) 183-195

[34] A.L. Yerokhin, X. Nie, A. Leyland, A. Matthews, S.J. Dowey, Plasma electrolysis for surface engineering, Surface and Coatings Technology, 122 (1999) 73-93

[35] F. Chen, H. Zhou, B. Yao, Z. Qin, Q. Zhang, Corrosion resistance property of the ceramic coating obtained through microarc oxidation on the AZ31 magnesium alloy surfaces, Surface & Coatings Technology, 201 (2007) 4905-4908

[36] Y. Gu, S. Bandopadhyay, C.F. Chen, Y. Guo, C. Ning, Effect of oxidation time on the corrosion behavior of micro-arc oxidation produced AZ31 magnesium alloys in simulated body fluid, Journal of Alloys and Compounds, 543 (2012) 109-117

[37] Y. Gu, C.F. Chen, S. Bandopadhyay, C. Ning, Y. Guo, Residual stress in pulsed DC microarc oxidation treated AZ31 alloy, Surface Engineering, Volume 28 (2012) 498-502

[38] J. Zhang, Y. Gu, Y. Guo, C. Ning, Electrochemical behavior of biocompatible AZ31 magnesium alloy in simulated body fluid, Journal Material Science, 47 (2012) 5197-5204

[39] N. Ostrowski, B. Lee, N. Enick, B. Carlson, S. Kunjukunju, A. Roy, P.N. Kumta, Corrosion protection and improved cytocompatibility of biodegradable polymeric layer-by-layer coatings on AZ31 magnesium alloys, Acta Biomaterialia, 9 (2013) 8704-8713

[40] N. Ostrowski, B. Lee, A. Roy, M. Ramanathan, P.N. Kumta, Biodegradable poly(lactide-co-glycolide) coatings on magnesium alloys for orthopedic applications, Journal of Material Science, 24 (2013) 85-96

[41] G.K. Soujanya, T. Hanas, V.Y. Chakrapani, B.R. Sunil, T.S.S. Kumar, Electrospun nanofibrous polymer coated magnesium alloy for biodegradable implant applications, Procedia Materials Science, 5 (2014) 817-823

[42] N. Scharnagl, C. Blawert, W. Dietzel, Corrosion protection of magnesium alloy AZ31 by coating with poly(ether imides) (PEI), Surface and Coatings Technology, 203 (2009) 1423-1428

[43] A. Zomorodian, M.P. Garcia, T.M. Silva, J.C.S. Fernandez, M.H. Fernandes, M.F. Montemor, Corrosion resistance of a composite polymeric coating applied on biodegradable AZ31 magnesium alloy, Acta Biomaterialia, 9 (2013) 8660-8670

[44] M.A. Woodruff, D.W. Hutmacher, The return of a forgotten polymer – Polycaprolactone in the 21st century, Progress in Polymer Science, 35 (2010) 1217-1256

[45] Y. Chen, Y. Song, S. Zhang, J. Li, C. Zhao, X. Zhang, Interaction between a high purity magnesium surface and PCL and PLA coatings during dynamic degradation, Biomedical Materials, 6 (2011) 025005

[46] H.M. Wong, K.W.K. Yeung, K.O. Lam, V. Tam, P.K. Chu, K.D.K. Luk, K.M.C. Cheung, A biodegradable polymer-based coating to control the performance of magnesium alloy orthopaedic implants, Biomaterials, 31 (2010) 2084-2096

[47] J.L. Gamble, Chemical Anatomy, Physiology and Pathology of Extracellular Fluid, Harvard University Press, Cambridge MA, 1967

[48] T. Kokubo, H. Takadama, How useful is SBF in predicting in vivo bone bioactivity?, Biomaterials, 27 (2006) 2907-2915

[49] A. Oyane, H.M. Kim, T. Furuya, T. Kokubo, T. Miyazaki, T. Nakamura, Preparation and assessment of revised simulated body fluids, Journal of Biomedical Materials Research Part A, Volume 65A (2003) 188-195

[50] N.I.Z. Abidin, B. Rolfe, H. Owen, J. Malisano, D. Martin, J. Hofstetter, P.J. Uggowitzer, A. Atrens, The in vivo and in vitro corrosion of high-purity magnesium and magnesium alloys WZ21 and AZ91, Corrosion Science, 75 (2013) 354-366

[51] J. Walker, S. Shadanbaz, N.T. Kirkland, E. Stace, T. Woodfield, M.P. Staiger, G.J. Dias, Magnesium alloys: predicting in vivo corrosion with in vitro immersion testing, J Biomed Mater Res Part B, 100B (2012) 1134-1141

[52] X. Wang, X. Zeng, G. Wu, S. Yao, Y. Lai, Effects of tantalum ion implantation on the corrosion behavior of AZ31 magnesium alloys, Journal of Alloys and Compounds, 437 (2007) 87-92

[53] W.D. Mueller, M.L. Nascimento, M. Zeddies, M. Corsico, L.M. Gassa, M.A.F.L. de Mele, Magnesium and its alloys as degradable biomaterials. Corrosion studies using potentiodynamic and EIS electrochemical techniques, Materials Research, Volume 10 (2007) 5-10

[54] W.E. Mueller, M.F.L. de Mele, M.L. Nascimento, M. Zeddies, Degradation of magnesium and its alloys: dependence on the composition of the synthetic biological media, Journal of Biomedical Materials Research, Volume 90A (2009) 487-495

[55] X.N. Gu, Y.F. Zheng, L.J. Chen, Influence of artificial biological fluid composition on the biocorrosion of potential orthopedic Mg-Ca, AZ31, AZ91 alloys, Biomedical Materials, 4 (2009) 065011

[56] L. Yang, E. Zhang, Biocorrosion behavior of magnesium alloy in different simulated fluids for biomedical application, Materials Science and Engineering C, 29 (2009) 1691-1696

[57] F. Witte, J. Fischer, J. Nellesen, H.A. Crostack, V. Kaese, A. Pisch, F. Beckmann, H. Windhagen, In vitro and in vivo corrosion measurements of magnesium alloys, Biomaterials, 27 (2006) 1013-1018

[58] Y. Ren, J. Huang, B. Zhang, K. Yang, Preliminary study of biodegradation of AZ31B magnesium alloy, Front. Mater. Sci. China, 1(4) (2007) 401-404

[59] S. Shadanbaz, J. Walker, T.B.F. Woodfield, M.P. Staiger, G.J. Dias, Monetite and brushite coated magnesium: in vivo and in vitro models for degradation analysis, Journal Material Science, 25 (2014) 173-183

[60] T. Kokubo, H. Kushitani, S. Sakka, T. Kitsugi, T. Yamamuro, Solutions able to reproduce in vivo surface-structure changes in bioactive glass-ceramic A-W, Journal of Biomedical Materials Research, Volume 24 (1990) 721-734

[61] H.M. Kim, K. Kishimoto, F. Miyaji, T. Kokubo, Composition and structure of apatite formed on organic polymer in simulated body fluid with a high content of carbonate ion, Journal of Materials Science Materials in Medicine, 11 (2000) 421-426

[62] H. Takadama, M. Hashimoto, M. Mizuno, T. Kokubo, Round-robin test of SBF for in vitro measurement of apatite forming ability of synthetic materials, Phosphorous Research Bulletin, Volume 17 (2004) 119-125

[63] J.C. Bryant, Earle's balanced salt solution preparation of the saline, Tissue Culture Association, Volume 1 (4) (1975) 185-187

[64] W.R. Earle, Production of malignancy in vitro, Journal National Cancer Inst., Volume 4 (2) (1943) 131-212

[65] A. Yamamoto, S. Hiromoto, Effect of inorganic salts, amino acids and proteins on the degradation of pure magnesium in vitro, Materials Science and Engineering C, 29 (2009) 1559-1568

[66] L. Xu, E. Zhang, D. Yin, S. Zeng, K. Yang, In vitro corrosion behavior of Mg alloys in a phosphate buffered solution for bone implant application, Journal Material Science Materials in Medicine, 19 (2008) 1017-1025

[67] G. Song, Control of biodegradation of biocompatible magnesium alloys, Corrosion Science, 29 (2007) 1696-1701

[68] W.C. Kim, J.G. Kim, J.Y. Lee, H.K. Seok, Influence of Ca on the corrosion properties of magnesium for biomaterials, Materials Letters, 62 (2008) 4146-4148

[69] N.T. Kirkland, N. Birbilis, M.P. Staiger, Assessing the corrosion of biodegradable magnesium implants: a critical review of current methodologies and their limitations, Acta Biomaterialia, 8 (2012) 925-936

[70] ASM Handbook, Corrosion: Fundamentals, Testing, and Protection, Volume 13A, ASM International, Materials Park, OH 2003

[71] E. Barsoukov, J.R. Macdonald, Impedance spectroscopy: theory experiment, and applications, 2nd Edition, History 1 (2005)

[72] D. Loveday, P. Peterson, B. Rodgers, Evaluation of organic coatings with electrochemical impedance spectroscopy, Part 1: Fundamentals of electrochemical impedance spectroscopy, JCT Coatings Tech, 2004

[73] A. Ghasemi, V.S. Raja, C. Blawert, W. Dietzel, K.U. Kainer, Study of the structure and corrosion behavior of PEO coatings on AM50 magnesium alloy by electrochemical impedance spectroscopy, Surface and Coatings Technology, 202 (2008) 3513-3518

[74] D. Loveday, P. Peterson, B. Rodgers, Evaluation of organic coatings with electrochemical impedance spectroscopy, Part 2: Application of EIS to coatings, JCT Tech, 2004

[75] J. Liang, P.B. Srinivasan, C. Blawert, M. Stormer, W. Dietzel, Electrochemical corrosion behaviour of plasma electrolytic oxidation coatings on AM50 magnesium alloy formed in silicate and phosphate based electrolytes

[76] F. Mansfeld, H. Shih, H. Greene, C.H. Tsai, Analysis of EIS data for common corrosion processes, ASTM Special Technical Publication, 1188 (1993)

[77] T.F. Conceicao, N. Scharnagl, C. Blawert, W. Dietzel, K.U. Kainer, Corrosion protection of magnesium alloy AZ31 sheets by spin coating process with poly(ether imide) PEI, Corrosion Science, 52 (2010) 2066-2079

[78] ASTM G59-97 Standard test method for conducting potentiodynamic polarization resistance measurements (2014)

[79] J.J. Jacobs, J.L. Gilbert, R.M. Urban, Current concepts review – corrosion of metal orthopaedic implants, J Bone and Joint Surgery, 80-A(2) (1998) 268-282

[80] K.W. Guo, A review of magnesium/magnesium alloys corrosion and its protection, Recent Patents on Corrosion Science, 2 (2010) 13-21

[81] Y. Uematsu, T. Kakiuchi, M. Nakajima, Stress corrosion cracking behavior of the wrought magnesium alloy AZ31 under controlled cathodic potentials, Materials Science and Engineering A, 531 (2012) 171-177

[82] H.X. Wang, S.K. Guan, X. Wang, C.X. Ren, L.G. Wang, In vitro degradation and mechanical integrity of Mg-Zn-Ca alloy coated with Ca-deficient hydroxyapatite by the pulse electrodeposition process, Acta Biomaterialia, 6 (2010) 1743-1748

[83] M.B. Kannan, V.S. Raja, Enhancing stress corrosion cracking resistance in Al-Zn-Mg-Cu-Zr alloy through inhibiting recrystallization, Engineering Fracture Mechanics, 77 (2010) 249-256

[84] M.B. Kannan, R.K.S. Raman, In vitro degradation and mechanical integrity of calcium-containing magnesium alloys in modified-simulated body fluid, Biomaterials, 29 (2008) 2306-2314

[85] L. Choudhary, J. Szmerling, R. Goldwasser, R.K.S. Raman, Investigations into stress corrosion cracking behaviour of AZ91D magnesium alloy in physiological environment, Procedia Engineering, 10 (2011) 518-523

[86] N. Winzer, A. Atrens, W. Dietzel, V.S. Raja, G. Song, K.U. Kainer, Characterisation of stress corrosion cracking (SCC) of Mg-Al alloys, Materials Science and Engineering A, 488 (2008) 339-351

[87] G.R. Argade, W. Yuan, K. Kandasamy, R.S. Mishra, Stress corrosion cracking susceptibility of ultrafine grained AZ31, Journal of Materials Science, 47 (2012) 6812-6822

[88] R.G. Song, C. Blawert, W. Dietzel, A. Atrens, A study on stress corrosion cracking and hydrogen embrittlement of AZ31 magnesium alloy, Materials Science and Engineering A, 399 (2005) 308-317

[89] Y. Zhang, J. You, J. Lu, C. Cui, Y. Jiang, X. Ren, Effects of laser shock processing on stress corrosion cracking susceptibility of AZ31B magnesium alloy, Surface and Coatings Technology, 204 (2010) 3947-3953

[90] ASTM G39-99 Standard practice for preparation and use of bent-beam stress-corrosion test specimens (2011)

[91] M. Gupta, N.M.L. Sharon, Magnesium, magnesium alloys, and magnesium composites, John Wiley and Sons, 2011